Optoelectronic THz ratchets in two-dimensional metamaterials

Dissertation

zur Erlangung des Doktorgrades
der Naturwissenschaften (Dr. rer. nat.)
der Fakultät für Physik
der Universität Regensburg

vorgelegt von

Marcel Hild

aus Sinzing

im Jahr 2025

Promotionsgesuch eingereicht am: 09.01.2025

Die Arbeit wurde angeleitet von: Prof. Dr. Sergey D. Ganichev

Prüfungsausschuss

Vorsitzender: Prof. Dr. Klaus Richter
1. Gutachter: Prof. Dr. Sergey D. Ganichev
2. Gutachter: Prof. Dr. Jörg Wunderlich
weiterer Prüfer: PD Dr. Jonathan Eroms

Contents

1 Introduction 5

2 Fundamentals 9

2.1 Dirac fermions . . . 9
  2.1.1 The Dirac equation . . . 9
  2.1.2 Graphene . . . 10
2.2 Ferromagnetic characteristics in 2D systems . . . 14
  2.2.1 Micromagnetism . . . 14
  2.2.2 Anomalous Hall effect . . . 17
2.3 Ratchets in one-dimensional metamaterials . . . 18
  2.3.1 Phenomenology . . . 19
  2.3.2 Kinetic theory . . . 21
2.4 Cyclotron resonance . . . 24
  2.4.1 Quasi-classical treatment . . . 24
  2.4.2 Quantum mechanical treatment . . . 25

3 Methods and samples 29

3.1 THz laser source . . . 29
  3.1.1 CO_2 laser . . . 29
  3.1.2 Molecular gas laser . . . 31
3.2 Experimental setup . . . 32
  3.2.1 Laser beam characteristics and measurement technique . . . 32
  3.2.2 Altering the polarisation state of the radiation . . . 34
3.3 Investigated samples . . . 36
  3.3.1 Graphene-based metamaterial . . . 36
  3.3.2 Ferromagnetic metamaterial . . . 40

4 Linear ratchets in patterned-gated graphene **43**

4.1 Experimental results on linear ratchets 43

4.2 Discussion 49

5 Circular ratchets in patterned-gated graphene **55**

5.1 Experimental results on circular ratchets 55

5.2 Discussion 58

6 Magneto-ratchets in patterned-gated graphene **63**

6.1 Experimental results on magneto-ratchets 63

6.2 Discussion 67

7 Ratchets in the magnetic metamaterial **75**

7.1 Experimental results on the magnetic metamaterial 75

7.2 Discussion 80

8 Conclusion **89**

References **102**

Acknowledgments **103**

1 Introduction

The optoelectronic ratchet effect has emerged as a rapidly expanding area of interest in both fundamental and applied terahertz (THz) physics. This effect occurs in out-of-equilibrium systems without spatial inversion center and provides the conversion of the ac high-frequency electric field of the radiation into an dc electric current, despite the macroscopic average force is zero [2,19,97].

For the realisation of optoelectronic ratchets, it has been suggested to use artificially and periodically structured system – so called metamaterials with a superimposed structure much smaller than the radiation wavelength. The exceptional tunable geometry of this material predestines it for a wide range of potential applications and have attracted increasing attention due to their excellent ability to provide ratchet currents excited by THz radiation in systems, including the one-dimensional (1D) lateral modulation in comb-like dual-grating-gate (DGG) in bilayer [14,17,23,95] or monolayer [4,8,96] graphene, and quantum well-based field effect transistor structures [1,3,5–7,9,13,15,18]. The emergence of electric ratchet currents in DGGs has been attributed to the combined action of the periodic electrostatic potential and the asymmetric near-field amplitude created by diffraction on the grating. Studies on DGGs have also demonstrated that ratchet currents may have multiple origins, such as the electronic ratchet effect [1,8,11,14,18–23], the plasmonic ratchet/drag effect [3,5,7,8,13,14,16,23–41], or the photo-thermoelectric effect [16,42–46]. Here, intensive investigations have been done over a wide range of frequencies from gigahertz (GHz) to tens of THz [8,10,12–14,23,41,47–49].

Strikingly, the ratchet effect has also demonstrated the ability to produce spin-polarised currents or even pure spin currents [54,55]. These spin ratchets paved the way for efficient generation and tunability of spin fluxes [56]. Recently, the THz magneto-ratchet effect resulting in a spin-polarised electric current has been observed in DGGs, in lateral superlattices fabricated on diluted magnetic semiconductor (DMS), and in gallium nitride two-dimensional (2D) electron systems [39,57,58]. It has been shown that the spin magneto-ratchet is caused by the joint action of spin-orbit interaction and the Zeeman effect and is supposed to be significantly enhanced in DMS materials with a lateral superlattice made of ferromagnetic materials. Most recently, spin-ratchets in a stack of cobalt (Co) and platinum (Pt) have been reported by exciting the ferromagnetic metamaterial by visible or near-infrared light [59].

In this thesis, the concept of yielding THz-induced ratchet currents in a 1D-modulated 2D electron systems is extended to 2D modulation, which has not been studied so far. Also, in contrast to previous works on DGGs, the structures in this work do not have asymmetric periodic stripes on top. Instead, 2D modulation is achieved by introducing periodically arranged triangular holes either in the bottom gate or into the material itself.

Specifically, two types of samples have been investigated. The first type is a monolayer of graphene encapsulated in hexagonal boron nitride [121–123]. These samples have a conventional homogeneous back gate. However, in addition they have a patterned back gate, comprising triangular holes arranged in a squared antidot array. As the patterned gate is situated closer to the graphene sheet, it screens the homogeneous gate. This enables one to selectively tune the modulation of both the electrostatic potential and the Fermi energy (i.e. the carrier density), as demonstrated by electrical transport measurements in Ref. [60] in a similar sample. In this thesis it is demonstrated for the first time that the direction and magnitude of the ratchet current in the graphene-based 2D metamaterials can be controlled upon variation of the linear and circular polarisation state of the incident THz radiation electric field, and upon the applied gate voltages [121,122]. Moreover, it is demonstrated that if the graphene metamaterial is subjected to an out-of-plane magnetic field B, sign-alternating magneto-ratchets are observed that exhibit $1/B$-periodic oscillations with an amplitude orders of magnitude larger than the ratchet current at zero magnetic field [123]. Furthermore, resonant absorption of radiation by the carriers, referred to as cyclotron resonance (CR) has been observed. The $1/B$-periodic magneto-ratchets as well as the ratchet currents due to CR have been studied for several combinations of the applied back and patterned gate voltage. Analysing these data demonstrates that in contrast to resistance measurements, the ratchet currents enables one to identify the spatial origin of the observed ratchet effects and the role of the Shubnikov–de Haas oscillations for the formation of the magneto-ratchet effect.

The second system is based on a stacking of ferromagnetic Co and paramagnetic Pt which has triangular holes in the material itself arranged in a hexagonal lattice [125], as previously investigated in Ref. [59] in the visible and near-infrared spectral range. This special layer sequence provides a strong perpendicular magnetic anisotropy [61,62] and a distinct magnetic hysteresis. It is demonstrated that exciting this device with THz radiation results in the formation of spin-ratchets that can be either polarisation-sensitive or -insensitive, which has not been investigated before [125]. The analysis of the experimental data demonstrates that the spin-ratchets are closely related to the anomalous Hall effect or the anomalous Nernst effect.

This thesis is structured in the following way: Chapter 2 addresses fundamental principles and concepts. First, relativistic Dirac fermions are introduced in Sec. 2.1 and their close analogue to graphene, which hosts massless Dirac fermions, is demonstrated. Afterwards, Sec. 2.2 depicts key concepts of magnetic domains, the emergence of the magnetic hysteresis, and the AHE, which are relevant for the understanding of the ratchet phenomena in the ferromagnetic sample. In Sec. 2.3 is presented the basic principle of the ratchet effect on the example of a DGG. Thereby, the phenomenological as well as microscopic descriptions are presented. Then, the phenomenon of resonant radiation absorption by charge carriers in the presence of magnetic field, the cyclotron resonance, is outlined in Sec. 2.4. Chapter 3 covers the experimental techniques and samples. It starts with the description of the THz source (Sec. 3.1), followed by the experimental setup (Sec. 3.2) and the description of the characteristic of the used graphene- and Co/Pt-based metamaterials (Sec. 3.3). The experimental results are presented and discussed in Chaps. 4–7 First, the results of the linear ratchet in graphene are shown in Chap. 4 and the results of the circular ratchet in Chap. 5. Subsequently, data of the magneto-ratchets in graphene are shown in Chap. 6. The results of the ferromagnetic metamaterial are shown in Cap. 7. Finally, the thesis is summarised in Chap. 8.

2 Fundamentals

This chapter outlines the theoretical background of this thesis. It starts with the Dirac equation and its limit for massless particles, which is crucial for grasping the peculiar properties of graphene. The ansatz of a tight-binding model shows that graphene exhibits linear energy dispersion, and thus that it hosts massless Dirac fermions. This demonstrates that electrons in graphene are intimately connected to the Dirac theory. Subsequently, the fundamental properties and models of magnetic quantum films are introduced, including the manifestation of hysteresis in the magnetisation by using the Stoner–Wohlfarth model, the formation of magnetic domains, and the anomalous Hall effect. Then, ratchets are introduced for one-dimensional metamaterials in terms of both a phenomenological and a microscopic description. Afterwards, optical absorption by free carriers is depicted, in particular in the presence of a magnetic field giving rise to resonant absorption due to cyclotron resonance. This phenomenon is treated within the quasi-classical and the quantum mechanical theory, with the latter predicting the emergence of Landau levels.

2.1 Dirac fermions

This section addresses relativistic particles. First, the Dirac equation of free fermions is introduced, showing that massless particles have linear dispersion. Afterwards, crystallographic and electrical properties of graphene are depicted, where the tight-binding model reveals that carriers in graphene can have zero effective mass; thus, they are connected to the Dirac theory. Subsequently, an overview of the optical transitions of graphene is given.

2.1.1 The Dirac equation

In 1928, one issue in quantum mechanics was that the Schrödinger equation for spin-1/2 particles did not include relativity, and that the relativistic Klein–Gordon equation is non-linear and describes spinless particles. To overcome this obstacle, Paul Dirac proposed a linearisation by introducing four 4×4 matrices and writing [63]

$$\left(c\boldsymbol{\alpha} \cdot \boldsymbol{p} + \beta mc^2\right) \psi = E\psi \,, \tag{2.1}$$

where c is the speed of light, $\boldsymbol{p}$ the momentum operator, m the mass of the particle, and $\beta, \boldsymbol{\alpha}$ the Dirac matrices

$$\beta = \begin{pmatrix} \mathbb{1}_2 & 0 \\ 0 & -\mathbb{1}_2 \end{pmatrix}, \quad \text{and} \quad \alpha_i = \begin{pmatrix} 0 & \sigma_i \\ \sigma_i & 0 \end{pmatrix}. \tag{2.2}$$

Here, $\mathbb{1}_2$ is the 2×2 unit matrix and σ_i are the Pauli matrices given by

$$\sigma_x = \begin{pmatrix} 0 & 1 \\ 1 & 0 \end{pmatrix}, \; \sigma_y = \begin{pmatrix} 0 & -i \\ i & 0 \end{pmatrix}, \; \sigma_z = \begin{pmatrix} 1 & 0 \\ 0 & -1 \end{pmatrix}. \tag{2.3}$$

The eigenvalues for relativistic free particles in Eq. (2.1) are [63]

$$E_\pm = \pm\sqrt{m^2c^4 + p^2c^2}\,, \tag{2.4}$$

where both solutions are double degenerate. The two solutions with positive energy describe electrons with spin-up and spin-down, and the two negative solutions the electron's antiparticles, the positrons, also with these two spin states. It can be seen that at $p = 0$, the two solutions exhibit an energy gap of $E_+ - E_- = 2mc^2$. In the zero-mass limit, Eq. (2.4) takes the form

$$E_\pm = \pm c|p|\,. \tag{2.5}$$

This is often described in the framework of the Weyl equation $E = c\boldsymbol{\sigma} \cdot \boldsymbol{p}$ [64]. Accordingly, the eigenfunctions of massless spin-1/2 particles are two-component Weyl spinors.

2.1.2 Graphene

Graphene is an atomically thin layer made of carbon atoms. It was fabricated for the first time in 2004 [66–68] and is known to host massless Dirac fermions. Although in graphene spin-orbit interaction vanishes, relativistic behaviour manifests because of the hexagonal lattice structure of the carbon atoms. In the following, the crystallographic properties and intrinsic electronic characteristics of this intriguing material are addressed.

Figure 2.1(a) depicts the real-space arrangement of the carbon atoms. This honeycomb lattice can be regarded as two triangular sublattices A and B with two atoms per

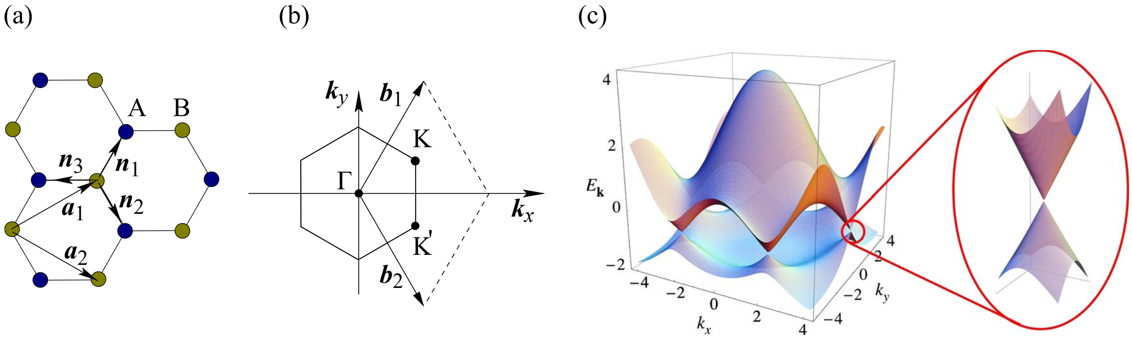

Figure 2.1 | Panel (a) shows the honeycomb real-space lattice with sublattices A and B, lattice vectors $\boldsymbol{a}_i$, and the nearest-neighbour vectors $\boldsymbol{n}_i$. Panel (b) depicts the Brillouin zone with the Γ point, the Dirac points K and K′, and the reciprocal vectors $\boldsymbol{b}_i$. Panel (c) illustrates the energy dispersion with the zoom-in showing one Dirac cone. Adapted from Ref. [65].

unit cell. The lattice vectors are given by [65,69]

$$\boldsymbol{a}_1 = \frac{a}{2}\left(3, \sqrt{3}\right), \quad \boldsymbol{a}_2 = \frac{a}{2}\left(3, -\sqrt{3}\right), \tag{2.6}$$

where $a \approx 1.42\,\text{Å}$ is the distance between two adjacent atoms. The nearest-neighbour vectors are

$$\boldsymbol{n}_1 = \frac{a}{2}\left(1, \sqrt{3}\right), \quad \boldsymbol{n}_2 = \frac{a}{2}\left(1, -\sqrt{3}\right), \quad \boldsymbol{n}_3 = -a\left(1, 0\right). \tag{2.7}$$

Figure 2.1(b) shows the Brillouin zone (BZ) of the reciprocal honeycomb lattice with vectors

$$\boldsymbol{b}_1 = \frac{2\pi}{3a}\left(1, \sqrt{3}\right), \quad \boldsymbol{b}_2 = \frac{2\pi}{3a}\left(1, -\sqrt{3}\right). \tag{2.8}$$

Of particular interest are the high-symmetry point Γ and the points at the corners of the BZ, K and K′, which are referred to as Dirac points.

Next, graphene's band structure is calculated. Each carbon atom hosts six electrons: two in the inner $1s$ shell, three in the three in-plane covalent sp^2 bond, and one in the out-of plane p_z orbital [70]. In the framework of the tight-binding model considering electron hopping to adjacent atoms, denoted by $\langle i, j\rangle$, and to second-nearest neighbours, denoted by $\langle\langle i, j\rangle\rangle$, the Hamiltonian reads [65]

$$H = -t \sum_{\langle i,j\rangle,\sigma} \left(a^\dagger_{\sigma,i} b_{\sigma,j} + \text{h.c.}\right) - t' \sum_{\langle\langle i,j\rangle\rangle,\sigma} \left(a^\dagger_{\sigma,i} a_{\sigma,j} + b^\dagger_{\sigma,i} b_{\sigma,j} + \text{h.c.}\right), \tag{2.9}$$

where $a_{i,\sigma}$ and $(a^\dagger_{i,\sigma})$ annihilates (creates) an electron having spin σ on site $\boldsymbol{r}_i$ [65].

The parameter $t \approx 2.8\,\text{eV}$ [65,71] describes inter-sublattice hopping (A→B, B→A), and the parameter $t' \approx 0.1\,\text{eV}$ [71,72] intra-sublattice hopping (A→ A, B→ B). Note that h.c. is the Hermitian conjugate. From this model the analytical solution can be expressed as [65,73]

$$E_{\pm}(\boldsymbol{k}) = \pm t\sqrt{3 + f(\boldsymbol{k})} - t' f(\boldsymbol{k})\,, \tag{2.10}$$

with

$$f(\boldsymbol{k}) = 2\cos\left(\sqrt{3}k_y a\right) + 4\cos\left(\frac{\sqrt{3}}{2}k_y a\right)\cos\left(\frac{3}{2}k_x a\right)\,, \tag{2.11}$$

where "+" and "–" refers to the upper π^* (conduction) and lower π (valence) band, respectively. It can be shown that for $t' = 0$ the spectrum in Eq. (2.11) [see Figure 2.1(c)] is symmetric in the vicinity of zero energy. If $t' \neq 0$, the electron-hole symmetry is broken and the π^*, π bands are asymmetric. The zoom-in in Fig. 2.1(c) depicts the Dirac cone dispersion, which is acquired by expansion of Eq. (2.11) close to the K (or K') point yielding [65,69,70,73]

$$E_{\pm} \approx \hbar v_0 |\boldsymbol{k}|\,, \tag{2.12}$$

where $\boldsymbol{k}$ is now expressed relatively to the Dirac point K (or K'), and v_0 is the Fermi velocity $v_0 = 3ta/2 \approx 10^6\,\text{m/s} \approx c/300$ [65,73]. At this point, it should be emphasised that in systems hosting carriers with linear dispersion, such as graphene, v_0 does neither depend on energy nor on momentum, in strong contrast to the Fermi velocity v_F in systems with parabolic dispersion [65]. In the following and also in the scope of this thesis, the band structure of graphene is considered in the vicinity of the Dirac point. At this point it is fourfold degenerate, comprising twofold spin and valley degeneracy, and has the density of states per unit cell $\rho(E) = 2A|E|/(\pi v_0^2)$ with $A = 3\sqrt{3}a^2/2$ [65].

Equations (2.5) and (2.12) have the same form if one sets $\boldsymbol{p} \to \hbar\boldsymbol{k}$ and $c \to v_0$. Due to this close analogy, carriers in graphene are often referred to as massless Dirac fermions. Indeed, the existence of the two sublattices A and B gives rise to a chiral pseudo-spin in close analogue to the electron spin. This leads to two linear bands intersecting at the Dirac points [69]. It can be shown that the effective low-energy Hamiltonian in graphene can be written as [65,69]

$$H_\text{K} = \hbar v_0 \begin{pmatrix} 0 & k_x - ik_y \\ k_x + ik_y & 0 \end{pmatrix} = \hbar v_0\, \boldsymbol{\sigma} \cdot \boldsymbol{k}\,, \tag{2.13}$$

where $\boldsymbol{\sigma} = (\sigma_x, \sigma_y)$ expresses the pseudo-spin. For the K' point, Eq. (2.13) takes the form $H_{\mathrm{K}'} = \hbar v_0\, \boldsymbol{\sigma}^* \cdot \boldsymbol{k}$. The corresponding two-dimensional pseudo-spinors for the K and K' points are

$$\psi_{\pm,\mathrm{K}}(\boldsymbol{k}) = \frac{1}{\sqrt{2}} \begin{pmatrix} e^{-i\theta_{\boldsymbol{k}}/2} \\ \pm e^{i\theta_{\boldsymbol{k}}/2} \end{pmatrix}, \quad \psi_{\pm,\mathrm{K}'}(\boldsymbol{k}) = \frac{1}{\sqrt{2}} \begin{pmatrix} e^{i\theta_{\boldsymbol{k}}/2} \\ \pm e^{-i\theta_{\boldsymbol{k}}/2} \end{pmatrix}, \tag{2.14}$$

with $\theta_{\boldsymbol{k}} = \arctan(k_x/k_y)$, and "±" corresponds to $E = \pm\hbar v_0 |k|$. The pseudo-spinors in Eq. (2.14) are eigenstates of the helicity operator $\hat{h} = \boldsymbol{\sigma} \cdot \boldsymbol{p}/(2|\boldsymbol{p}|)$, and thus electrons (holes) possess positive (negative) helicity. At large energy or finite t', helicity is not a good quantum number [65].

Graphene does not only exhibit special electronic characteristics but also intriguing optic peculiarities, such as the nearly frequency-independent interband absorption of $\pi\alpha \approx 0.023$ [75] for large frequencies, where $\alpha \approx 1/137$ is the fine structure constant. As far as optical transitions in the THz range are concerned, also indirect intraband transitions become important, as this effect typically becomes stronger with larger wavelengths [76], and since the photon energy (order of 10 meV) is small compared to typical Fermi energies (order of 100 meV); see Fig. 2.2. This Drude-like absorption describes scattering via phonons or impurities considered as virtual states.

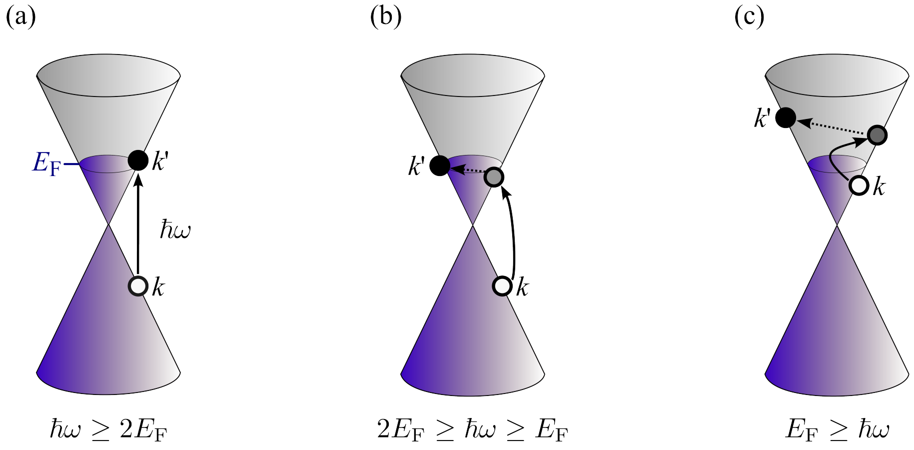

Figure 2.2 | Optical transitions in graphene for the electron regime, i.e. $E_\mathrm{F} > 0$ marked in blue. Panel (a) depicts direct interband, panel (b) indirect interband, and panel (c) indirect intraband transitions. Solid arrows indicate electron-photon interaction, and dashed arrows electron scattering by phonons or impurities. Initial, virtual, and final states are marked by white, grey and black circles, respectively. Adapted from [74].

2.2 Ferromagnetic characteristics in 2D systems

This section is dedicated to magnetism, with focus on two-dimensional metals. After a brief phenomenological description of magnetisation in the classical theory, the Landau–Lifshitz approach of micromagnetism is introduced. Subsequently, the Stoner–Wohlfarth model of magnetic hysteresis is described. Then, the formation of domains and domain walls are outlined, after which an overview of the anomalous Hall effect is given.

Regarding the magnetisation vector $\boldsymbol{M}$, the fundamental relation to the external magnetic field $\boldsymbol{H}$ in linear response is given by [83]

$$M_i = \chi_{ij} H_j \,, \tag{2.15}$$

where the magnetic susceptibility tensor is $\chi_{ij} = \partial M_i / \partial H_j$. Phenomenologically, there are three classical states of magnetism: (i) diamagnetism ($\chi < 0$), (ii) paramagnetism ($\chi > 0$), and ferromagnetism ($\chi \gg 1$). Thereby, only ferromagnetism can have non-zero magnetisation in the absence of an external H-field [83].

2.2.1 Micromagnetism

Micromagnetism is a continuum theory pioneered by Landau and Lifshitz [77]. In this theory, the ensemble of quantised magnetic moments is replaced by the continuous magnetisation vector field $\boldsymbol{M}$. In the continuum limit, this quantity is expressed by an integral [77,78]. For static micromagnetism, the spatial magnetisation distribution can be acquired by minimising the total magnetic energy [62,78,79]

$$E_{\text{mag}} = E_{\text{ex}} + E_{\text{an}} + E_{\text{Z}} + E_{\text{d}} \,. \tag{2.16}$$

Here, E_{ex} denotes the exchange, E_{an} the anisotropy, E_{Z} the Zeeman, and E_{d} the demagnetisation energy.

The exchange energy results from the long-range dipole-dipole interaction of the magnetic momenta governed by the Pauli principle and the Coulomb repulsion. In the Heisenberg theory, the Hamiltonian reads

$$H = -J \sum_{i \neq j} \boldsymbol{S}_i \cdot \boldsymbol{S}_j \,, \tag{2.17}$$

in which the exchange integral J leads to ferromagnetism if $J > 0$ and to antiferromagnetism if $J < 0$. The exchange energy is isotropic and tends to align adjacent spins parallel.

However, the anisotropy energy imposes preferred directions for the magnetisation. This leads to directions in which the magnetisation can be aligned easier compared to other directions, referred to as easy and hard axis. The anisotropy energy is composed of several contributions, such as the boundary, surface, or the volume anisotropy. The latter causes an alignment along a favourable crystal axis. In case of uni-axial anisotropy with only one easy axis, the energy density of the volume anisotropy can be written in lowest order as

$$E_{\mathrm{an,v}}/V = K_{\mathrm{v1}} \sin^2(\alpha)\,, \tag{2.18}$$

with the angle α between the easy axis and the magnetisation; see Fig. 2.3(a). For cobalt, the ferromagnetic material used in this thesis, the coefficients are $K_{\mathrm{v1}} = 410\,\mathrm{kJ/m^3}$ and $K_{\mathrm{v2}} = 100\,\mathrm{kJ/m^3}$ [80]. The energy density due to boundary and surface anisotropy arises on surfaces or interfaces of thin films because the translation symmetry is broken, giving rise to an easy axis perpendicular to the plane. For thin films it is given by

$$E_{\mathrm{an,bs}}/V = \frac{2K_{\mathrm{bs}}}{d} \sin^2(\alpha)\,. \tag{2.19}$$

In micromagnetism the Zeeman energy is expressed as

$$E_{\mathrm{Z}} = -\mu_0 \int \boldsymbol{M} \cdot \boldsymbol{H} \,\mathrm{d}V\ , \tag{2.20}$$

and consequently the energy density is

$$E_{\mathrm{Z}}/V = -\mu_0 \boldsymbol{M} \cdot \boldsymbol{H} = -\mu_0 M_{\mathrm{s}} H \cos\phi\,. \tag{2.21}$$

Here, M_{s} is the saturation magnetisation and ϕ the angle between magnetisation and external $\boldsymbol{H}$-field; see Fig. 2.3(a).

Finally, the stray field energy reads

$$E_{\mathrm{str}} = -\frac{\mu_0}{2} \int \boldsymbol{M} \cdot \boldsymbol{H}_{\mathrm{str}} \,\mathrm{d}V\ . \tag{2.22}$$

Because the stray field $H_{\mathrm{str},i} = D_{ij} M_j$ is coupled to magnetisation by a demagnetisation tensor, for thin magnetic films the energy density is [80,81]

$$E_{\mathrm{str,film}}/V = \frac{\mu_0}{2} M_{\mathrm{s}}^2 \cos^2(\alpha)\,, \tag{2.23}$$

and originates from the Maxwell equation $\nabla \cdot \boldsymbol{B} = \mu_0 \nabla \cdot (\boldsymbol{M} + \boldsymbol{H}) = 0$ [79].

Stoner–Wohlfarth model. Minimising the total magnetic energy in Eq. (2.16) is a hard task, and in general it is possible only with numerical methods. To overcome this difficulty, the Stoner–Wohlfarth model was developed [82], which takes into account merely an uni-axial anisotropy potential affected by the Zeeman term, and assumes the magnetic moments to rotate coherently, described by the average magnetisation $\boldsymbol{M}$. Moreover, only one magnetic domain is considered. The working equation in this model is [82,83]

$$E_{\mathrm{SW}}/V = K\sin^2(\theta-\phi) - \mu_0 H M_{\mathrm{s}}\cos\phi\,, \tag{2.24}$$

where θ is the angle between $\boldsymbol{H}$ and the easy axis, and ϕ the angle between $\boldsymbol{M}$ and $\boldsymbol{H}$. The two special cases are $\theta = 0$ ($\boldsymbol{H}$ parallel to the easy axis) and $\theta = 90°$ ($\boldsymbol{H}$ parallel to the hard axis), as only for these angles there are known analytical solutions. Generally speaking, the magnetisation tends to be parallel to the easy axis for low magnetic fields and aligns to $\boldsymbol{H}$ for large magnetic fields. In this thesis, $\theta = 0$ is the most important case, as the external field is applied along the easy axis. Figure 2.3(b) presents the solution $M(H)$ of Eq. (2.24) for several values of θ. It can be seen that the model predicts hysteresis for $\theta \neq 90°$. Furthermore, it can be seen that for $\theta = 0$ the critical field $H_{\mathrm{k}} = 2K/(\mu_0 M_{\mathrm{s}})$ equals the coercive field H_{c}, which is the reversed-applied field at which the magnetisation is reduced to zero.

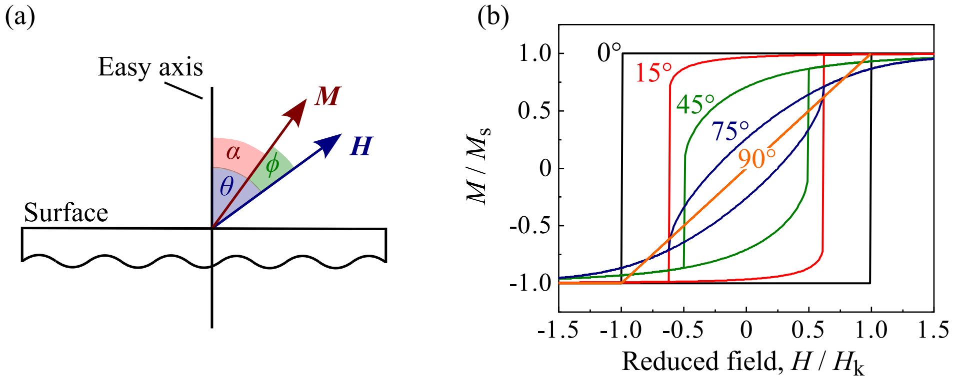

Figure 2.3 | Panel (a) depicts the definitions used in this section for the angles between the easy axis, the magnetisation $\boldsymbol{M}$, and the external magnetic field $\boldsymbol{H}$. It is shown for the specific case of an out-of-plane easy axis. Panel (b) shows the calculated curves of the magnetisation for different values of θ according to Eq. (2.24) normalised to the saturation magnetisation versus the reduced field H/H_{k}, with $H_{\mathrm{k}} = 2K/(\mu_0 M_{\mathrm{s}})$. Adapted from Ref. [62].

Domain formation. The Stoner–Wohlfarth model predicts one fingerprint of ferromagnetism – the hysteresis – but does not include the formation of domains. Actually, real ferromagnet systems are in a multi-domain state prior to exposure to an external H-field, because defects and inhomogeneities lower the total energy; see Eq. (2.16). However, the formation of multiple domains increases the total energy because of the energy stored in domain walls. As $\nabla \cdot \boldsymbol{H} = -\nabla \cdot \boldsymbol{M}$, a demagnetising field originates; see Eq. (2.23). This energy can be reduced by building domains [83]. Hence, the formation of domains in the sample is an interplay between the demagnetisation energy and the domain wall energy. The thickness of a domain wall is the distance after which M has rotated from the orientation of one domain to the orientation of the adjacent domain, and is governed by the interplay between the exchange and anisotropy energy [83].

Real ferromagnets do exhibit different domains with each one having one single magnetisation orientation. However, neighbouring domains can have a different orientation. The most prominent domain wall type is the Bloch wall in which $\boldsymbol{M}$ rotates smoothly by 180° between adjacent domains. Thereby, the rotation occurs in the plane of the two domain walls [83]. The ensemble of magnetic domains, which are often referred to as Weiss districts, can be aligned by applying a magnetic field that is large enough such that the magnetisation saturates, $M \to M_\mathrm{s}$. In this work, the studied magnetic sample consists of a symmetric stack of repeating Co and Pt. This type of sample is known to possess strong anisotropy with the easy axis pointing out-of-plane [61,62], and to have a controllable coercive field strength by tuning the layer thicknesses of the ferromagnetic Co and the paramagnetic Pt compound [84,85].

2.2.2 Anomalous Hall effect

The Hall resistivity of a 2D magnetic system can be written as

$$\rho_\mathrm{H} = R_0 B + R_\mathrm{S} M \,, \tag{2.25}$$

where the first term is the normal, classical Hall effect which is proportional to the magnetic field and emerges because of the classical Lorentz force [86]. At large magnetic fields and sufficiently low temperatures, this term becomes inappropriate and the effect translates into the quantum Hall effect [87], which is related to the condensation of the density of states due to the formation of Landau levels; see the quantum mechanical treatment of Sec. 2.4. The second term is non-zero in ferromagnetic samples and is referred to as the anomalous Hall effect (AHE). This effect describes the deflection of charge carriers depending on the orientation of $\boldsymbol{M}$.

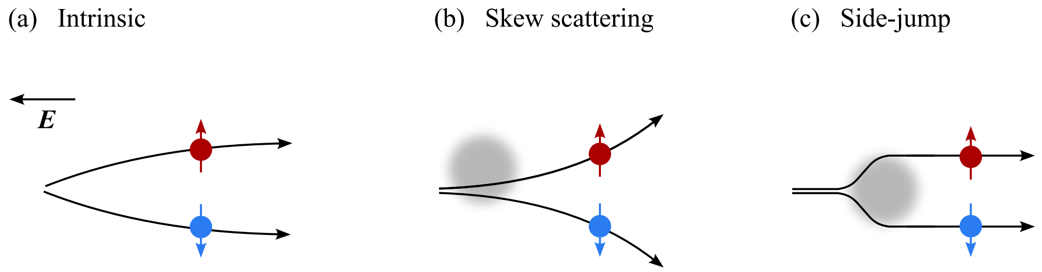

Figure 2.4 | Contributions to the anomalous Hall effect. Panel (a) shows the intrinsic deflection due to the Berry curvature, panel (b) depicts skew scattering emerging from asymmetric scattering due to spin-orbit coupling between the conduction electron and the impurity, and panel (c) shows side-jump scattering which originates because the electrons experience spin-dependent electric fields during propagating towards and offwards impurities. After Ref. [88].

The AHE is commonly assumed to be formed by the combination of one intrinsic and two extrinsic mechanisms [89–91]. On one hand, the intrinsic contribution results from spin-orbit interaction of spin-polarised conduction electrons with intrinsic scattering centers. Applying an electric field $\boldsymbol{E}$, the group velocity $\boldsymbol{v}_\mathrm{g} = \hbar^{-1}\nabla_{\boldsymbol{k}} E(\boldsymbol{k}) + e\hbar^{-1}\boldsymbol{E}\times\boldsymbol{\Omega}$ acquires an anomalous correction due to the Berry curvature $\boldsymbol{\Omega}$ [92,93], which in turn depends on the electrons' Bloch function properties in the BZ. This effect has a large contribution in ferromagnets of moderate conductivity [90,94]. On the other hand, the extrinsic skew-scattering arises because the spin-orbit coupling between the conduction electrons and the localised scattering centers translates into asymmetric scattering rates [88]. Skew-scattering dominates for high conductivity [90,94]. The side-jump scattering arises because the electrons experience spin-dependent electric fields during propagating towards and offwards the impurity [88]. Semi-classically, side-jump scattering corresponds to spin-orbit coupling scattering of a Gaussian wave packet with momentum $\boldsymbol{k}$ off a spherical impurity, which displaces the transverse component of $\boldsymbol{k}$ [89,94]. Side-jump scattering has a high contribution if the ferromagnet has moderate conductivity [90,94].

2.3 Ratchets in one-dimensional metamaterials

Systems that are driven out of thermal equilibrium allow for charge carrier transport even if the macroscopic force averages to zero – this phenomenon is referred to as the ratchet effect. The optoelectronic ratchet effect requires a simultaneous lack of thermal equilibrium due to electromagnetic waves and of spatial inversion symmetry due to an extrinsically imposed asymmetric electrostatic potential. Accordingly, an ac radiation can be converted into a dc current density by the joint action of the radiation electric field and the electrostatic potential. This type of ratchets excited by

THz radiation has been observed in numerous systems, such as bilayer [14,17,23,95] or monolayer [4,8,96] graphene, and quantum wells [1,3,5–7,9,13,15,18].

2.3.1 Phenomenology

Already in 1998, Blanter and Büttiker proposed a system in which an optoelectronic ratchet effect can be implemented [97]. They theoretically investigated a superlattice (SL) illuminated by light trough a mask that has the same period d as the SL but is phase shifted with respect to the SL, as depicted in Fig. 2.5(a). The force acting on the carriers is given by [19]

$$F(x,t) = -\frac{\mathrm{d}V(x)}{\mathrm{d}x} + eE(x,t)\,, \tag{2.26}$$

where x is the modulation direction and $V(x)$ the electrostatic potential. $E(x,t)$ is the radiation electric field passing trough the mask. This heats the electron gas locally and gives rise to a periodic temperature profile. As a result, the inhomogeneous temperature profile is phase shifted with respect to $\mathrm{d}V(x)\,/\,\mathrm{d}x$, which translate into a dc ratchet current. This effect is polarisation-independent and referred to as Seebeck ratchet.

Since its introduction, many adaptions of the Blanter and Büttiker model have been investigated, such as 1D arrays of grooves etched into the top cap of a semiconductor heterostructure [18] or 1D modulation by asymmetric gate fingers [1,8]. The 2D model system in this section is a 1D lateral gate superlattice superimposed on a homogeneous 2D electron system (2DES), as investigated in a comb-like dual-grating-

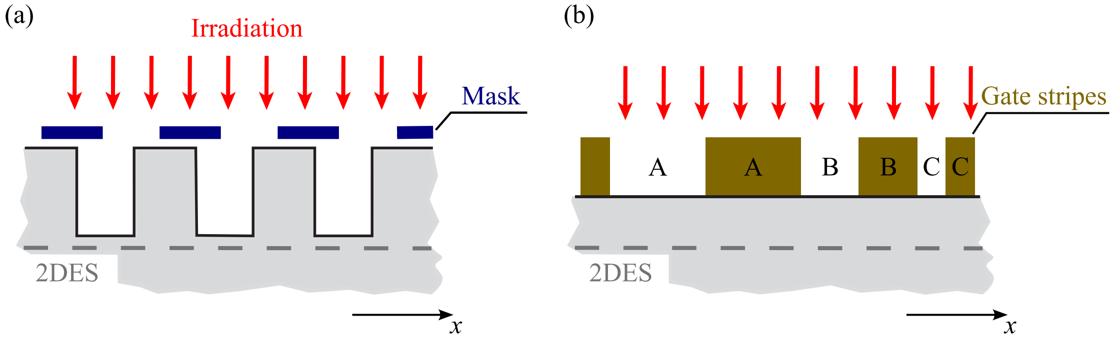

Figure 2.5 | Different realisations of a 1D ratchet in 2D systems. The modulation is in x-direction. Panel (a) sketches the geometry considered by Blanter and Büttiker. A superlattice is irradiated trough a mask that has the same period than the superlattice but is phase shifted. Panel (b) shows the supercell of metallic gate stripes placed onto a homogeneous 2DES; same capital letters describe holes/stripes with the same width. Adapted from Ref. [1].

gate. The following theory is adapted from Refs. [2,18,19]. The modulation in x-direction is achieved by depositing gate stripes in an asymmetric configuration, as shown in Fig. 2.5(b). Furthermore, the model system hosts carriers with parabolic energy dispersion.

The following description of the model predicts that ratchet currents can be generated due to incident light being diffracted on the metal gate stripes. Due to the periodicity of these stripes, it is constructive to expand the near-field $\boldsymbol{E}(x)$ and the potential $V(x)$, which have the period d of the SL, in Fourier series [19]:

$$\boldsymbol{E} = \boldsymbol{E}_0 \left[1 + \sum_n \mathcal{E}_n \cos\left(nqx + \phi_{\mathcal{E}_n}\right)\right] \approx E_0 \left[1 + \mathcal{E}_1 \cos(qx + \phi_{\mathcal{E}})\right] , \tag{2.27}$$

$$V(x) = \sum_n \mathcal{V}_n \cos\left(nqx + \phi_{\mathcal{V}_n}\right) \approx \mathcal{V}_1 \cos\left(qx + \phi_{\mathcal{V}}\right) , \tag{2.28}$$

with $q = 2\pi/d$. The expansions are approximated by taking only one mode into account. One can show that the photocurrent in x-direction is proportional to [2,19]

$$\Xi = |\boldsymbol{E}_0|^2 \sum_n nq\mathcal{E}_n\mathcal{V}_n \sin\left(\phi_{\mathcal{E}_n} - \phi_{\mathcal{V}_n}\right) \approx |\boldsymbol{E}_0|^2 q\mathcal{E}_1\mathcal{V}_1 \sin\left(\phi_{\mathcal{E}} - \phi_{\mathcal{V}}\right) , \tag{2.29}$$

where Ξ is referred to as lateral asymmetry parameter. It can be seen from Eq. (2.29) that the photocurrent: (i) is only non-vanishing if the modulations of the potential and the electric field are phase shifted; (ii) is tunable by the geometry of the gate stripes and the applied gate voltage; (iii) increases with decreasing SL period; and (iv) is proportional to the square of the incident radiation electric field.

Phenomenologically, the ratchet current has to be invariant at the same symmetry operations allowed by the geometry of the system. The model system has C_s symmetry, and therefore it has only one non-trivial symmetry operation: the mirror plane in the (zx)-plane. As a consequence, the ratchet current $\boldsymbol{j} = (j_x, j_y)$ transforms after the mirror operation into $\boldsymbol{j}' = (j_x, -j_y)$. Hence, the current components are [2,18]

$$j_x = \Xi\chi_1(|e_x|^2 - |e_y|^2) + \Xi\chi_0 \, , \tag{2.30}$$

$$j_y = \Xi\chi_2(e_x e_y^* + e_x^* e_y) \, , \tag{2.31}$$

i.e. linear combinations of Stokes parameters; see Sec. 3.2.2.. The prefactors $\chi_{0,1,2}$ depend on the concrete system and are gained for the considered model system below. Note that in C_s symmetry, j_y can be generated by circular polarisation, which adds the term $j_y \propto \Xi P_{\text{circ}}$. This term is omitted.

2.3.2 Kinetic theory

In this section, the aforementioned model system is elaborated in a microscopic theory following Refs. [1,18,19,98].

An established approach for analysing ratchets is the Boltzmann kinetic equation for the electron distribution function $f_{\boldsymbol{k}}(x,t)$:

$$\left[\frac{\partial}{\partial t} + \boldsymbol{v}_{\boldsymbol{k},x}\frac{\partial}{\partial x} + \frac{\boldsymbol{F}(x,t)}{\hbar}\cdot\nabla_{\boldsymbol{k}}\right] f_{\boldsymbol{k}}(x,t) + Q_{\boldsymbol{k}} = 0\,, \tag{2.32}$$

with the force $\boldsymbol{F}(x,t) = -\frac{\mathrm{d}V(x)}{\mathrm{d}x} + e\boldsymbol{E}(x,t)$ and the collision integral $Q_{\boldsymbol{k}}$, which takes into account energy and momentum relaxation. Equation (2.32) is applicable if: (i) the electron wave vector k is significantly larger than the reciprocal lattice period, $k \gg 2\pi/d$; and (ii) if the electron energy exceeds both the potential modulation and the photon energy, $E_{\boldsymbol{k}} \gg |V(x)|, \hbar\omega$. The photocurrent can be obtained by taking the sum

$$\boldsymbol{j} = 2e\sum_{\boldsymbol{k}} \boldsymbol{v}_{\boldsymbol{k}} \left\langle f_{\boldsymbol{k}}(x,t)\right\rangle_{x,t} \tag{2.33}$$

with averaging the electron distribution function over x and t, and using $\boldsymbol{v}_{\boldsymbol{k}} = \hbar\boldsymbol{k}/m^*$ for parabolic dispersion. Note that the numeric prefactor is a product of the spin degeneracy $\mathrm{g_s} = 2$ and the valley degeneracy, which is assumed to be $g_{\mathrm{v}} = 1$.

In order to solve Eq. (2.32), the collision integral $Q_{\boldsymbol{k}}$ is modelled by a sum of an energy relaxation term Q_{E} and an elastic scattering term $Q_{\boldsymbol{k}}^{\mathrm{e.s.}} = \left[f_{\boldsymbol{k}}(x,t) - \left\langle f_{\boldsymbol{k}}(x,t)\right\rangle_{\boldsymbol{k}}\right]/\tau$, where the momentum relaxation time τ is constant and angular brackets denote averaging over directions of the 2D wave vector $\boldsymbol{k}$. Furthermore, the distribution function of the electron ensemble is expanded up to the second order in the radiation electric field $\boldsymbol{E}$ in the limit of high temperatures and a non-degenerate electron gas:

$$f_{\boldsymbol{k}}^{(0)}(x) = \left(1 - \frac{V(x)}{k_{\mathrm{B}}T}\right)\exp\left(\frac{\mu_0 - E_{\boldsymbol{k}}}{k_{\mathrm{B}}T}\right), \tag{2.34}$$

$$f_{\boldsymbol{k}}^{(1)}(x,t) = -|e|\tau\left(\frac{\mathrm{d}f_{\boldsymbol{k}}^{(0)}}{\mathrm{d}E_{\boldsymbol{k}}}\right)\boldsymbol{E}\cdot\boldsymbol{v}_{\boldsymbol{k}} + \mathrm{c.c.}\,, \tag{2.35}$$

$$f_{\boldsymbol{k}}^{(2)}(x,t) = e^2\tau^2 v^2\left(\frac{\mathrm{d}^2 f_{\boldsymbol{k}}^{(0)}}{\mathrm{d}E_{\boldsymbol{k}}^2}\right)|\boldsymbol{E}|^2\cos(2\phi_{\boldsymbol{k}} - 2\alpha)\,. \tag{2.36}$$

Here, μ_0 is the chemical potential, $E_{\boldsymbol{k}}$ the electron energy, and T the equilibrium temperature. The angles $\phi_{\boldsymbol{k}}$ and α are the polar angle of the corresponding electron momenta and the azimuth angle of $\boldsymbol{E}$ with respect to the x-direction, respectively.

It can be seen that the first-order term is time dependent and that in the second-order term only the time-independent part has to be taken into account. Using this expansion of the distribution function, it can be shown that the photocurrent reads

$$\boldsymbol{j} = \mu_\mathrm{e} \left\langle \delta N(x) \frac{\mathrm{d}V(x)}{\mathrm{d}x} \right\rangle_x \hat{\boldsymbol{x}} \; + \; 2\mu_\mathrm{e}|e| \,\mathrm{Re}\left\{ \left\langle \boldsymbol{E}^*_\omega(x) \delta N_\omega(x) \right\rangle_x \right\} , \tag{2.37}$$

with the mobility μ_e, $\delta N(x) = 2\sum_{\boldsymbol{k}} f^{(2)}_{\boldsymbol{k}}(x)$, and $\delta N_\omega(x) = 2\sum_{\boldsymbol{k}} f^{(1)}_{\boldsymbol{k}}(x)$. In Eq. (2.37) it is assumed that (i) the energy relaxation time is much larger than the momentum relaxation time and the reciprocal radiation frequency, (ii) the superlattice period d is much larger than the mean free path and the energy-diffusion length, and (iii) ac diffusion in the first order is neglected.

The first term in Eq. (2.33) is the polarisation-independent Seebeck ratchet effect. Physically, it can be regarded as inhomogeneous heating of the electron gas by the near-field diffraction of the incoming radiation at the metallic edges of the stripes, leading to a variation in the spatial temperature profile, and consequently to diffusion. The enhancement in temperature can be described by the balance equation

$$k_\mathrm{B} \frac{T(x) - T}{\tau_\mathrm{T}} = \hbar\omega g(x) , \tag{2.38}$$

τ_T is the temperature relaxation time. Here,

$$g(x) = \frac{2e^2}{m^*} \frac{\tau}{1 + (\omega\tau)^2} \frac{|\boldsymbol{E}|^2}{\hbar\omega} \tag{2.39}$$

is the photon absorption rate per electron. This Drude-like absorption promotes changes in the carriers' energy that can be transferred to the lattice, for example by electron-phonon scattering. Whereas for high lattice temperatures this coupling causes a fast thermal equilibrium, at low temperatures the electron temperature can significantly exceed the lattice temperature [76]. Using Ohm's law $\boldsymbol{j} = \sigma\boldsymbol{E}$, replacing $\boldsymbol{E} \to -(1/e)\,\mathrm{d}V(x)\,/\,\mathrm{d}x$ and $\sigma \to \delta\sigma(x) = \partial\sigma/\partial T\,\delta T(x)$, and using Eqs. (2.38) and (2.39) the Seebeck ratchet current can be expressed as

$$j^\mathrm{S}_x = \frac{2\tau_\mathrm{T} e}{m^* k_\mathrm{B}} \frac{\partial\sigma}{\partial T} \frac{\tau}{1 + (\omega\tau)^2} \left\langle |\boldsymbol{E}_0|^2 \frac{\mathrm{d}V(x)}{\mathrm{d}x} \right\rangle_x . \tag{2.40}$$

The factor

$$\Xi = \left\langle |\boldsymbol{E}_0(\boldsymbol{r})|^2 \frac{\mathrm{d}V(x)}{\mathrm{d}x} \right\rangle_x \tag{2.41}$$

coincides with Eq. (2.29). This lateral asymmetry parameter is the key quantity in regards of describing optoelectronic ratchet effects and takes into account the product of the squared near-field amplitude $\boldsymbol{E}_0$ and the derivative of the electrostatic potential $\mathrm{d}V(x)/\mathrm{d}x$, averaged over the x-coordinate. The near-field radiation has a spatial dependence similar to that of the potential but has to differ in phase, as already addressed in Eq. (2.29).

The expression in the microscopic theory in Eq. (2.40) is associated with the phenomenological current [see also Eq. (2.30)] as

$$j_x^{\mathrm{S}} = \Xi \chi_0 \tag{2.42}$$

with χ_0 containing the properties of the material, such as scattering mechanisms. The temperature dependence of the conductivity in a parabolic quantum well (QW) is given by [2]

$$\left(\frac{\partial \sigma}{\partial T}\right)_{\mathrm{QW}} = \frac{\pi e^2}{3\hbar^2} T(E_{\boldsymbol{k}}\tau_1)''_{E_{\boldsymbol{k}}=E_{\mathrm{F}}} \,, \tag{2.43}$$

where primes indicate differentiation with respect to the electron energy $E_{\boldsymbol{k}}$ and $\tau_1 = \tau_1(E_{\boldsymbol{k}})$ the momentum relaxation time of the non-equilibrium correction to the distribution function. In total, the Seebeck ratchet in Eq. (2.40) scales as e^3, and therefore the current changes sign when changing the charge carrier type from electrons to holes.

The second term in Eq. (2.37) is polarisation dependent. It can be shown that in first order in the potential, $\delta N_\omega(x)$ is given as [1]

$$\delta N_\omega(x) = \frac{ieN_0}{\omega m^* k_{\mathrm{B}} T} \frac{\tau}{1 - i\omega\tau} \frac{\mathrm{d}V(x)}{\mathrm{d}x} E_{x,0} \,. \tag{2.44}$$

Inserting Eq. (2.44) into Eq. (2.37) results in the azimuth angle–dependent photocurrent

$$j_x^{\alpha} = \Xi \chi_1 \left(|e_x|^2 - |e_y|^2\right) \,, \tag{2.45}$$

where χ_1 is again material dependent and the expression in brackets is the Stokes parameter P_1; see Sec. 3.2.2.

2.4 Cyclotron resonance

The physics of cyclotron resonance (CR) can be treated in a quasi-classical or a quantum mechanical picture. The latter is essential in order to explain effects associated with phenomena at high magnetic fields, such as Shubnikov–de Haas oscillations (SdHO) or the quantum Hall effect.

2.4.1 Quasi-classical treatment

As it is physically more graspable and illustrative, CR is first described in the semi-classical treatment in a two-dimensional electron system that hosts charge carriers with an isotropic and parabolic dispersion. If carriers with charge q and effective mass m^* are subjected to a magnetic field $\boldsymbol{B}$ orientated perpendicular to the plane, the Lorentz force causes the carriers to orbit in circular trajectories with the cyclotron frequency [99–101]

$$\omega_\mathrm{c} = \frac{q|\boldsymbol{B}|}{m^*} \,. \tag{2.46}$$

In the reciprocal $\boldsymbol{k}$-space, the carriers move with frequency ω_c on surfaces of constant energy that are orthogonal to the magnetic field [100,101].

Exciting the 2DEG with an electromagnetic wave at normal incidence, the semi-classical equation of motion for these carriers experiencing both a B-field and a radiation E-field can be expressed in the Drude model as [101,102]

$$m^* \frac{\mathrm{d}\boldsymbol{v}}{\mathrm{d}t} = q\left(\boldsymbol{E} + \boldsymbol{v} \times \boldsymbol{B}\right) - \frac{m^*\boldsymbol{v}}{\tau} \,, \tag{2.47}$$

where the term with the momentum relaxation time τ takes into account scattering. The absorbed power density can be written with Joule's loss formula by time-averaging the real part of the product of the current density $\boldsymbol{j} = -ne\boldsymbol{v}$ and the radiation electric field:

$$P = \Big\langle \mathrm{Re}\{\boldsymbol{j}\} \cdot \mathrm{Re}\{\boldsymbol{E}\} \Big\rangle_t = \frac{1}{2}\,\mathrm{Re}\{\boldsymbol{j} \cdot \boldsymbol{E}^*\} \,, \tag{2.48}$$

where $\boldsymbol{E}^*$ denotes the complex conjugate. In case of right-handed (σ^+) or left-handed (σ^-) circularly polarised light the corresponding absorbed power densities read as [101,102]

$$P_\pm = \sigma_0 E_0^2 \frac{1}{1 + \left(\omega \pm \omega_\mathrm{c}\right)^2 \tau^2} \,, \tag{2.49}$$

with the dc conductivity $\sigma_0 = ne^2\tau/m^*$, the carrier density n, and the amplitude E_0 of the radiation electric field. The power density in Eq. (2.49) exhibits a pronounced Lorentz-shaped resonance peak if $\omega_c\tau \gg 1$, i.e. the momentum relaxation time must exceed the period of the cyclotron motion [100,103]. Resonant absorption can be observed only if the helicity of the radiation matches the sense of cyclotron motion. Consequently, for left-handed polarised light electrons (holes) absorb radiation resonantly for positive (negative) polarity of $B = B_c$, and vice versa for right-handed polarised light. For this reason, CR is a useful opportunity to identify the carrier type, the effective mass, and the momentum relaxation time of carriers in a 2DES [100,102].

Note that the absorbed power density for linearly polarised light is given by [102,103]

$$P_{\mathrm{lin}} = \frac{1}{4}\sigma_0 E_0^2 \left[\frac{1}{1 + (\omega + \omega_c)^2 \tau^2} + \frac{1}{1 + (\omega - \omega_c)^2 \tau^2} \right] , \tag{2.50}$$

implying that the CR condition is fulfilled for both B-field polarities, irrespective of whether electrons or holes are considered. The factor 1/4 emerges because the root mean square electric field of the linearly polarised wave is smaller by a factor $\sqrt{2}$ than the one of the circularly polarised wave. This translates into the intensities $I = E_0^2/(2Z_0)$ for linearly and $I = E_0^2/Z_0$ for circularly polarised light, where $Z_0 = 1/(\epsilon_0 c) \approx 377\,\Omega$ is the vacuum impedance.

2.4.2 Quantum mechanical treatment

In contrast to the semi-classical approach, the quantum-mechanical treatment involves electron trajectories that are quantised [100]. In quantum mechanics, CR is the resonant direct optical transition between Landau levels [103]. These discrete, quantised levels can be found as eigenvalues of the Schrödinger equation for a charge carrier in a 2DES with parabolic dispersion, subjected to an out-of-plane magnetic field [100]:

$$H\psi = \frac{1}{2m^*} \left(-i\hbar\nabla + e\boldsymbol{A} \right)^2 \psi = E\psi \, . \tag{2.51}$$

Here, the magnetic field $\boldsymbol{B} = B\,\hat{\boldsymbol{z}}$ is expressed by the vector potential $\boldsymbol{A} = (0, xB, 0)$ using the Landau gauge. The Schrödinger equation takes then the form

$$\frac{\partial^2\psi}{\partial x^2} + \frac{\partial^2\psi}{\partial z^2} + \left(\frac{\partial}{\partial y} + \frac{ieBx}{\hbar} \right)^2 \psi + \frac{2m^* E}{\hbar}\psi = 0 \, . \tag{2.52}$$

The ansatz $\psi = \tilde{\psi} \exp\left[-i(k_y y + k_z z)\right]$ involves plane waves in the y- and z-directions, and hence [100,104]:

$$\frac{\partial^2 \tilde{\psi}}{\partial x^2} + \left[\frac{2m^* E}{\hbar^2} - k_z^2 - \left(\frac{eBx}{\hbar} - k_y\right)^2\right] \tilde{\psi} = 0\,. \tag{2.53}$$

Now, introducing

$$E_l = E - \frac{\hbar^2 k_z^2}{2m^*}\,, \tag{2.54}$$

$$\tilde{x} = x - \frac{\hbar k_y}{eB}\,, \tag{2.55}$$

and using $\omega_\mathrm{c} = eB/m^*$, Eq. (2.53) can be rewritten as [100]

$$\frac{\partial^2 \tilde{\psi}}{\partial \tilde{x}^2} + \frac{2m^*}{\hbar^2}\left[E_l - \frac{1}{2} m^* \omega_\mathrm{c}^2 \tilde{x}^2\right] \tilde{\psi} = 0\,. \tag{2.56}$$

This is the Schrödinger equation of a linear, harmonic oscillator with frequency ω_c with center at

$$\tilde{x}_0 = \frac{1}{\omega_\mathrm{c}} \frac{\hbar k_y}{m^*}\,. \tag{2.57}$$

The eigenenergies are thus [100,103]

$$E = E_l + E(k_z) = \left(l + \frac{1}{2}\right) \hbar\omega_\mathrm{c} + \frac{\hbar^2 k_z^2}{2m^*}\,, \tag{2.58}$$

with integer l and $l \geq 0$. It can be seen that in the presence of a magnetic field, the parabolic bands split into subbands, the Landau levels [100]. Equation (2.58) yields that for a parabolic band structure, the Landau levels are equidistant, where optical transitions are allowed only between neighbouring levels because of dipole selection rules [100]. Figure 2.6 depicts the Landau levels for parabolic [Fig. 2.6(a)] and linear [Fig. 2.6(b)] dispersion. In the case of the linear band structure, the Landau level spectrum is described by [105–107]

$$E_l = \mathrm{sgn}\,(l) \hbar v_0 \sqrt{\frac{2eB|l|}{\hbar}}\,, \tag{2.59}$$

where $l \in \mathbb{Z}$ and $l > 0$ ($l < 0$) belong to Landau levels in the conduction (valence) band [108]. Equation (2.59) implies that adjacent Landau levels are not equidistant anymore but scale as

$$\Delta E_l = \hbar\omega = \hbar v_0 \sqrt{\frac{2eB}{\hbar}} \left[\mathrm{sgn}\,(l+1)\sqrt{|l+1|} - \mathrm{sgn}(l)\sqrt{|l|} \right] . \tag{2.60}$$

In contrast, in the quasi-classical limit in which $E_\mathrm{F} \gg \hbar\omega_\mathrm{c}$, ω_c roughly scales linear with the magnetic field; see Eq. (2.46). These two regimes are shown in Fig. 2.6(b). However, the effective mass, which is zero for massless fermions, is replaced by the cyclotron mass $m_\mathrm{c} = E_\mathrm{F}/v_0^2 = \hbar\sqrt{\pi n}/v_0$, which depends on the carrier density [67,107]. Subsequently, in particular because the magneto-optic experiments with graphene were conducted with fixed excitation frequency, the position for the resonant magnetic field is given by

$$B_\mathrm{c} = \frac{\hbar\omega\sqrt{\pi n}}{e v_0} . \tag{2.61}$$

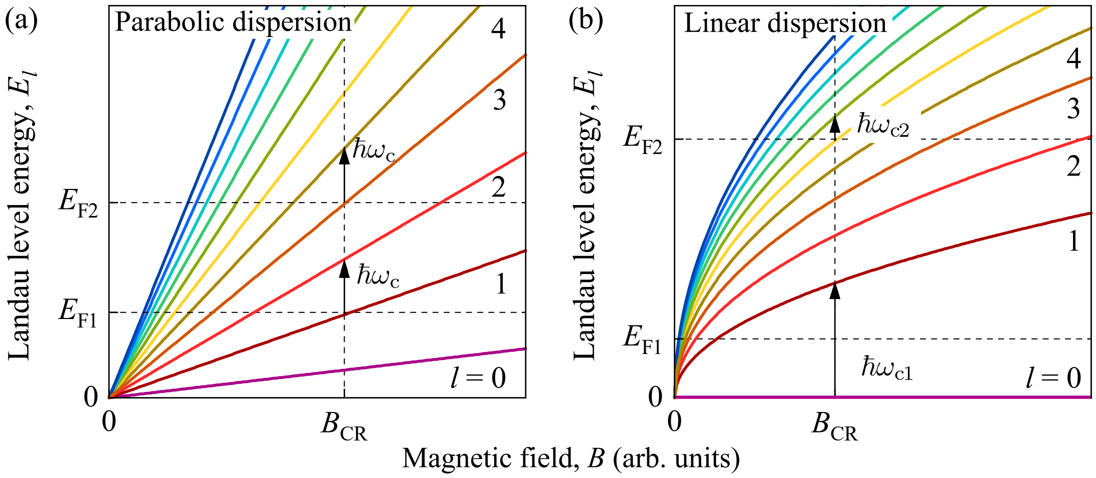

Figure 2.6 | Panel (a) shows the Landau levels E_l for parabolic dispersion according to Eq. (2.58) for $l = 0 \ldots 10$. For a fixed magnetic field neighbouring Landau levels are equidistant, independent of the position of the Fermi level. Panel (b) shows the spectrum for the same values of l for linear dispersion according to Eq. (2.60) for the conduction band regime. Shown are transitions for the quantum regime $E_{\mathrm{F1}} < \hbar\omega_{\mathrm{c1}}$ in which $\omega_\mathrm{c} \propto \sqrt{B}$, and for the quasi-classical limit $E_{\mathrm{F2}} \gg \hbar\omega_{\mathrm{c2}}$ in which $\omega_\mathrm{c} \propto B$. Adapted from Refs. [109,110].

3 Methods and samples

This chapter describes the laser setup used in the experiments and the investigated samples. The first section outlines how THz lasing is achieved. In this context, the working principle of a CO_2 laser and a molecular gas laser is explained. Subsequently, the second section documents the experimental setup used to collect electrical transport data and optoelectronic photosignals. Finally, details are given on the production and the properties of the investigated graphene- and Co/Pt-based metamaterials.

3.1 THz laser source

For the optical experiments a molecular gas laser was used, which operates in the far-infrared (FIR), i.e. the terahertz spectral range. In such systems, lasing is accomplished by converting mid-infrared radiation (MIR) into FIR. This is done by a CO_2 laser that optically excites the vibrational-rotational modes of the molecules in the molecular gas laser [111]. In this work, both lasers operate in the continuous wave (cw) regime and provide monochromatic radiation.

3.1.1 CO_2 laser

The gas mixture in the CO_2 laser resonator consists of carbon dioxide (CO_2, 7 %), nitrogen (N_2, 18 %), and helium (He_2, 75 %). Because CO_2 is a linear molecule with $N = 3$ atoms, it has $3N - 5 = 4$ vibrational modes [112]: a symmetric (n_1) and an asymmetric (n_3) stretching mode , and a twice-degenerate bending mode (n_2), as shown in Fig. 3.1(a). Hence, the vibration state of a CO_2 molecule can be described by the tuple (n_1, n_2^l, n_3), with the occupation number n_i of the corresponding mode i, and the degeneracy l. Alike CO_2, N_2 is linear but has $N = 2$ atoms, and thus one vibrational mode only. The energy schemes of CO_2 and N_2 are illustrated in Fig. 3.1(b).

Applying a high-voltage (in the experimental setup of about 16 kV) leads to a longitudinal, electrical discharge giving rise to the excitation of the N_2 molecules. It can be seen that the energies of the excited vibrational mode ($\nu = 1$) of N_2 and the asymmetric vibration mode (00^01) of CO_2 differs by 2.2 meV only. This

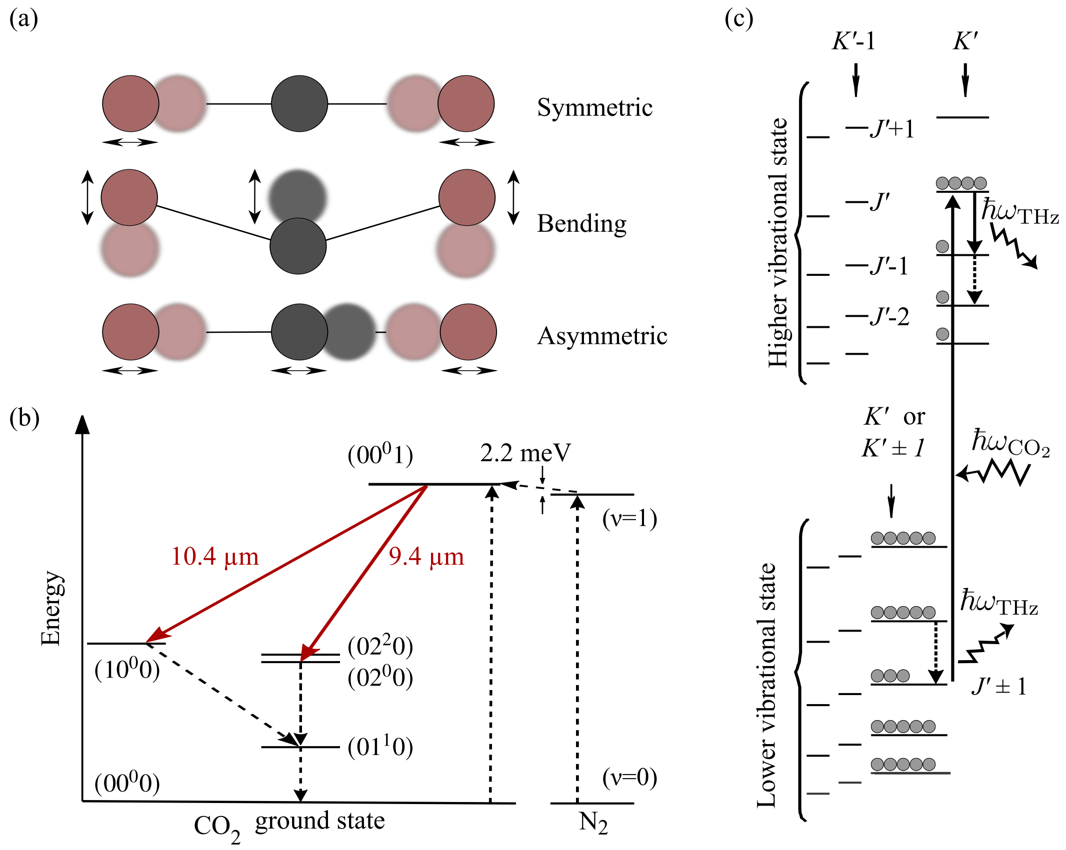

Figure 3.1 | Sketches for lasing of the used infrared range. Panel (a) shows all vibrational modes of a CO_2 molecule, with oxygen atoms being red and carbon atoms black. Full and reduced opacity indicate the two elongations of the oscillations. Panel (b) illustrates the corresponding energy level scheme, including the one of N_2. Panel (c) shows n the vibrational-rotational energy scheme for a prolate symmetric top molecule, where circles indicate occupation. The quantum number J is the angular momentum and K its projection. After Ref. [111].

small difference allows for energy transfer from the N_2 to the CO_2 molecules by collisions: electron–N_2 collisions excite N_2 molecules, which in turn collide with CO_2, and subsequently N_2 molecules relax to their ground state. In this way, population inversion can be achieved and optical transitions (9.4 µm and 10.4 µm) between vibrational energy states of CO_2 become possible. Also, direct excitation of CO_2 molecules are allowed; nevertheless, the described indirect transition dominates. Furthermore, lasing via N_2 is more efficient, since N_2 atoms have a small mass and are metastable because they lack a permanent dipole moment, which leads to a long lifetime [114]. The (10^00)-state couples with the (02^l0)-state in consequence to the Fermi resonance, which appears as the bending mode have the tendency to induce a symmetric stretching mode [114], allowing for depopulating the lower laser level. The whole lasing process in the MIR laser is improved by the admixed helium, which helps to deplete the lower CO_2 vibrational levels and also their thermal population.

Note that the energy levels are also split in rotational levels of the P- and R-branches, and that the selection rules forbid a Q-branch; for further information, see, e.g. Refs. [111,115].

3.1.2 Molecular gas laser

Whereas the MIR CO_2 laser lines are based on combined vibrational and rotational modes, the laser lines of the FIR molecular gas laser are purely related to rotational transitions. The pump photon energy must coincide with the vibrational-rotation levels of the molecules in the FIR cavity. However, Raman scattering enables lasing also in case of small mismatches. Figure 3.1(c) shows an example for a prolate symmetric top molecule transition scheme in which vibrational modes are split into bands due to the angular momentum J and its projection K onto the molecule's symmetry axis. The pump CO_2 radiation excites the vibrational-rotation modes of the FIR molecules. Consequently, THz radiation can be obtained by rotational transitions in both the higher and lower vibrational energy band owing to population inversion in both bands. In order for lasing to occur, the active media in the FIR resonator has to posses a permanent electric dipole moment. Furthermore, for population inversion the involved vibrational levels should have a long lifetime [111].

Figure 3.2 shows the coupling between the pump and the molecular gas laser. The frequency of the CO_2 pump radiation can be tuned by an echelette diffraction grating placed in the cavity and yields optical powers up to 50 W. The CO_2 beam is focused

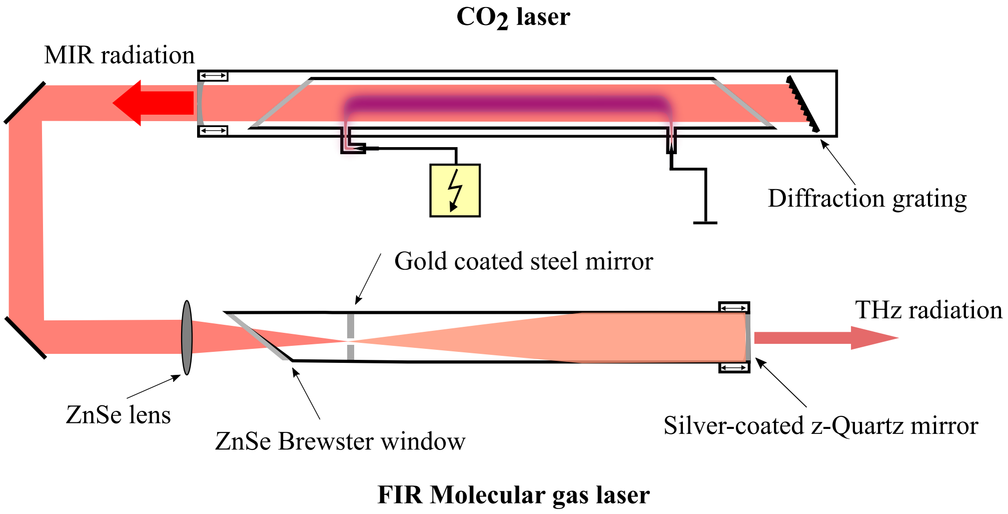

Figure 3.2 | Schematic setup of an optically pumped molecular gas laser. An electrically pumped CO_2 laser, which wavelength can be adjusted by a diffraction grating, excites vibrational-rotational levels of the molecular gas in the FIR resonator. Adapted from Ref. [113]

by a zinc selenide (ZnSe) lens and guided into the FIR laser cavity through a ZnSe Brewster window, ensuring linearly polarised light. The THz radiation in the FIR cavity can be coupled out by a silver-coated z-cut quartz mirror, which also reflects the pump radiation back into the cavity. The THz radiation output has tens to hundreds of milliwatts.

3.2 Experimental setup

Figure 3.3 depicts the setup used in the experiments. The THz radiation output beam is divided into two parts by a beam splitter. The reflected part is modulated by a mechanical chopper and is focused on an off-axis parabolic mirror to a pyroelectric reference detector in order to monitor the radiation power during the measurements. The electrical signal of this detector is proportional to the radiation power and has to be calibrated to the transmitted power in advance. The reference signal is coupled to a piezoelectric stabiliser, which minimises the power fluctuations substantially.

The transmitted part is also modulated by a mechanical chopper and passes optical auxiliary elements. Subsequently, another off-axis parabolic mirror focuses the beam into an optical cryostat (Oxford Spectromag); see orange dashed rectangle in Fig. 3.3. This has three chambers: the outer one for nitrogen, the mid one for helium, and the inner one for the sample. The superconducting coils in the helium bath chamber enables magnetic fields up to $\pm 7\,\mathrm{T}$, and are connected to the sample chamber by a needle valve, which allows for cooling slowly and homogeneously. The outer windows of the cryostat are covered with thin black polyethylene foils, which keep ambient room light and near-infrared radiation but not the THz radiation from exposing the sample. For some experiments at room temperature, a water-cooled electromagnet with fields up to $B = \pm 0.5\,\mathrm{T}$ was used; see dashed blue box on the right-hand side in Fig. 3.3.

3.2.1 Laser beam characteristics and measurement technique

In this work the two different THz-regime wavelengths $118\,\mu\mathrm{m}$ and $432\,\mu\mathrm{m}$ were used by employing the active laser media methanol (CH_3OH) and formic acid (CH_2O_2), respectively. Since homogeneous irradiation of the sample is a crucial prerequisite for optoelectronic ratchet effects, see Chap. 2, a Gaussian-like beam shape was aimed, and the beam profile was detected with a pyroelectric camera commonly used for the FIR spectral range [116,117]. In the top left corner in Fig. 3.3 the spatial intensity distribution of the THz beam is shown exemplarily for the wavelength $118\,\mu\mathrm{m}$. The spot sizes are given by the full width at half maximum being $1.5\,\mathrm{mm}$ ($118\,\mu\mathrm{m}$) and

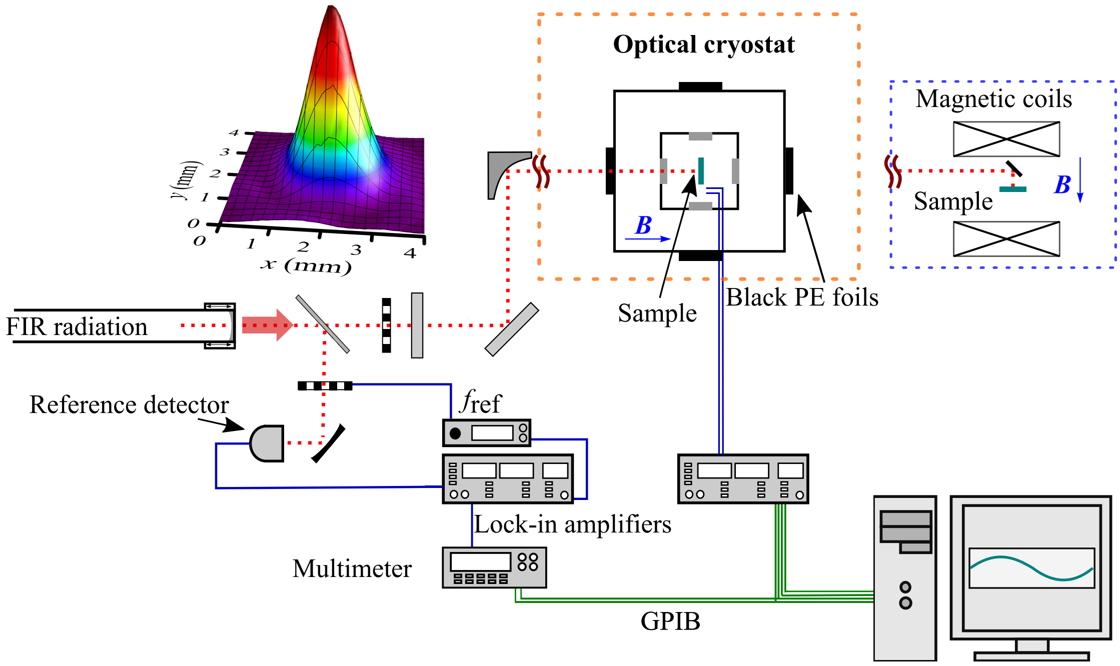

Figure 3.3 | Top left: spatial distribution of the Gaussian-like laser spot captured with a pyroelectric camera for a wavelength of 118 µm. Experimental setup: A beam splitter reflects one fraction to a reference detector for monitoring radiation power. The main part, modulated by an optical chopper, propagates to optical elements, and is subsequently focused on the sample. In some experiments, the cryostat is replaced by room-temperature magnetic coils, i.e. the setup in the dashed orange box is replaced by the setup in the dashed blue box. Adapted from Ref. [113].

3.1 mm (432 µm). The beam powers were 40 mW and 15 mW, respectively. Table 3.1 gives an overview of the FIR wavelengths used. Note that homogeneous illumination is fulfilled because the beam spots are much larger than the sample size. The experimental data are either normalised to radiation intensity, or to the power incident to the sample,

$$P_\mathrm{s} = P\,A_\mathrm{s}/A_\mathrm{beam}\,. \tag{3.1}$$

Here A_s and A_beam are the area of the sample and the laser beam, respectively. This normalisations take into account small variations in the laser output power.

All measurements were performed via the measurement software LabVIEW. The instruments and the computer-based programme communicated by GPIB (general purpose interface bus). Furthermore, all signals were fed into lock-in amplifiers prior to the recording. Electrical measurements were performed for characterising the investigated samples, namely resistance, carrier density, mobility, and momentum relaxation time. For this purpose, an ac bias current of 10 nA was applied via a load

Table 3.1 | THz frequencies and their corresponding wavelengths, beam diameters, powers, and photon energies. In addition the active gas media and the CO_2 pump lines are listed.

f (THz)	λ (µm)	d (mm)	P (mW)	E_{ph} (meV)	Medium	$\lambda_{\mathrm{CO_2}}$ (µm)
2.54	118	1.5	40	10.5	Methanol	9.965
0.69	432	3.1	15	2.87	Formic acid	9.271

resistance. The graphene samples featured Hall bar geometry, allowing for mostly measuring the four-point resistances R_{xx} and R_{xy}. The Co/Pt-based samples had a simple geometry; thus, only the two-point resistance were measured. For more details on the transport characteristics, see Sec. 3.3. All photosignals were measured by modulating the radiation at 100 Hz, picking up the THz-induced voltage drop across the unbiased sample, pre-amplifying the voltage by the factor 100 and feeding it into the lock-in. In some occasions in the course of this thesis, the photovoltage U is given by the equivalent photocurrent $J = U/R_{\mathrm{s}}$ or photocurrent density $j = U/(R_{\mathrm{s}}w)$, by using the Hall bar width w and the fact that the sample resistance R_{s} is much smaller than the input impedance of the amplifier.

3.2.2 Altering the polarisation state of the radiation

THz-induced photosignals, in particular ratchet photocurrents, can have a strong dependence on the polarisation of the radiation electric field. In order to investigate ratchet effects upon altering polarisation, the initial, linearly polarised electric field vector $\boldsymbol{E}$ was altered to $\boldsymbol{E'}$ by means of $\lambda/2$ and $\lambda/4$ wave plates that are both based on birefringence, as sketched in Fig. 3.4. The working principle of such plates is that the ordinary refractive index n_{o} and the extraordinary one (n_{eo}) are different [118,119]. As a consequence, with respect to the c-axis, the parallel ($\boldsymbol{E}_{\parallel}$) and perpendicular $\boldsymbol{E}_{\perp}$ component experience a different phase shift because of their different phase velocities. This leads to a difference [118,119]

$$\Delta\phi = \frac{2\pi d}{\lambda}(n_{\mathrm{o}} - n_{\mathrm{eo}}) \tag{3.2}$$

in phase, which depends on the thickness d of the material and the wavelength λ of the incident radiation. In case of half-wave plates, $\Delta\phi$ is an odd multiply of π and the initial linearly polarised radiation remains linearly but is rotated after passing the plate by the azimuth angle $\alpha = 2\beta$. Here, β is the rotation angle of the plate's

c-axis with respect to the incoming linearly polarised electric field vector $\boldsymbol{E}$. On the other hand, for quarter-wave plates $\Delta\phi$ is an odd integer of $\pi/2$ and $\boldsymbol{E}'$ becomes in general elliptically polarised when rotating a $\lambda/4$ plate by an angle φ. In the special case $\varphi = 45°$ or $135°$, $\boldsymbol{E}'$ is left- or right-handed circularly polarised, respectively, and if $\varphi = 0°$, $90°$ or $180°$, the polarisation state of $\boldsymbol{E}'$ is identical to the initial one.

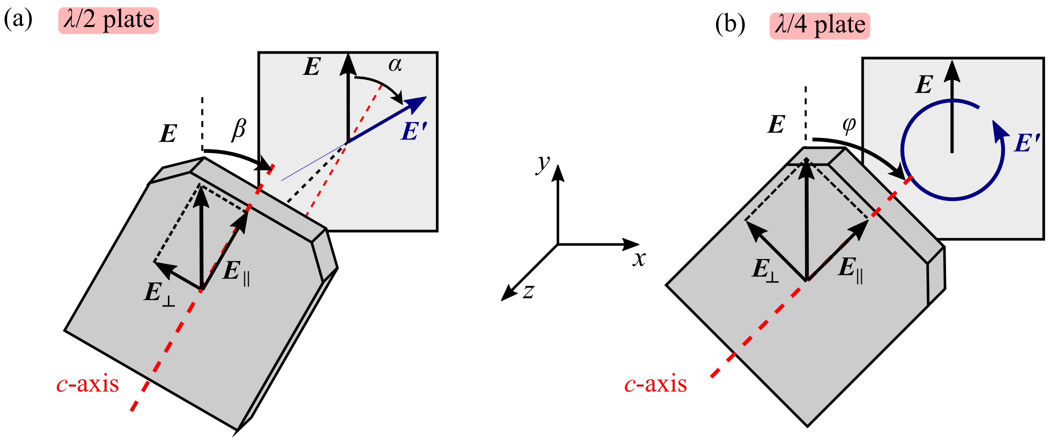

Figure 3.4 | Schematic illustration of the geometry of a $\lambda/2$ (a) and $\lambda/4$ (b) plate. $\boldsymbol{E}$ denotes the incident and $\boldsymbol{E}'$ the modified radiation electric field vector. Panel (a) demonstrates that rotating the c-axis of the plate by an angle β with respect to $\boldsymbol{E}$ results in $\boldsymbol{E}'$ to be rotated by $\alpha = 2\beta$. In contrast, rotating a $\lambda/4$ plate by an angle φ leads to a polarisation state that is in general elliptical. Adapted from Refs. [110,113].

One way to describe the polarisation of plane waves is to introduce the so-called Stokes parameters. This is insofar natural because ratchets are a second-order phenomenon in E, and scale therefore linear with the intensity. Stokes parameters, describing the polarisation state also in terms of intensities, are linear combinations of the Cartesian components of $\boldsymbol{E}$:

$$\begin{aligned}
S_0 &= |E_x|^2 + |E_y|^2\,, \\
S_1 &= |E_x|^2 - |E_y|^2\,, \\
S_2 &= E_x E_y^* + E_x^* E_y\,, \\
S_3 &= i\left(E_x E_y^* - E_x^* E_y\right)\,, \qquad (3.3)
\end{aligned}$$

where asterisk means complex conjugated and i is the imaginary unit number. With respect to the experiments, Eq. (3.3) can be expressed as a function of α [$\lambda/2$ plate] or φ [$\lambda/4$ plate]. In the THz range, the plates for changing the polarisation of the radiation electric beam are typically made of x-cut crystalline quartz as it is transparent for THz and has a pronounced birefringent behaviour [120]. The thickness of the plates is in the order of millimeters. If the initial electric field vector is parallel to the y-axis, the Stokes parameters can be expressed as

$$\begin{aligned} P_1 &= \frac{S_1}{S_0} = -\cos 2\alpha\,, \\ P_2 &= \frac{S_2}{S_0} = -\sin 2\alpha\,, \end{aligned} \tag{3.4}$$

and

$$\begin{aligned} P_1 &= -\frac{\cos 4\varphi + 1}{2}\,, \\ P_2 &= -\frac{\sin 4\varphi}{2}\,, \\ P_3 &= \frac{S_3}{S_0} = P_{\text{circ}} = \sin 2\varphi\,, \end{aligned} \tag{3.5}$$

where $P_{\text{circ}} = [-1, 1]$. $P_{\text{circ}} = \pm 1$ in case of right- and left-handed circularly polarised light, respectively, and $P_{\text{circ}} = 0$ if the beam is linearly polarised. Note that in the course of this work, the Stokes parameters are often written with the unit vector $\hat{\boldsymbol{e}}$ of $\boldsymbol{E} = E\hat{\boldsymbol{e}}$, reading, e.g. $P_1 = |e_x|^2 - |e_y|^2$.

3.3 Investigated samples

In the framework of this thesis, the THz-induced ratchet effect has been investigated with two different 2D metamaterials, which are graphene incorporating a gate-tunable lateral superlattice allowing for carrier and potential modulation, and a Co/Pt stacked ferromagnetic metal that exhibits holes in the material itself. Either way, the holes in the patterned graphite gate as well as in the Co/Pt are triangular and are designed to be arranged in an array. The array of the graphene samples' gate is quadratic, whereas in the Co/Pt metal it is hexagonal. The physical fundamentals for both sample types have been pointed out in Chap. 2 showing the most crucial difference that graphene has a linear energy dispersion, whereas Co/Pt has a parabolic one.

3.3.1 Graphene-based metamaterial

The graphene-based metamaterials were manufactured by Julia Amann from the research group of PD. Dr. Jonathan Eroms / Prof. Dr. Dieter Weiss of the University of Regensburg; see also Refs. [60,121–123] for further information on the sample.

Figure 3.5(a) shows the layer sequence of the samples that are based on a $p^{++}-$doped silicon (Si) chip operating as a back gate used in conventionally gated devices. The dielectric and insulating spacing layer is silicon dioxide SiO$_2$. On top, the key part was deposited – the patterned bottom gate. It consists of graphite (a couple layers of graphene) and was patterned with triangular equilateral holes arranged in a quadratic superlattice. The array was fabricated by electron beam lithography and reactive ion etching with oxygen plasma, yielding a period of $0.6\,\mu$m and a side length of the individual triangles of $1\,\mu$m; see Fig. 3.5(b). Above, a monolayer graphene embedded in hexagonal boron nitride (hBN) was placed. The lower hBN thickness in sample G1 (G2) is about 40 nm (30 nm) and the upper one is 35 nm (30 nm). Finally, the samples were etched into a Hall bar configuration with dimensions of $16\,\mu\text{m} \times 2.5\,\mu\text{m}$ for sample G1, and $11\,\mu\text{m} \times 5\,\mu\text{m}$ for G2, as depicted by the optical microscope images in Fig 3.5(c). Figure 3.5(d) sketches the working principle of the device when a voltage

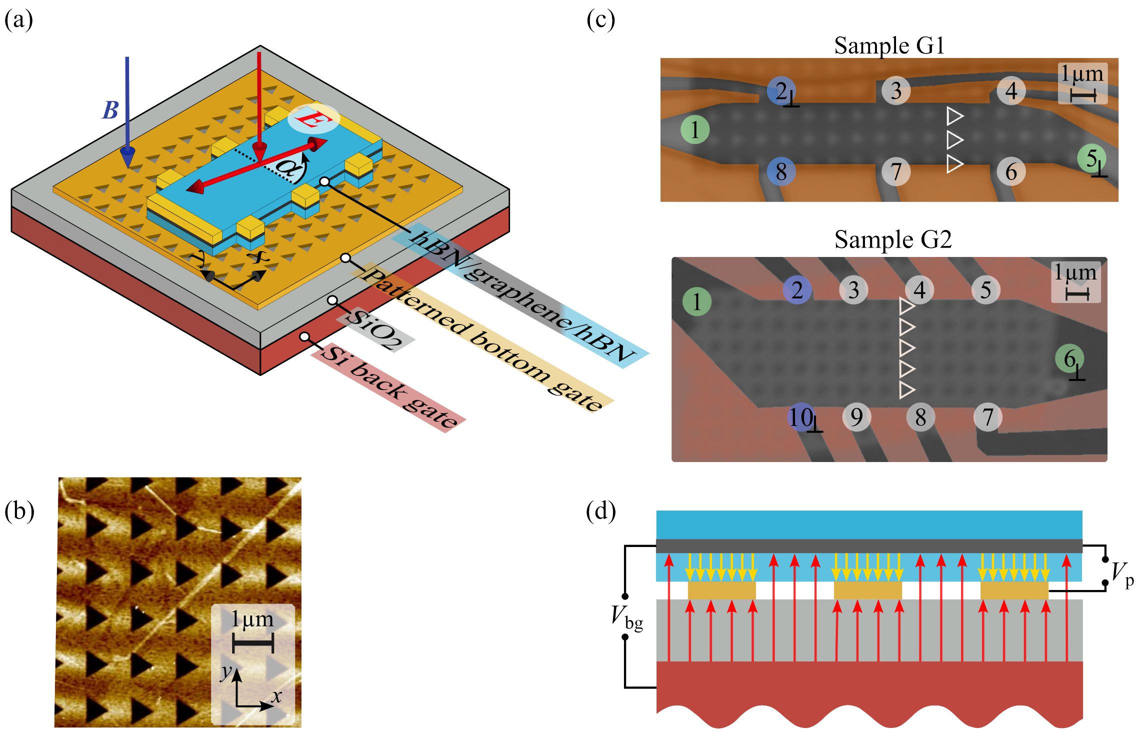

Figure 3.5 | The patterned-gated graphene sample. Panel (a) shows a sample sketch and the experimental setup, in which the magnetic field vector $\boldsymbol{B}$ and the THz beam are applied perpendicularly to the sample surface. The red double arrow indicates the radiation electric field vector that can be rotated anticlockwise by the angle α with respect to the triangles' base, i.e. $\alpha = 0$ corresponds to $\boldsymbol{E} \parallel \hat{\boldsymbol{y}}$. Panel (b) shows an AFM image of the patterned gate. Panel (c) shows microscope images of the used samples G1 and G2 [orange areas are the etching mask overlay], where in each image one row of triangles is highlighted. In (d) a part of the cross section is given and the coloured arrows indicate the electric field caused by the back gate voltage [V_{bg}, red] and patterned gate voltage [V_{p}, yellow] in case both gate voltages have opposite magnitudes. The photovoltages in x- and y-direction were measured along the contact pair (1–$5_\perp$) and (8–$2_\perp$), respectively, with contact 5 and 2 grounded [G1] and (1–$6_\perp$) and (2–$10_\perp$), with 6 and 10 grounded [G2]. Adapted from Refs. [60,121,123].

is applied to both the homogeneous and the patterned back gate. In principle, both back gates can influence the charge carrier concentration and electric potential in graphene. However, due to screening of the back gate potential by the patterned gate, the back gate acts only in regions in graphene inside the triangles, whereas the patterned gate acts in the areas in graphene between the triangles. As a consequence, both the carrier concentration and the potential are modulated, depending on the sign and magnitude of both gate voltages applied, as previously shown in Refs. [60,124] and related to this thesis in Refs. [121–123].

In order to characterise the sample, transport measurements at room temperature were conducted. For this, the lock-in technique was used with an applied bias voltage of 1 V modulated with 11 Hz and a load resistance of 10 MΩ. Figure 3.6(a) shows the two-terminal resistance of sample G1 measured at room temperature and zero magnetic field as a function of the back gate voltage V_bg and the patterned gate V_p. As both gates affect different regions in graphene, complete charge neutrality throughout the sample is the case for $V_\mathrm{bg} = -2.4\,\mathrm{V}$ and $V_\mathrm{p} = -0.15\,\mathrm{V}$, which corresponds to the point where both dash-dotted lines cross. These values are non-zero because of background doping, which can be unintentionally introduced during, e.g. the fabrication of the sample or different cool-down cycles, and due to a built-in potential introduced by the patterned gate. The lines in Fig. 3.6(a) demonstrate the similarity to unmodulated graphene, in which only the Dirac point is present, i.e. keeping one gate fixed results in maxima that appear along the dash-dotted lines. The data show that there are four charge carrier regimes, denoted by n, n^* (electrons) and p, p^* (holes), with plain symbols labelling the carrier concentration between the triangles and the asterisks “$*$” indicating the concentration inside the triangles. When one repeats this measurement for $B = 0.2\,\mathrm{T}$, one can determine the average density across the sample via the Hall resistance slope according to

$$n_\mathrm{D} = (e\Delta R_{xy}/\Delta B)^{-1} \, . \tag{3.6}$$

If $V_\mathrm{bg} = 0$, the carrier density is given by the empirical relation

$$n_\mathrm{D} = 6.3 \times 10^{11}\,(V_\mathrm{p} + 0.15\,\mathrm{V})\,\frac{\mathrm{cm}^{-2}}{\mathrm{V}} \, . \tag{3.7}$$

Note that Fig. 3.6(a) as well as Eq. (3.7) relate to all optical experiments obtained for zero magnetic field.

Experiments regarding magneto-ratchets were conducted after several cool-downs; hence, the sample characteristics are comparable but differ sightly quantitatively. The corresponding transport data that are important for magnetic field measurements at

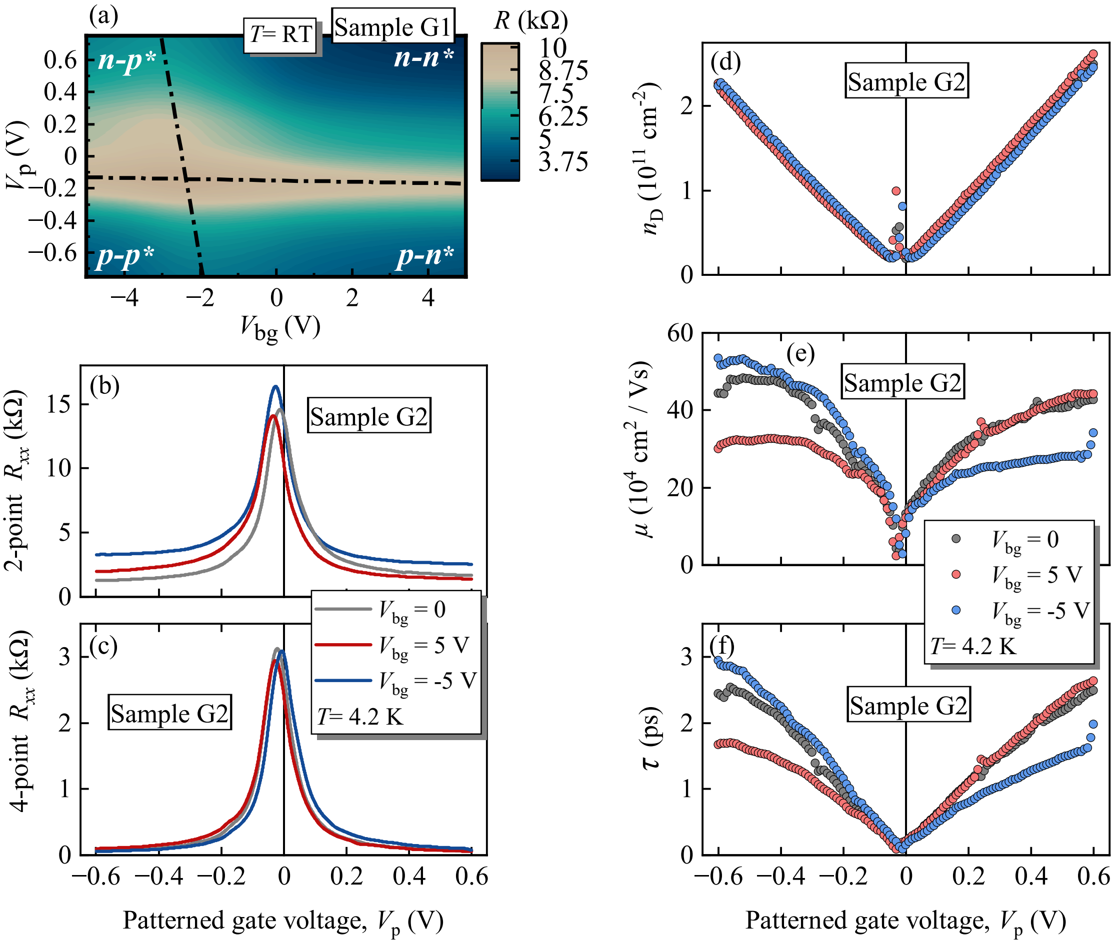

Figure 3.6 | Characteristics of the patterned-gated graphene samples G1 and G2. Panel (a) shows a two-point resistance map as a function of patterned and back gate voltage at room temperature. The dashed-dotted lines indicates the behaviour and position (crossing between them) of the charge neutrality region as a guide for the eyes. The map is divided into four parts, where n (electrons) and p (holes) indicate the charge carrier type and the asterisk ($*$) indicates the type inside graphene above the triangles. Panels (b) and (c) show the two- and four-point resistance dependent on the patterned gate for several gate voltages measured at room temperature. Panels (d)–(f) show the extracted charge carrier density, the mobility, and the momentum relaxation time, respectively. Adapted from Refs. [121,123].

$T = 4.2\,\mathrm{K}$ are given in Figs. 3.6(b)–3.6(f) for sample G2. Figures 3.6(a) and 3.6(b) show the two- and four-terminal measurements, respectively, as a function of the patterned gate voltage for various back gate voltages, measured in the same range as the optical experiments. It can be seen that while in the two-terminal setup the resistance slightly changes its magnitude with the back gate, in the four-terminal measurement the resistance does change only marginally. The same conclusion can be drawn for the position of the maximal resistance. By measuring the Hall resistance R_{xy} and the longitudinal resistance R_{xx} in four-point geometry at $B = 0.2\,\mathrm{T}$ [not shown], one can calculate important properties of the sample: the carrier density n_D according to Eq. (3.6) [Fig. 3.6(d)], the mobility $\mu = [n_\mathrm{D} e \rho_{xx}(B=0)]^{-1}$ [Fig. 3.6(e)], and the momentum relaxation time $\tau = \hbar\mu\sqrt{\pi n_\mathrm{D}/(v_0 e)}$ [Fig. 3.6(f)] with the Fermi velocity v_0. The resistivity is given by $\rho_{xx} = R_{xx} W/L$, with taking into account the width W and length L of the Hall bar channel.

3.3.2 Ferromagnetic metamaterial

The magnetic samples were fabricated by the research group of Prof. Dr. Masakazu Matsubara of Tohoku University in Japan; see also Refs. [59,125]. Figure 3.7(a) shows a cross section, revealing the layer sequence: The substrate is composed of silicon dioxide and a 5 nm thick silicon nitride (SiN) layer, each of size 4 mm × 4 mm. Above this substrate a metallic Co/Pt multilayer film sandwiched between two 2 nm thick Pt layers were attached. The multilayer consists of 0.5 nm Co and 0.9 nm Pt which repeat five times. All Co and Pt layers were fabricated by magnetron sputtering. Subsequently, the manufactured film was patterned within an area of 250 µm × 250 µm by electron beam lithography and argon ion etching. As a result, the patterned area consists of triangular holes in the material that are about 20 nm

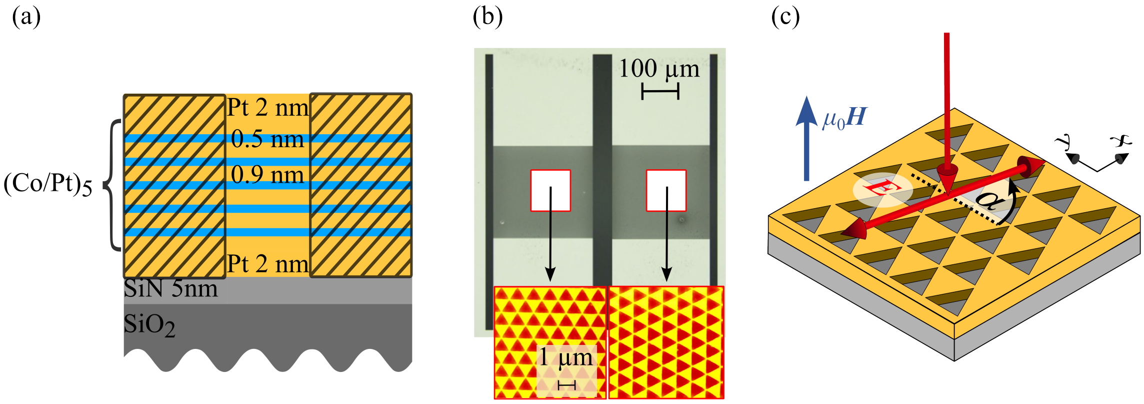

Figure 3.7 | The ferromagnetic Co/Pt metamaterial. The cross section of the sample is schematically depicted in (a), where diagonal lines indicate the slice plan, Co is marked blue and Pt yellow. Panel (b) shows an optical microscope image demonstrating the electrically separated areas, whereby the dark squares show the patterned area. The lower part shows AFM images taken from the patterned area in the region marked by red squares. Panel (c) shows the facilitated experimental configuration with the red double arrow indicating the linear polarisation vector $\boldsymbol{E}$ that can be rotated anticlockwise by the angle α with respect to the triangles' base, which means that $\alpha = 0$ corresponds to $\boldsymbol{E} \parallel \hat{\boldsymbol{y}}$. The blue vector is the magnetic field vector $\mu_0\boldsymbol{H}$. The triangles in (c) are not true to scale and depicts only the substrate and the metallic stacking (shown as one yellow layer). Figure adapted from Ref. [125].

deep, have a side length of 480 nm, and a period of 550 nm ensuring a continuous and conducting area over the entire sample; see the atomic force microscope image in Fig. 3.7(b). All measurements were conducted measuring along the height (x-axis) and the baseline (y-axis) of the triangles. For this, two ohmic contact pairs were bonded.

Note that the investigated sample in fact consists of two samples on the same substrate that are electrically separated and moreover rotated by 90°. Thus, they were measured independently, as can be seen in Fig. 3.8(a). Although some physical parameters of both sample parts may vary slightly, it is sufficient to treat it as one sample, as shown in Fig. 3.7(c). By applying an external magnetic field H, the magnetisation M can be varied, which leads to the total magnetic field $B = \mu_0 (M + H)$. Hence, due to the presence of magnetisation, the applied field is denoted by $\mu_0 H$ instead of B. Figure 3.8 shows the sample characteristics of the magnetic metamaterials. Figure 3.8(a) depicts a scheme of the sample, where grey and yellow areas correspond to insulating and conducting areas, respectively.

The electrical resistance was measured as a two-point measurement voltage drop over a 10 MΩ load resistance with a 1 V bias voltage modulated with 12 Hz from the lock-in. The resistance versus applied external magnetic field $\mu_0 H$ measured along the x-direction is given in the left sub panel Fig. 3.8(b) for 4.2 K and room temperature. It can be seen that the resistance does not depend on the magnetic

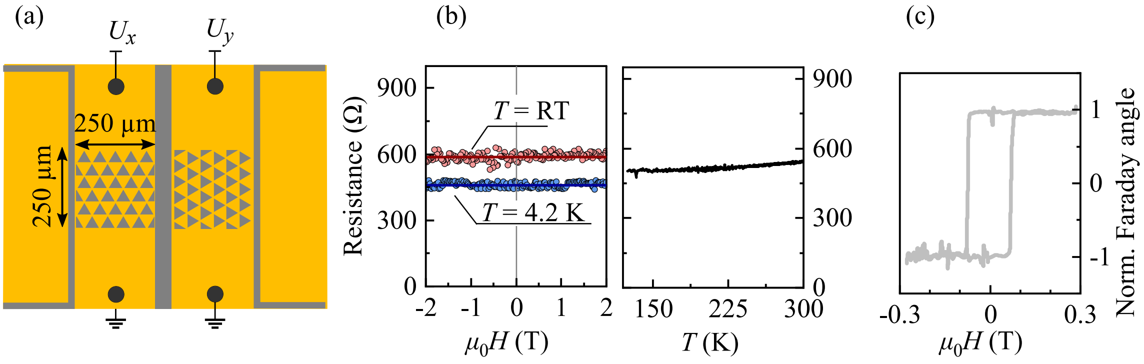

Figure 3.8 | Sample characteristics. Panel (a) shows a sketch of the sample (not to scale), including the ohmic contacts and the separated patterned areas. Grey and yellow areas are insulating and conducting, respectively. Panel (b) presents electric transport data of U_x, i.e. for the resistance measured along the triangles' height. The circles in the left sub panel show the resistance data measured versus magnetic field for 4.2 K and room temperature, and solid lines are the average values. The resistance in the right sub panel was measured at $M = H = 0$ for a wide temperature range. Panel (c) shows the hysteresis of the unstructured Co/Pt film. Figure adapted from Ref. [125].

field. Indeed, as demonstrated by the solid lines that indicate the average values, the resistance is unaltered by the magnetic field. The right sub panel in Fig. 3.8(b) shows the resistance as a function of temperature for zero magnetic field and zero magnetisation. The data were obtained during one single cool-down. The grey curve in Fig. 3.8(c) is the result of the Faraday rotation measurement and shows the normalised Faraday rotation angle conducted over the unpatterned Co/Pt film by the group of Prof. Dr. Matsubara at Tohoku University. The Faraday effect incorporates that the polarisation plane of a linearly polarised light passing trough the magnetised sample is rotated by an angle that is proportional to magnetisation. For the method and more details, see e.g. Refs. [59,134].

4 Linear ratchets in patterned-gated graphene

This chapter is devoted to the study of optoelectronic ratchet photosignals excited with linearly polarised THz radiation in graphene-based metamaterials. It starts with the presentation of the experimental results. Subsequently, the data are discussed in the framework of the theory of ratchets in a phenomenological as well as in a microscopic picture. All data shown in this chapter were measured on sample G1 and were detected at room temperature without an applied magnetic field.

4.1 Experimental results on linear ratchets

In this section, data are presented measured by a linearly polarised THz beam. The azimuth angle α indicates the anti-clockwise rotation of the radiation electric field vector $\boldsymbol{E}$ with respect to the y-direction, i.e. with respect to the triangles' base.

First, measurements were done with no patterned gate voltage (V_p) or back gate voltage (V_bg) applied. When the unbiased graphene-based sample was illuminated with THz radiation at normal incidence, a photovoltage was observed being strongly sensitive to the azimuth angle α. Figure 4.1 shows polarisation dependencies of the measured photovoltages U_x [Fig. 4.1(a)] and U_y [Fig. 4.1(b)], normalised to the radiation power to which the sample was exposed. The photosignal measured along the x-direction is maximal at $\alpha \approx 90°$, minimal at $\alpha \approx 0, 180°$, and changes its sign at approximately $\alpha = 45°, 135°$. In contrast, the signal in y-direction is maximal and minimal at $\alpha \approx 45°$ and $\alpha \approx 135°$, respectively, and changes its sign at $\alpha \approx 90°$. This behaviour can empirically be described by

$$U_x = -U_1 \cos 2\alpha + U_0 \,, \tag{4.1}$$

$$U_y = -\tilde{U}_2 \sin 2\alpha \,, \tag{4.2}$$

where $U_{x,y} \propto U_{x,y}/P_\mathrm{s} \propto j_{x,y}$. The solid lines in Fig. 4.1 are fit curves according to Eqs. (4.1) and (4.2), yielding values for the fit parameters listed in the caption of Fig. 4.1.

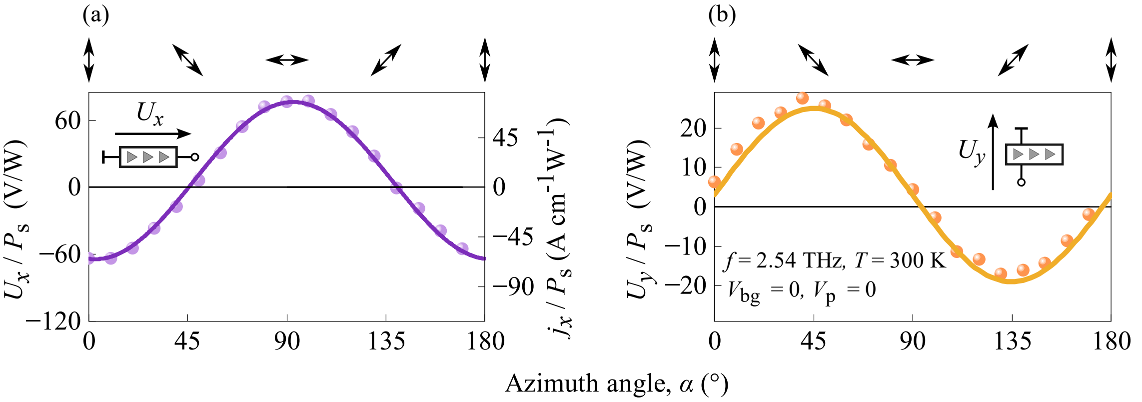

Figure 4.1 | Polarisation dependencies of the photocurrents normalised to the power the sample is exposed to, U/P_s, measured in the x-direction (a) and the y-direction (b). The data were obtained at zero gate voltages and solid lines are fits according to Eqs. (4.1) and (4.2) yielding: $U_1 = 70\,\mathrm{V/W}$, $U_0 = 6\,\mathrm{V/W}$, and $\tilde{U}_2 = -22\,\mathrm{V/W}$. The right scale in panel (a) exemplarily shows the current density normalised to the power, j_x/P_s. Insets show the direction of measurement with respect to the triangles. Arrows on top indicate the polarisation state for some values of α [121].

Next, the influence of the back gate and patterned gate voltage on the polarisation dependence is investigated. It was detected that applying gate voltages affects the polarisation dependencies significantly and leads to additional polarisation-sensitive and -insensitive contributions to the photosignals expressed by

$$U_x = -U_1 \cos 2\alpha - U_2 \sin 2\alpha + U_0\,, \tag{4.3}$$

$$U_y = -\tilde{U}_1 \cos 2\alpha - \tilde{U}_2 \sin 2\alpha + \tilde{U}_0\,, \tag{4.4}$$

where the coefficients $U_{0,1,2}$ and $\tilde{U}_{0,1,2}$ are dependent on the gate voltages applied. This is shown in Fig. 4.2 for zero patterned gate voltage and varied back gate voltages for the x-direction [Figs. 4.2(a)–4.2(c)] and the y-direction [Figs. 4.2(d)–4.2(f)]. Under these conditions, the amplitude of the polarisation dependence measured in x-direction is sensitive to the applied back gate voltage, but the polarisation dependence is not phase shifted, as U_2 is not only negligibly small but also barely depends on V_bg. In strong contrast, the signal in y-direction exhibits a complex phase shift, as the two contributions $\tilde{U}_1$ and $\tilde{U}_2$ have comparable magnitudes and are highly affected by the back gate voltage. Neglecting the polarisation-independent contribution, the phase dependence can be described by

$$U_y = \sqrt{\tilde{U}_1^2 + \tilde{U}_2^2}\ \sin 2\left(\alpha - \tilde{\phi}\right)\ ; \tag{4.5}$$

see Figs. 4.2(d)–4.2(f), with the back gate dependence of $\tilde{\phi}$ given in the inset in

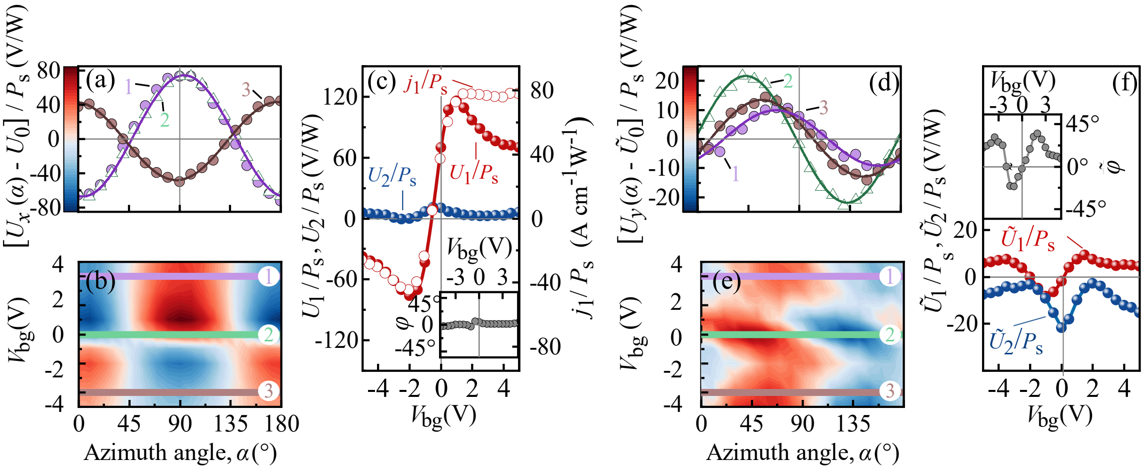

Figure 4.2 | Polarisation dependencies for zero patterned gate voltage measured in the x- [panels (a)–(c)] and y-direction [panels (d)–(f)] for a back gate voltage range from -4 V to 4 V. Note that for better visibility, the polarisation-independent contributions U_0 and $\tilde{U}_0$ have been subtracted from the α-traces. The colour scale of the contour plots [panels (b) and (e)] is given in the corresponding panel above [panels (a) and (d)], in which are shown some chosen traces, indicated by purple, green, and brown. Panels (c) and (f) depict the amplitudes according to Eqs. (4.3) and (4.4), and the insets show the phase shifts defined in Eqs. (4.5) and (4.6). The open circles in panel (c) show the contribution U_1 normalised to the resistance (right axis). Adapted from Ref. [121].

Fig. 4.1(f). The almost disappearing phase shift ϕ in the x-direction is included by

$$U_x = \sqrt{U_1^2 + U_2^2}\ \cos 2(\alpha - \phi)\ ; \tag{4.6}$$

see Figs. 4.2(a)–4.2(c), with the back gate dependence of ϕ given in the inset in Fig. 4.2(c). Indeed, a significant non-zero phase ϕ was observed only at combinations of large negative back gate voltages and simultaneous high positive patterned gate voltages, as will be shown in Fig. 4.5.

The following data presented are related to the x-direction; data of the y-direction are shown afterwards. Furthermore, the focus is on U_1 and U_0, because U_2 is considerably smaller than the other contributions. Ratchet currents are known to depend highly on the lateral asymmetry parameter. For this reason, variations in the back and patterned gate voltages, and consequently the electrostatic potential, are expected to influence the ratchet current significantly. This is demonstrated in Figs. 4.3–4.5, showing data detected by holding one gate at a fixed value and sweeping the other one. In Fig. 4.3(a) the patterned gate voltage was set to zero and the back gate voltage was varied, and vice versa in Fig. 4.3(b) $V_{bg} = 0$ and V_p was varied. It can be seen that the polarisation-dependent (U_1) and -independent (U_0) contributions have similar behaviour. So, they change their sign close at gate voltages at which the

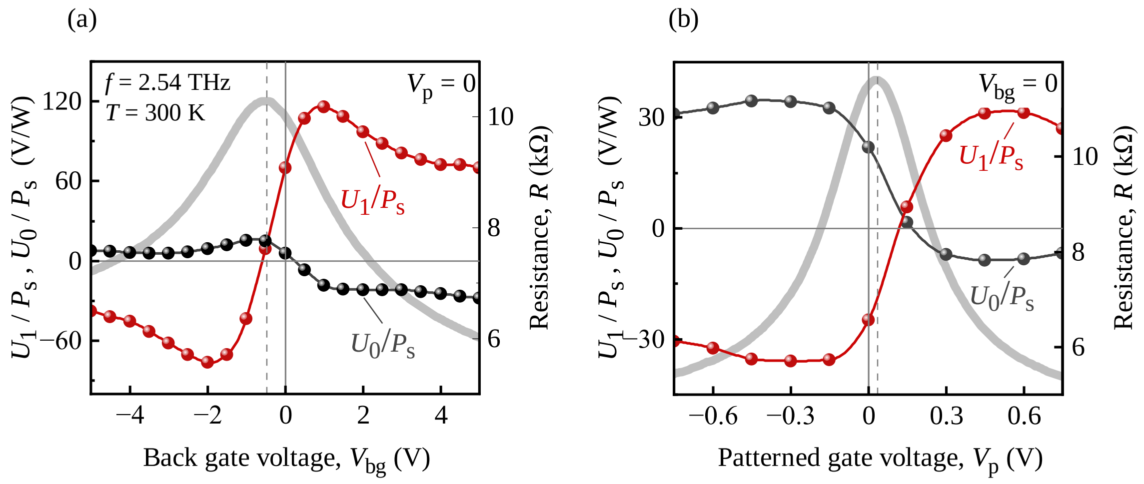

Figure 4.3 | U_1 and U_0 of U_x normalised to P_s in response to the gate voltages. The data were measured keeping one gate voltage at zero and sweeping the other. The grey curves relate to the right axes and show the two-terminal resistance measured for the same gate voltage combination as the photosignal. Adapted from Ref. [121].

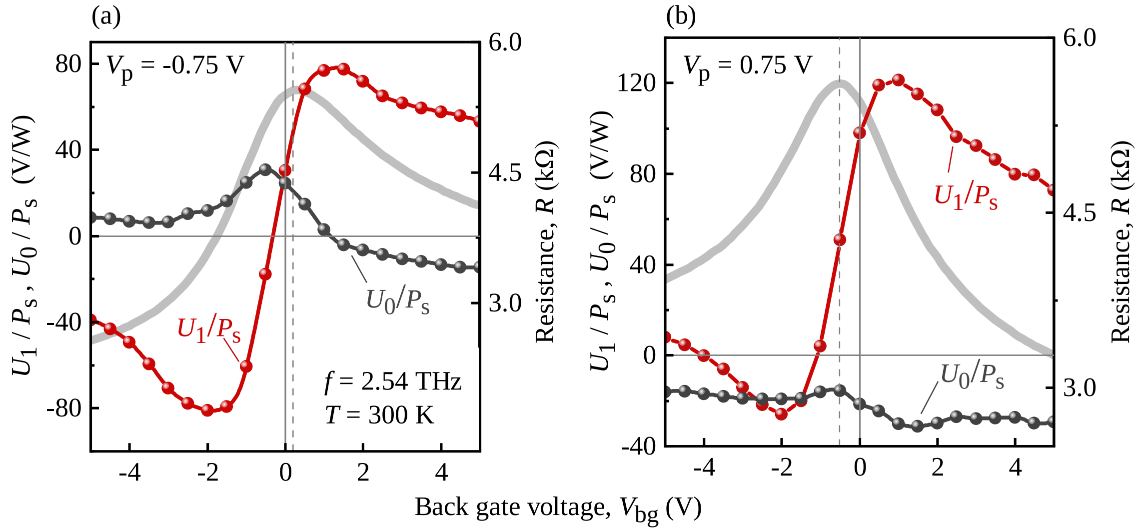

Figure 4.4 | U_1 and U_0 of U_x normalised to P_s in response to the back gate voltage. The data were measured keeping the patterned gate voltage fixed at sweeping the back gate voltage. The grey curves relate to the right axes and show the two-terminal resistance measured for the same gate voltage combination as the photosignal. Adapted from Ref. [121].

resistance is maximal, and their magnitude decreases moderately for high magnitudes of the varied gate voltage. Note that the resistance decreases for larger $|V_\text{bg}|$ and $|V_\text{p}|$, and therefore the photocurrent $j = U/R_\text{s}$ may increase or become independent of the gate voltage, as exemplarily indicated in Fig. 4.2(c) (see right axis). Moreover, U_1 and U_0 have opposite signs and U_2 is more than one order of magnitude smaller than U_1 for most gate voltages; hence U_2 is presented only in figures in which it has a non-vanishing value.

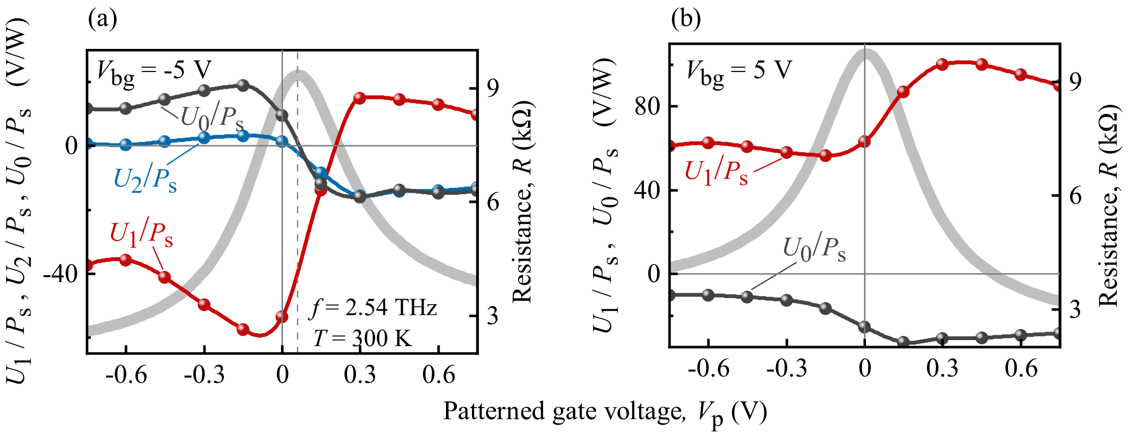

Figure 4.5 | U_1, U_2, and U_0 of U_x normalised to P_s in response to the patterned gate voltage. The data were measured keeping the back gate voltage fixed at sweeping the patterned gate voltage. The grey curves relate to the right axes and show the two-terminal resistance measured for the same gate voltage combination as the photosignal. Adapted from Ref. [121].

Figure 4.4 shows the results obtained if both gate voltages are non-zero. In Fig. 4.4(a) the data were obtained applying $V_p = -0.75\,\mathrm{V}$ and in Fig. 4.4(b) by applying $V_p = 0.75\,\mathrm{V}$. It was observed that the fixed patterned gate does not severely alter the ratchet current qualitatively. So, for both polarities of the patterned gate voltage, U_1 is significantly larger than U_0 and exhibits a sign inversion close to the maximal resistance. Qualitatively, U_1 appears to be shifted vertically when changing $V_p = -0.75\,\mathrm{V}$ to $V_p = 0.75\,\mathrm{V}$. Also, the polarisation-insensitive contribution U_0 is negative for all applied back gate voltages.

Next, the back gate voltage was set to a fixed value and the patterned gate voltage was varied. The result is presented in Fig. 4.5, showing data obtained for $V_{bg} = -5\,\mathrm{V}$ [Fig. 4.5(a)] and for $V_{bg} = 5\,\mathrm{V}$ [Fig. 4.5(b)]. It can be seen in Fig. 4.5(a) that U_1 predominates the photosignal for most values of the gate voltages, and for values larger than $V_p \approx 0.2\,\mathrm{V}$, the three contributions U_1, U_2, and U_0 exhibit a comparable magnitude. The striking difference is that for $V_{bg} = -5\,\mathrm{V}$, U_1 and U_0 undergo a sign change close to the resistance maximum, whereas for $V_{bg} = 5\,\mathrm{V}$ the signs do not change. In both cases, i.e. for negative as well as positive polarities of the back gate voltage, the main change in the photosignal amplitudes occurs for patterned gate voltages nearby the resistance maximum.

Finally, the gate dependences of the photosignal measured in the y-direction are depicted. For a set value of the patterned gate voltage of $V_p = \pm 0.75\,\mathrm{V}$ and a varied back gate voltage, the data are shown in Fig. 4.6. It can be seen that all contributions are of the same order of magnitude and feature a far more complex behaviour compared to the ratchet current U_x. So, $\tilde{U}_0$ (black traces) and $\tilde{U}_2$ (blue traces) change their sign twice in the measured range of V_{bg} for both high negative [Fig. 4.6(a)] and high positive [Fig. 4.6(b)] values of the patterned gate voltage. Conversely, Fig. 4.7 shows data obtained for $V_{\mathrm{bg}} = \pm 5\,\mathrm{V}$ and a varied patterned gate voltage. Under these conditions, the signals change their signs only once and cross at one common point, as observed for the data measured in x-direction.

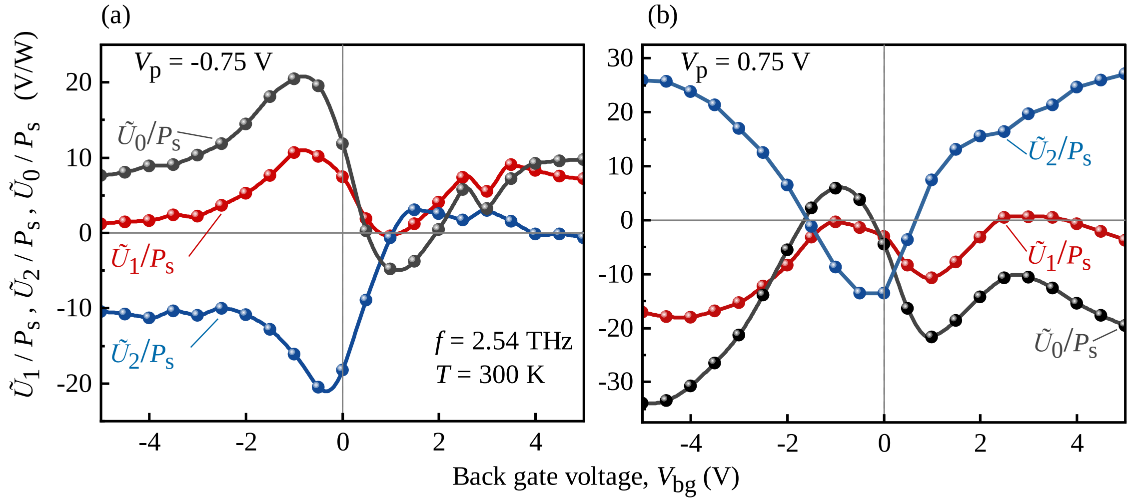

Figure 4.6 | Contributions of U_y normalised to P_{s} in response to the back gate voltage. The data were measured keeping the patterned gate voltage fixed at sweeping the back gate voltage. Adapted from Ref. [121].

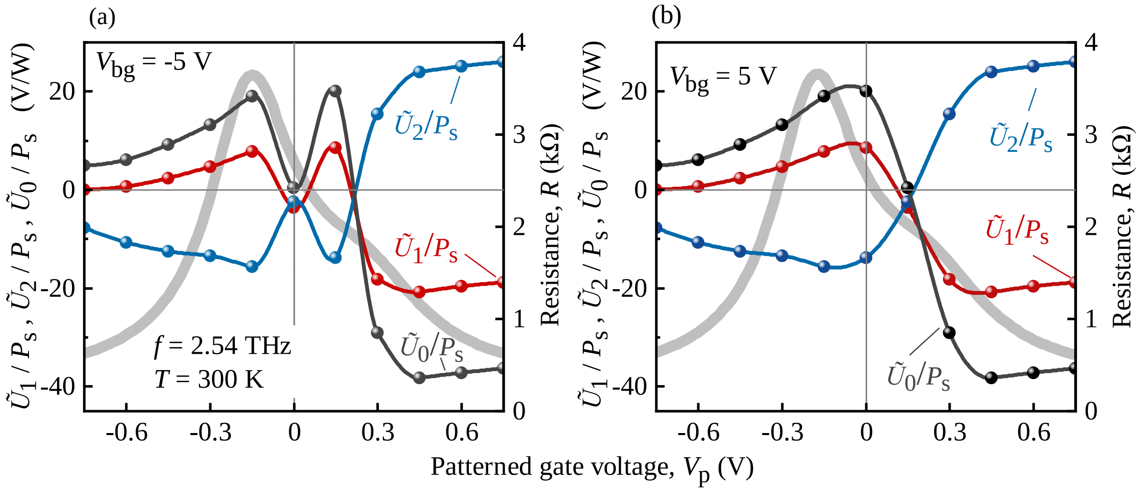

Figure 4.7 | Contributions of U_y normalised to P_{s} in response to the patterned gate. The data were measured keeping the back gate voltage fixed at sweeping the patterned gate voltage. The grey curves relate to the right axes and show the two-terminal resistance measured for the same gate voltage combination as the photosignal. Adapted from Ref. [121].

4.2 Discussion

In this section the experimental data obtained with linearly polarised light are analysed. When THz radiation is applied at normal incidence while both gate voltages are set to zero, photocurrents in the bulk of the material have been observed, as seen in Fig. 4.1. This implies that the structure has a non-centrosymmetric symmetry group, as the presence of a spatial symmetry center does not allow for ratchet currents. If a graphene flake is on a substrate or on a uniform gate, the symmetry is C_{6v}; see the review in Ref. [126]. This reduction of the symmetry occurs because the negative and positive z-directions are not equivalent any longer. For this symmetry, it is forbidden to generate dc currents at normal incidence. Consequently, the symmetry of the graphene-based device is reduced further. The polarisation dependence for $V_{\mathrm{bg}} = V_{\mathrm{p}} = 0$ in Fig. 4.1 is empirically described by Eqs. (4.1) and (4.2). This behaviour has been reported previously for ratchets in 1D metamaterials [8,18,19] and is described by C_s symmetry; see also Sec. 2.3. Indeed, the geometry of the patterned gate has C_s symmetry. This can be seen, if one considers the triangle-shaped antidots grouped in a square lattice. The conducting patterned gate underneath the graphene flake leads to an electrostatic interaction that gives rise to an asymmetric built-in potential. As a consequence, photosignals can be observed even for zero gate voltages.

A system with C_s symmetry supports only one non-trivial symmetry operation: reflection in the (zx)-plane, which is perpendicular to both the graphene sheet and the bases of the triangles. Hence, the x-direction is composed of a polarisation-independent and -dependent part that is symmetric, and the y-direction consists only of an antisymmetric part. For 2D metamaterials the photocurrent densities are given by

$$j_x = \Xi_x \left[\chi_0 + \chi_1 \left(|e_x|^2 - |e_y|^2\right)\right] , \tag{4.7}$$

$$j_y = \Xi_x \chi_2 \left(e_x e_y^* + e_x^* e_y\right) , \tag{4.8}$$

as suggested by Dr. Leonid Golub in [121]. Here, Ξ_x is the x-component of the lateral asymmetry vector [121]

$$\Xi_{\mathrm{2D}} = \left\langle \boldsymbol{E}_0^2(\boldsymbol{r}) \nabla V(\boldsymbol{r}) \right\rangle , \tag{4.9}$$

where the average is performed over the 2D period. The transition of ratchets in 1D metamaterials to the 2D case was proposed in Ref. [121]. Therein, the assumption is to treat the potential as well as the electric field of the radiation as small perturbations, which allows one to trace back the microscopic photocurrent generation of a 2D modulation to a 1D modulation. This means that in contrast to previous works, e.g. in Refs. [2,18,19], the lateral asymmetry parameter is a vector instead of a scalar quantity, because the system is modulated in two dimensions. The interpretation of χ_0, χ_1, and χ_2 is the same as in the 1D modulation presented in Sec. 2.3, i.e. they describe the microscopic mechanisms and depend only on the characteristics of the 2DES. Equations (4.7) and (4.8) are in accordance with Fig. 4.1 measured in the ungated sample and with the empirically obtained Eqs. (4.1) and (4.2), which can be seen especially bearing in mind that $P_1 = (|e_x|^2 - |e_y|^2) = -\cos 2\alpha$ and $P_2 = \left(e_x e_y^* + e_x^* e_y\right) = -\sin 2\alpha$. It should be mentioned that the measured signals are not due to edge currents, because U_x is maximal for azimuth angles for which the edge current is zero [126,127]; see Figs. 4.1(a), 4.2(a), and 4.2(b).

As the experiments were performed at room temperature at which the condition $\omega\tau \gg 1$ holds, it can be shown that in the high-frequency limit the microscopic parameters take the form [121]

$$\chi_1 = \chi_2 = -\frac{q^3 v_0^2 \tau}{2\pi\hbar^2\omega^2 E_\mathrm{F}}\,, \tag{4.10}$$

and [121]

$$\chi_0 = \chi_1 \left(1 - \frac{16\pi^2 k_\mathrm{B} T \tau_\mathrm{T}}{9\tau E_\mathrm{F}}\right)\,. \tag{4.11}$$

Here, q is the carrier charge, v_0 the Fermi velocity, τ the transport relaxation time, E_F the Fermi energy, T the lattice temperature, and τ_T the electron temperature relaxation time corresponding to electron-phonon interaction [8,121]. While $\chi_{1,2}$ are gained in the model of dynamic carrier-density redistribution (DCDR) accounting for the polarisation-dependent ratchets, χ_0 describes the polarisation-independent ratchet current; see also Eqs (4.7) and (4.8). The first term of χ_0 in Eq. (4.11) is also evoked by DCDR. However, the second term is caused by the Seebeck ratchet generated by heating of the electron gas and simultaneous spatial charge redistribution [8,121]. The expressions for $\chi_{1,2}$ and χ_0 acquired from the theory allow for the following qualitatively conclusions [121]: (i) all parameters are proportional to q^3, and therefore changing from the electron to the hole conduction regime inverse the sign of the parameters; (ii) $\chi_{1,2}$ depend on the charge carrier density n due to the ratio τ/E_F, which is independent of n for long-range Coulomb scattering and for short-range scattering $\chi_{1,2} \propto 1/n$; (iii) χ_0 and $\chi_{1,2}$ have opposite signs if the Seebeck ratchet predominates; and (iv) all parameters scale as τ/ω^2, and thus higher mobilities and longer wavelengths should result in higher photocurrents. In particular, the conclusion (iii) has been observed in the experiments, as can be seen in Fig. 4.1(a), demonstrating that the polarisation-dependent and -independent parts have opposite signs. This behaviour has also been observed for most gate voltage sequences, as seen in Figs. 4.3–4.5. From these finding follows that the Seebeck contribution is the most crucial mechanism for the generation of the polarisation-independent ratchet current.

Equations (4.10) and (4.11) may lead to the fallacy that the formation of the photocurrents would simply be governed by these expressions. However, the concrete 2D-modulated system is more complex as a 1D-modulated system, because the patterned gate and the uniform back gate act almost independently. So, two regions are formed due to the screening of the back gate by the patterned gate: the area in graphene inside the triangles, governed by the back gate voltage, and the area between the triangle-shaped antidots, governed by the patterned gate voltage [60,121]. The total photocurrent is the sum of the contributions of both areas, which may not only have a different lateral asymmetry vector but can also generate currents that are different in sign. Thus, the ratchet currents are governed by the two independent lateral asymmetry parameters Ξ_x and Ξ_x^*, with different charge densities inside (n^*, p^*) or outside (n, p) the triangles.

Now, the data obtained in the gated graphene metamaterial are discussed. Gating the sample results in additional parts to the photocurrent, which can be seen very pronounced in Figs. 4.2(d)–4.2(f), 4.5, 4.6, and 4.7. These additional contributions are empirically described by Eqs. (4.3) and (4.4). Phenomenologically, this means that the symmetry is reduced from C_s to C_1, which has only the identity symmetry operation. This argument is supported by the sample design shown in the microscopic image of sample G1 in Fig. 3.5(c), revealing that the graphene flake includes only a part of the lowest triangle row. As a consequence of this symmetry reduction, also the y-component of the lateral asymmetry vector $\boldsymbol{\Xi}_{2\mathrm{D}}$ enters the equation for the photocurrent, resulting in the corrections [121]

$$\delta j_x = \Xi_y \chi_2 \left(e_x e_y^* + e_x^* e_y \right) , \tag{4.12}$$

$$\delta j_y = \Xi_y \left[\chi_0 - \chi_1 \left(|e_x|^2 - |e_y|^2 \right) \right] . \tag{4.13}$$

The parameters $\chi_{0,1,2}$ are the same as in Eqs. (4.7) and (4.8), because they are set by the properties of graphene and do not depend on the lateral potential. Bearing again the Stokes parameters in mind, the total photocurrent is now given by [121]

$$j_x = \Xi_x \left(\chi_0 - \chi_1 \cos 2\alpha \right) - \Xi_y \chi_2 \sin 2\alpha \, , \tag{4.14}$$

$$j_y = -\Xi_x \chi_2 \sin 2\alpha + \Xi_y \left(\chi_0 + \chi_1 \cos \alpha \right) . \tag{4.15}$$

These modifications fully describe all experimental results. In particular, the connection of theory and experimental data yields that $U_1 \propto \Xi_x\chi_1$, $U_2 \propto \Xi_y\chi_2$, $U_0 \propto \Xi_x\chi_0$, $\tilde{U}_1 \propto \Xi_y\chi_1$, $\tilde{U}_2 \propto \Xi_x\chi_2$, and $\tilde{U}_0 \propto \Xi_y\chi_0$. This symmetry reduction largely impacts the y-component of the photocurrent, as can be seen in Fig. 4.2(d)–4.2(f) showing that the contributions $\tilde{U}_1$ and $\tilde{U}_2$ dictate the photocurrent to a similar extend. In contrast, the contribution U_1 in x-direction is large compared to U_2 for most gate voltage sequences. Furthermore, the polarisation-insensitive part $\tilde{U}_0$ would not be allowed for C_s symmetry and is a clear signature for C_1 symmetry.

The exact influence of the gate voltages on the lateral asymmetry vectors remains unclear and is a future task. For example, in Ref. [8] it has been demonstrated that radiation near fields can depend on the applied gate voltage.

Nevertheless, the effect of the gate voltages on the electrostatic potential in the sample G1 used for the experiments was simulated by the finite-element method using FEniCS [131] by Wun-Hao Kang from the research group of Prof. Dr. Ming-Hao Liu of the National Cheng Kung University of Taiwan; see also Ref. [121]. For the computation, an array of triangles of 3×3 was considered, as shown in Fig. 4.8(a). The additional assumptions were (i) that the volume of the holes in the patterned gate is vacuum, since hBN and SiO_2 barely modify the potential in such a thin metal sheet; (ii) that the dielectric constants are $\epsilon(\text{hBN}) = 3$ and $\epsilon(\text{SiO}_2) = 3.9$; and (iii) that the built-in potential is not included. By calculating the dielectric displacement field $\boldsymbol{D}$, the potential was found by the relation $V(\boldsymbol{r}) = -\,\text{sgn}[n(\boldsymbol{r})]\hbar v_0\sqrt{\pi|n(\boldsymbol{r})|}$, and the spatially dependent capacitances $C_{\text{bg}}(\boldsymbol{r})$ and $C_{\text{p}}(\boldsymbol{r})$ of both gates were calculated. The results are shown in Fig. 4.8(b) and 4.8(c), showing the spatially dependent capacitance for one period of the triangles for the back and patterned gate, respectively. Figures 4.8(d)–4.8(g) present the partial-differentiated on-site potential $\nabla_x V(r)$ with respect to x in real space for different combinations of the gate voltages. It can be seen that while it is symmetric with respect to the y-coordinate, it is highly asymmetric regarding the x-coordinate, enabling a non-zero ratchet current along the x-direction. In particular, reversing one of the gate voltage polarity inverts the sign of $\nabla_x V(r)$, and consequently the sign of the lateral asymmetry parameter. In strong contrast, $\nabla_y V(r)$ is asymmetric in y-direction, as shown in Figs. 4.8(h) and 4.8(i).

The results of the simulations may help in judging the signs of the photocurrents. If one supposes that the near-field does not change sign with the gate voltages and using the numerical results, it can be seen that $q^3\Xi_x$ and $q^{*3}\Xi_x^*$ do not change sign, as inverting one gate polarity inverts the sign of q^3 or q^{*3} and simultaneously the corresponding lateral asymmetry parameter. Hence, if $q^3\Xi_x$ and $q^{*3}\Xi_x^*$ have the same sign, the photocurrent keeps its sign, as shown in Fig. 4.5(b).

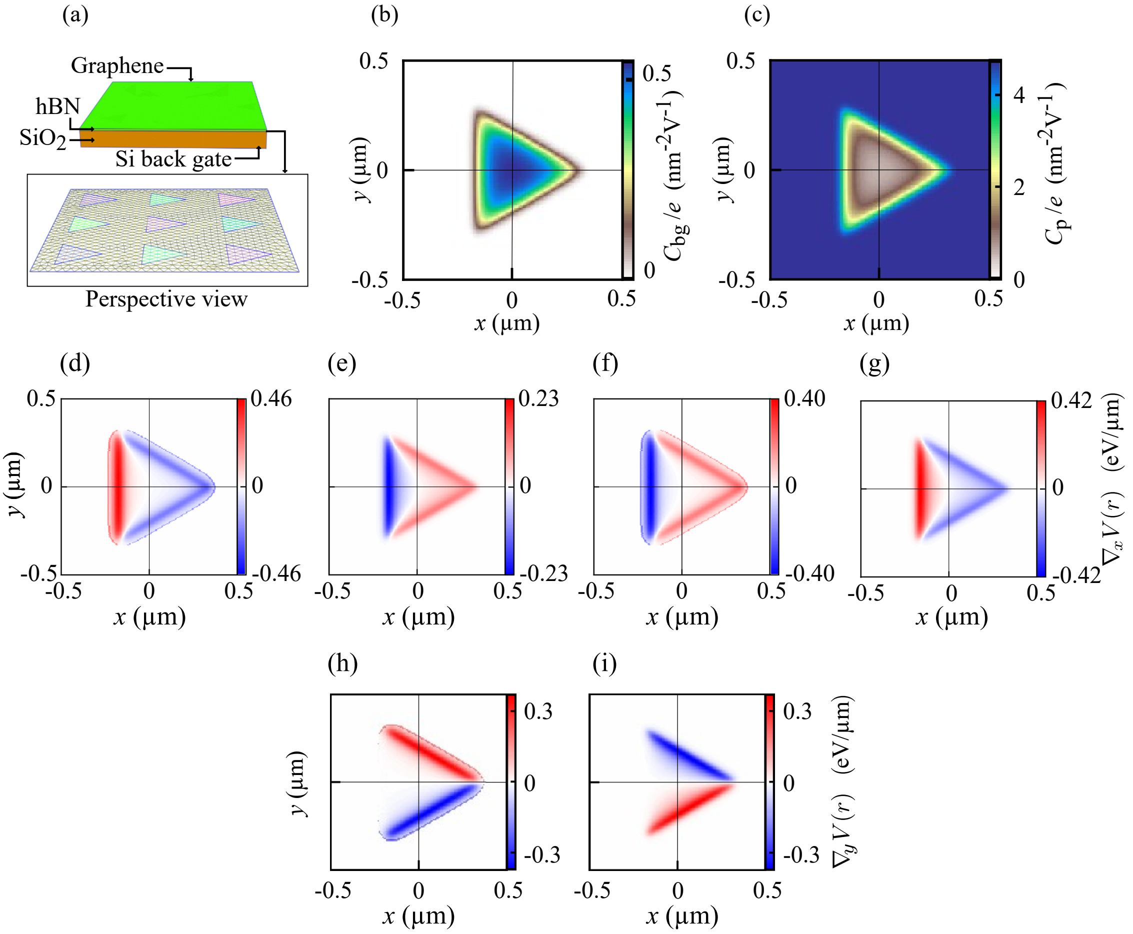

Figure 4.8 | Panel (a) sketches the geometry of the electrostatic simulation. The Capacitance simulation is spatially dependent due to the global back gate (b) or the patterned back gate (c), shown for one triangle period. Panels (d) to (i) show the partial derivative of the potential (scale on right axes) with respect to x [panels (d) to (g)] and to y [panels (h) and (i)] as a function of x and y for (V_{bg}, V_{p}) taken in volts: (-2, 0)(d), (1.5, 0) (e), (0, -0.15) (f),(0, 0.5) (g), (1.5, 0) (h), and (0, 0.5) (i). Adapted from Ref. [121].

5 Circular ratchets in patterned-gated graphene

This chapter presents data of ratchet signals in the graphene-based metamaterial obtained with circularly polarised THz radiation. First, the experimental data are depicted, and afterwards the data are discussed in the framework of the ratchet effect. All data shown in this chapter were measured on sample G1 at room temperature without an applied magnetic field.

5.1 Experimental results on circular ratchets

In the following, data are depicted obtained with circularly polarised light. First, polarisation dependencies were recorded by rotating a quarter-wave plate, altering both the helicity and linear polarisation degree of the incident linearly polarised THz radiation. The detected photovoltages in x- and y-direction are shown in Fig. 5.1 for zero patterned gate voltage and several back gate voltages. The data can be well

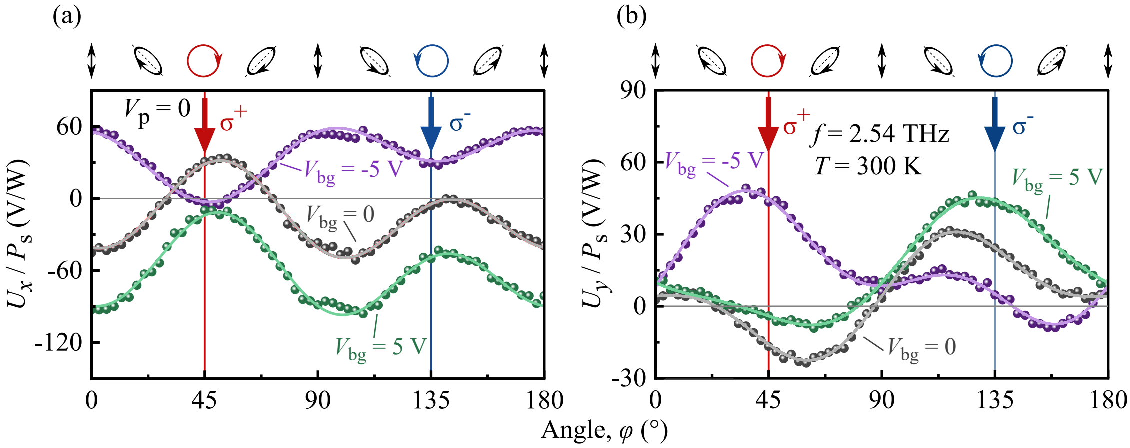

Figure 5.1 | Photovoltage normalised to power for the x- (a) and y-direction (b) as a function of the angle φ for zero patterned gate voltage and different back gate voltages. On top are given the polarisation states for some angles of φ. The arrows for $\varphi = 45°$ (red) and $\varphi = 135°$ (blue) indicate the circularly polarised regime. The solid lines are fits according to Eqs. (5.1) and (5.2) and the obtained parameters are listed in Table 5.1. Adapted from Ref. [122].

Table 5.1 | Parameters in units (V/W) for V_{bg} =$\{-5,\ 0,\ 5\}$ V obtained from the fit functions shown in Fig. 5.1 according to Eqs. (5.1) and (5.2).

	U_x				U_y			
V_{bg} (V)	U^{circ}	U_0	U_1	U_2	$\tilde{U}^{\mathrm{circ}}$	$\tilde{U}_0$	$\tilde{U}_1$	$\tilde{U}_2$
−5	17	14	−41	5	−19	25	16	21
0	−17	12	53	−28	20	4	0	21
5	−25	−31	59	−17	−1	−22	−14	−3

fitted by the empirical formulas

$$U_x = U^{\mathrm{circ}} \sin 2\varphi + U_0 - U_1 \frac{1+\cos 4\varphi}{2} - U_2 \frac{\sin 4\varphi}{2}\,, \tag{5.1}$$

$$U_y = \tilde{U}^{\mathrm{circ}} \sin 2\varphi + \tilde{U}_0 - \tilde{U}_1 \frac{1+\cos 4\varphi}{2} - \tilde{U}_2 \frac{\sin 4\varphi}{2}\,, \tag{5.2}$$

where the Stokes parameters occur; see Chap. 3. For illustration, the polarisation states are shown on top of Fig. 5.1(a) and 5.1(b) for chosen values of the angle φ. The fit parameters are listed in Table 5.1. As the parameters that describe linearly polarisation-dependent ($U_1, U_2, \tilde{U}_1, \tilde{U}_2$) and -independent ($U_0, \tilde{U}_0$) contributions have already been addressed in the previous chapter, the parameters U^{circ} and $\tilde{U}^{\mathrm{circ}}$ are of particular interest. In fact, a change in the photosignal amplitude has been observed when changing from right- to left-handed circularly polarised light, marked by red and blue arrows, respectively. This demonstrates that there is a noticeable contribution to the ratchet current that is sensitive to the helicity of the radiation. For purely circularly polarised light, as is the case for $\varphi = 45°, 135°$, the Stokes parameters P_1, P_2 describing the linear polarisation states are zero. Hence, Eqs. (5.1) and (5.2) take the simplified form

$$U_x^{\mathrm{circ}} = \pm U^{\mathrm{circ}} + U_0\,, \tag{5.3}$$

$$U_y^{\mathrm{circ}} = \pm \tilde{U}^{\mathrm{circ}} + \tilde{U}_0\,, \tag{5.4}$$

where “+” and “−” refers to right- (σ^+) and left-handed (σ^-) circularly polarised light, respectively. Consequently, the circular contributions to the photosignal can be extracted by taking the half-differences

$$U^{\mathrm{circ}} = \frac{1}{2}\left(U_x^{\sigma^+} - U_x^{\sigma^-}\right)\,, \tag{5.5}$$

$$\tilde{U}^{\mathrm{circ}} = \frac{1}{2}\left(U_y^{\sigma^+} - U_y^{\sigma^-}\right)\,. \tag{5.6}$$

It can be seen in Fig. 5.1 as well as in the insets in Figs. 5.2 and 5.3 that the σ^+- and σ^--generated photosignals depend exceedingly on the applied gate voltages; in particular, they differ in amplitude and for some gate voltages they have also opposite

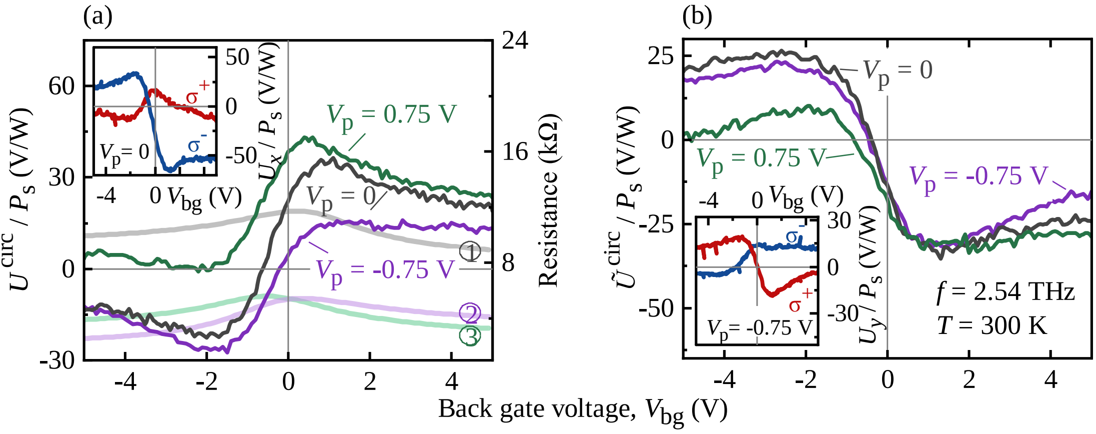

Figure 5.2 | Normalised photovoltages $U^{\mathrm{circ}}/P_{\mathrm{s}}$ (a) and $\tilde{U}^{\mathrm{circ}}/P_{\mathrm{s}}$ (b) dependent on the back gate voltage for different patterned gate voltages. The data were obtained measuring the photosignal in response to right- and left-handed circularly polarised light and using Eqs. (5.5) and (5.6). Solid lines with reduced opacity refer to the resistance measured for the same patterned gate voltages as applied for the photovoltage measurements: ① 0; ② -0.75 V; and ③ 0.75 V. The insets in panel (a) and (b) exemplarily depict signals obtained for both helicities. Adapted from Ref. [122].

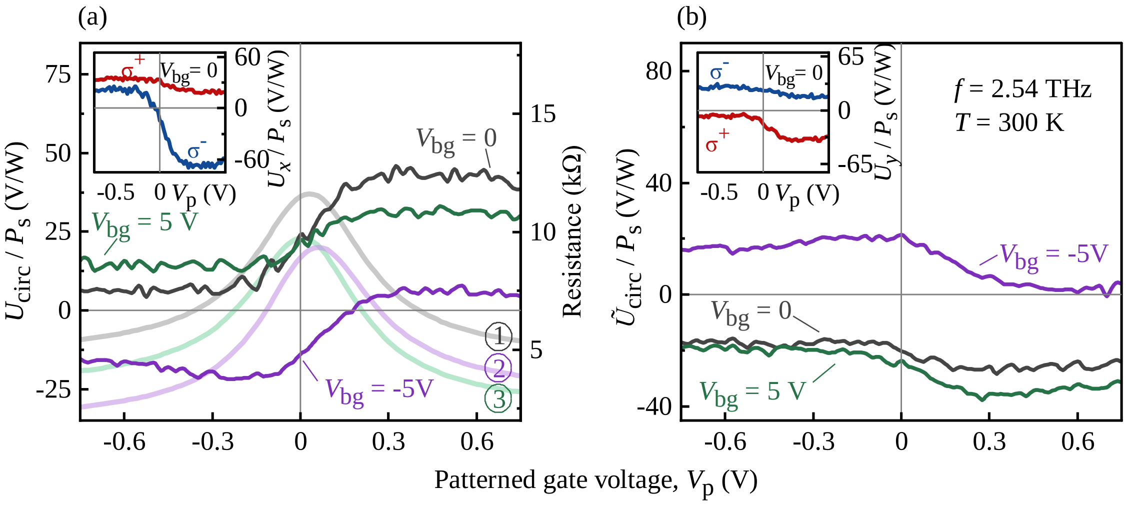

Figure 5.3 | Normalised photovoltages $U^{\mathrm{circ}}/P_{\mathrm{s}}$ (a) and $\tilde{U}^{\mathrm{circ}}/P_{\mathrm{s}}$ (b) dependent on the patterned gate voltage for different back gate voltages. The data were obtained measuring the photosignal in response to right- and left-handed circularly polarised light and using Eqs. (5.5) and (5.6). Solid lines with reduced opacity refer to the resistance measured for the same back gate voltages as applied for the photovoltage measurements: ① 0; ② -5 V; and ③ 5 V. The insets exemplarily depict the measured helicity dependence as a function of the patterned gate for zero back gate voltage. Adapted from Ref. [122].

signs. The extracted circular ratchet signals are shown in Figs. 5.2 and 5.3. The data were measured keeping one gate voltage at a fixed value and sweeping the other one. It has been observed that both U_x [Figs. 5.2(a) and 5.3(a)] and U_y [Figs. 5.2(b) and 5.3(b)] are altered only slightly for large $|V_{\mathrm{bg}}|$ and $|V_{\mathrm{p}}|$ and change their amplitude substantially close to the resistance maximum. On one hand, at this point, the photosignal can change its sign, as seen, e.g. in Figs. 5.2(a) for $V_{\mathrm{p}} = -0.75\,\mathrm{V}$ or in Fig. 5.2(b). On the other hand, the photosignal can preserve its sign, as seen, e.g. in Fig. 5.3. Moreover, the circular ratchet currents along the x-direction have opposite signs to those measured along the y-direction for all gate voltage sequences used in the experiments. This means that varying the gate voltage, the maxima and minima of U^{circ} were detected at different polarities of the gate voltage compared to $\tilde{U}^{\mathrm{circ}}$.

5.2 Discussion

In this section, the experimental data of the circular ratchet data are analysed, starting with the polarisation dependencies shown in Fig. 5.1. These data are well described by the empirical Eqs. (5.1) and (5.2). The linear polarisation-dependent contributions $U_{1,2}$ and $\tilde{U}_{1,2}$, and the -insensitive contributions U_0 and $\tilde{U}_0$ have already been discussed in the previous chapter. However, the circular polarisation-dependent components U^{circ} of U_x and $\tilde{U}^{\mathrm{circ}}$ of U_y are new. They can only be observed in case of non-zero ellipticity of the radiation and are most pronounced for purely circularly polarised radiation. Specifically, the sign of the contribution depends on the helicity, as given by Eqs. (5.5) and (5.6). As already elaborated in the preceding analysis of the linear ratchets, the symmetry operation for the graphene sample G1 is described by C_1 symmetry. In the phenomenological description as given in Ref. [122], Eqs. (4.14) and (4.15) can be extended such that they include also the circular terms leading to [122]

$$j_x = -\Xi_y \gamma P_{\mathrm{circ}} + \Xi_x \left(\chi_0 + \chi_1 P_1\right) + \Xi_y \chi_2 P_2 \,, \tag{5.7}$$

$$j_y = \Xi_x \gamma P_{\mathrm{circ}} + \Xi_y \left(\chi_0 - \chi_1 P_1\right) + \Xi_x \chi_2 P_2 \,. \tag{5.8}$$

Here, the additional parameter γ emerges and is connected to the Stokes parameter $P_{\mathrm{circ}} = -i\left(\boldsymbol{e} \times \boldsymbol{e}^*\right)_z$. Note that in this section the radiation is assumed to propagate in the $-z$-direction. From the phenomenological equations can be seen that the sign of the circular ratchet currents depends on the sign of the helicity, because the circular current is proportional to P_{circ}, whose sign reverses when changing from right- to left-handed circularly polarisation. This can be seen in the insets in Figs. 5.2 and 5.3.

For pure circular polarisation, the photosignal is only composed of the circular and the polarisation-independent ratchets. Subsequently, the photocurrent densities of the circular ratchet effect read [122]

$$j_x^{\mathrm{circ}} = -\Xi_y \gamma P_{\mathrm{circ}}\,, \tag{5.9}$$

$$j_y^{\mathrm{circ}} = \Xi_x \gamma P_{\mathrm{circ}}\,. \tag{5.10}$$

This means that the circular ratchet current in one spatial coordinate direction is generated by a finite lateral asymmetry parameter evaluated along the other direction. If one assumes that Ξ_x and Ξ_y have the same sign, Eqs. (5.9) and (5.10) predict that $U^{\mathrm{circ}} \propto j_x^{\mathrm{circ}}$ and $\tilde{U}^{\mathrm{circ}} \propto j_y^{\mathrm{circ}}$ have opposite signs. This has indeed been observed, as can be seen in the experimental data in Figs. 5.1–5.3. For better visibility, some data are re-plotted in Fig. 5.4, clearly demonstrating the different sign of the photosignal in x- and y-direction.

Now, the discussion turns to the microscopic theory, which has been developed in Ref. [122]. Therein, it was found that the parameter γ takes the form

$$\gamma = \frac{q^3 v_0^4 \tau^3 \omega^2 \mathcal{F}(\Omega)}{2s^2 \pi \hbar E_{\mathrm{F}} \left[1 + (\omega\tau)^2\right] \left[\omega^2 + \left(\omega^2 - \omega_{\mathrm{pl}}^2\right)^2 \tau^2\right]}\,, \tag{5.11}$$

where τ denotes the transport relaxation time, and $\omega_{\mathrm{pl}} = s\sqrt{q_x^2 + q_y^2}$ the plasmon frequency. Here, s is the plasmon velocity, and for the 2D square lattice in this work $q_x = q_y = 2\pi/d$ is the reciprocal lattice period of the metamaterial [$\mathcal{F}(\Omega)$ takes into account scattering and is discussed later on]. Equation (5.11) demonstrates that γ, and consequently U^{circ} and $\tilde{U}^{\mathrm{circ}}$, scales with the third power of the charge carrier density q. As the two lateral asymmetry vectors (Ξ_{2D} controlled by V_{p} and Ξ_{2D}^*

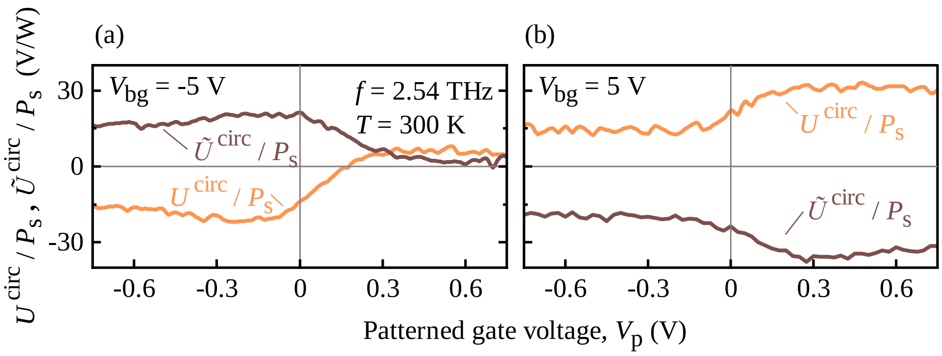

Figure 5.4 | Circular ratchet signals in x-direction (U^{circ}, orange) and y−direction ($\tilde{U}^{\mathrm{circ}}$, brown) versus patterned gate voltage for $V_{\mathrm{bg}} = -5\,\mathrm{V}$ (a) and $V_{\mathrm{bg}} = 5\,\mathrm{V}$ (b). Adapted from Ref. [122].

controlled by V_{bg}) are supposed to change their signs when inverting the corresponding gate voltage polarity (see discussion in Sec. 4.2), the signs of $q^3\Xi_{x,y}$ and/or $q^3\Xi^*_{x,y}$ do not change. In consequence, the signs of U^{circ} and $\tilde{U}^{\text{circ}}$ are expected to remain; however, the circular currents can undergo a change in sign upon sweeping one gate voltage, as detected for certain back gate and patterned gate voltages. This finding can be attributed to a different sign of $q^3\Xi_x$ and $q^3\Xi^*_x$, or $q^3\Xi_y$ and $q^3\Xi^*_y$

The sign of γ itself depends on the concrete scattering mechanism, which is addressed in the following theoretical description after Refs. [2,122]. The dimensionless factor $\mathcal{F}(\Omega)$ in Eq. (5.11) with $\Omega = \omega\tau$ takes into account the frequency-dependent scattering mechanism in graphene. For instance, for short-range ("s.r.") and Coulomb ("C") scattering potentials, this factor is expressed by [122]

$$\mathcal{F}_{\text{s.r.}} = -\frac{2\Omega^5 + \Omega^3 + 8\Omega}{\left(\Omega^2 + 4\right)^2}\,, \quad \mathcal{F}_{\text{C}}(\Omega) = \frac{1}{\Omega}\,. \tag{5.12}$$

The limit $\mathcal{F}_{\text{C}}(\Omega) \to \infty$ if $\Omega \to 0$ does not strictly hold, as $\mathcal{F}_{\text{C}}(\Omega)$ is screened by plasmon or energy relaxation mechanisms preserving a finite value. For this reason, in the calculations performed at $\omega_{\text{pl}} = 0$ it is assumed that $\mathcal{F}_{\text{C}}(\Omega) = \Omega/\left[\Omega^2 + (\tau/\tau_{\text{E}})^2\right]$, with the transport relaxation time much smaller than the energy relaxation time τ_{E}, and the ratio $(\tau/\tau_{\text{E}})^2 = 0.2$ [122]. Note that τ_{E} significantly modifies the behaviour of j^{circ} only at low frequencies. The results of the calculated photocurrent densities for the short-range and Colomb scattering are shown in Fig. 5.5 for the y-direction, $j_y^{\text{circ}} = \Xi_x\gamma$, normalised to $j_0 = \Xi_x q^3 v_0^4 \tau^3/(4s^2\pi\hbar E_{\text{F}})$. It can be seen that the ratchet current is highly sensitive to $\Omega = \omega_{\text{pl}}\tau$ due to different regimes, which in the limit $\omega_{\text{pl}}\tau \ll 1$ is electronic and for $\omega_{\text{pl}}\tau \gg 1$ plasmonic . The electronic regime is shown by the black curves in Fig. 5.5, revealing that the circular ratchet current is maximal

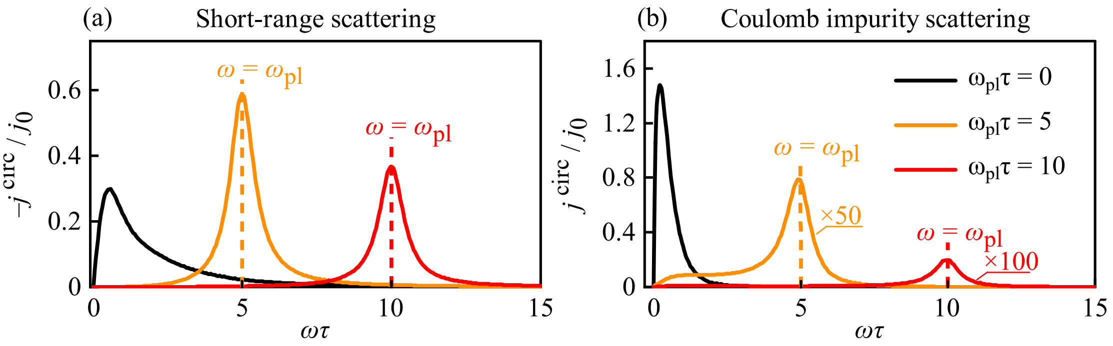

Figure 5.5 | Normalised circular photocurrent densities in y-direction for short-range (a) and Coulomb scattering (b) as a function of $\omega\tau$ for $\omega_{\text{pl}} = 0$ (black curves) and different values of $\omega_{\text{pl}}\tau$. For the sake of comparability, the sign of the photocurrents in panel (a) has been inverted. Adapted from Ref. [122].

at $\omega\tau \lesssim 1$. This condition is indicative for circular photocurrents, for example generated by the photogalvanic effect or the dynamic Hall effect [47,126]. In order to generate photocurrents that are responsive to the radiation helicity, it is fundamental that the carriers undergo a retardation with respect to the driving field. This retardation is caused by scattering and for both introduced types of scattering the circular photosignal becomes maximal at $\omega\tau \lesssim 1$, especially for Coulomb scattering if $\omega\tau_{\mathrm{E}} \approx 1$. Furthermore, the ratchet current substantially reduces for higher frequencies, and for $\omega\tau \gg 1$ the asymptote scales as ω^{-3} for short-range and as ω^{-5} for Coulomb impurity scattering. Higher plasmon frequencies give rise to the plasmonic ratchet effect exhibiting a significant change in the frequency dependence of the circular ratchet photocurrent, demonstrated by the orange and red curves in Fig. 5.5. On one hand, the two scattering mechanisms behave similarly: the circular ratchet current is maximal close to the plasmon frequency, and the width of the plasmon resonance depends on $\omega_{\mathrm{pl}}\tau$. On the other hand, there are differences: for short-range scattering, the maximal ratchet current does only slightly depend on ω_{pl}, whereas for Coulomb scattering larger plasmon frequencies lead to a suppression of the resonant current amplitude. This is seen in Fig. 5.5 in which the amplitudes from left to right become significantly smaller.

For future studies this theory [122], which describes the scattering mechanisms in the parameter γ, may be helpful to identify the scattering processes in the sample, in particular as the short-range and Colomb impurity scattering lead to photocurrents with different signs.

Finally, the shape of the photosignals are commented. In Figs. 5.2 and 5.3 can be seen that the photovoltage amplitude changes its sign preliminary close to the resistance maximum, and for larger $|V_{\mathrm{bg}}|$ and $|V_{\mathrm{p}}|$ the signal reduces or remains constant. At this point, it should be noted that the shape of the photo current density $j = U/(R_{\mathrm{w}})$ differs from the photovoltage to some extend. As with higher gate voltage magnitudes the resistance decreases, the behaviour of the photocurrent versus gate is modified: for higher $|V_{\mathrm{bg}}|$ and $|V_{\mathrm{p}}|$ the photocurrent density is mostly constant or increases. This can be seen in Fig. 5.6, which shows j^{circ} for various gate voltage combinations.

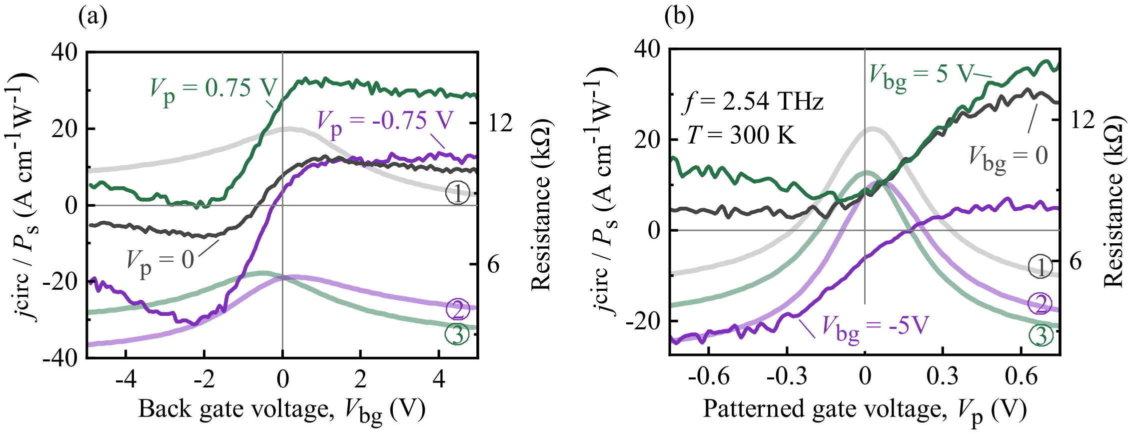

Figure 5.6 | Circular photocurrent densities $j^{\text{circ}} = U^{\text{circ}}/(R_\text{s}w)$ normalised to the power versus back gate (a) and patterned gate voltage (b) for different values of the gate voltages. The right axes relate to the resistance given by the curves with reduced opacity measured for the same gate voltages as the photosignal: in panel (a) ① $V_\text{p} = 0$, ② $V_\text{p} = -0.75\,\text{V}$, ③ $V_\text{p} = 0.75\,\text{V}$; and in panel (b) ① $V_\text{bg} = 0$, ② $V_\text{bg} = -5\,\text{V}$, ③ $V_\text{bg} = 5\,\text{V}$. Adapted from Ref. [122].

6 Magneto-ratchets in patterned-gated graphene

In the previous chapters the graphene metamaterial was investigated and discussed for zero magnetic field. In particular, the photoresponse of the device was studied in terms of polarisation states and applied gate voltages. In this chapter the main subject is the magneto-ratchet effect obtained in the presence of a magnetic field. As presented by the data and discussed in the second section, in this regime Shubnikov–de Haas oscillations (SdHO) and cyclotron resonance (CR) are important features emerging in the photocurrents. All data in this chapter were detected at liquid helium temperature and were obtained from sample G2.

6.1 Experimental results on magneto-ratchets

When the sample was excited at normal incidence with linearly polarised radiation $\boldsymbol{E} \parallel \hat{\boldsymbol{x}}$ of frequency $0.69\,\mathrm{THz}$, a photosignal U_x was observed that oscillates with the magnetic field. Figure 6.1 shows the sign-alternating oscillations for a fixed back gate voltage of $V_{\mathrm{bg}} = 5\,\mathrm{V}$ for different patterned gate voltages. Strikingly, the photosignal amplitudes are several orders of magnitude larger than the signals measured at zero magnetic field. In fact, it was observed that the amplitude of the oscillations grow exponentially. Apparently, the photosignal is connected to the resistance of the sample (grey curves in Fig. 6.1) which also has oscillatory behaviour and was measured without illumination. Comparing the established SdHO in the resistance with the photocurrent reveals that for some gate voltage sequences, the magneto-ratchets follow the SdHO in period and phase. This can be seen clearly in Figs. 6.1(a)–6.1(c), in which the extrema of the ratchet signal coincide with the extrema of the SdHO. These findings demonstrate that the magneto-oscillations observed in the ratchet signal and the SdHO in the resistance are both associated with Landau quantisation. On the contrary, for some combinations of V_{p} and V_{bg} the oscillations in the ratchet current are more complex and deviate from the SdHO, as seen in Fig. 6.1(d).

In order to examine these profound differences in greater detail, the magneto-ratchet

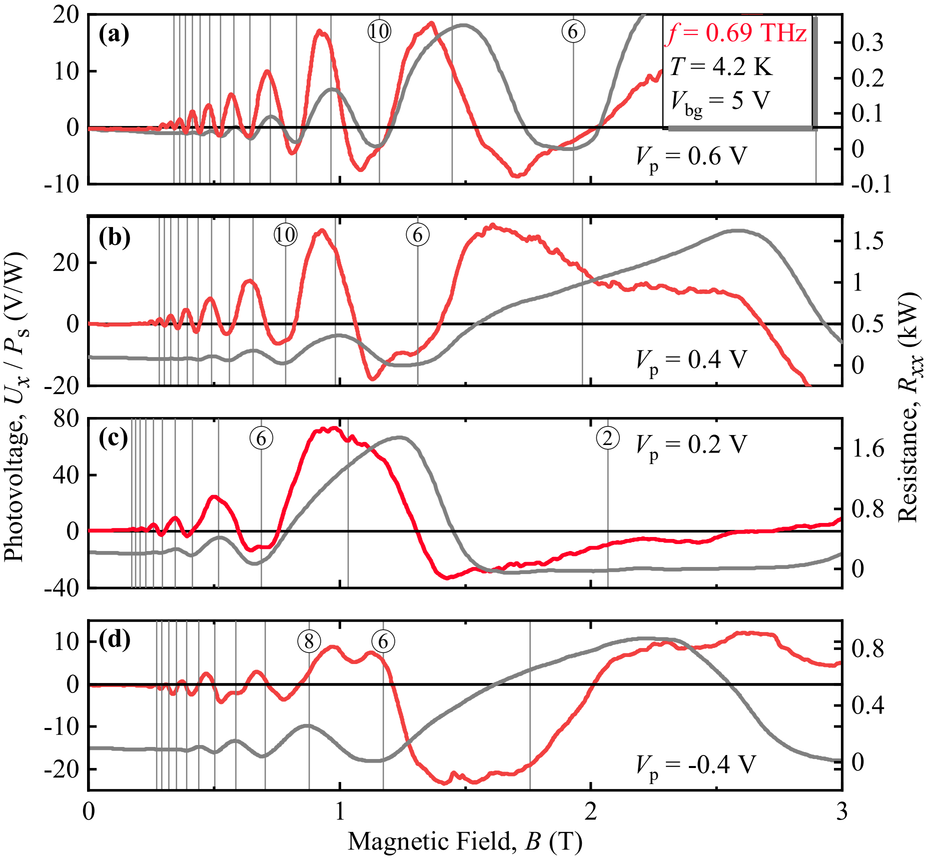

Figure 6.1 | Photovoltage measured in x-direction normalised to radiation power in response to the magnetic field at fixed back gate voltage and different patterned gate voltages. The data were obtained measuring with linear polarisation $\boldsymbol{E} \parallel \hat{\boldsymbol{x}}$, i.e. $\alpha = 90°$. Grey curves are the corresponding longitudinal resistances R_{xx}. The vertical lines indicate even filling factors of the resistance with some values given by the encircled numbers. Adapted from Ref. [123].

and the magneto-resistance were measured at fixed patterned gate voltage $V_\mathrm{p} = 0.6\,\mathrm{V}$ and for back gate voltages ranging from $-0.8\,\mathrm{V}$. to $1.2\,\mathrm{V}$ The data are presented in Fig. 6.2 and demonstrate that the oscillations in the ratchet signal are markedly sensitive to the applied back gate voltage [Fig. 6.2(a)], whereas the SdHO in the resistance persist unaltered. This can also be seen in Figs. 6.2(c) and 6.2(d). Figure 6.2(c) depicts the Fast Fourier Transform (FFT) amplitudes of the photosignal U_x (full circles and lines) and of the resistance R_{xx} (open circles and double lines). Whereas the maximum of the FFT amplitude of U_x shifts with V_bg, the maxima of R_{xx} (see grey rectangle) remains unaltered. The signal U_y measured under the same conditions along the bases of the triangles shows similar behaviour as U_x; see Fig. 6.3.

Similar measurements were conducted with a much higher radiation frequency of 2.54 THz. In addition to the magneto-oscillations, resonant enhancement of the ratchet signal was observed in U_y, as shown in Fig. 6.4. In order to investigate this

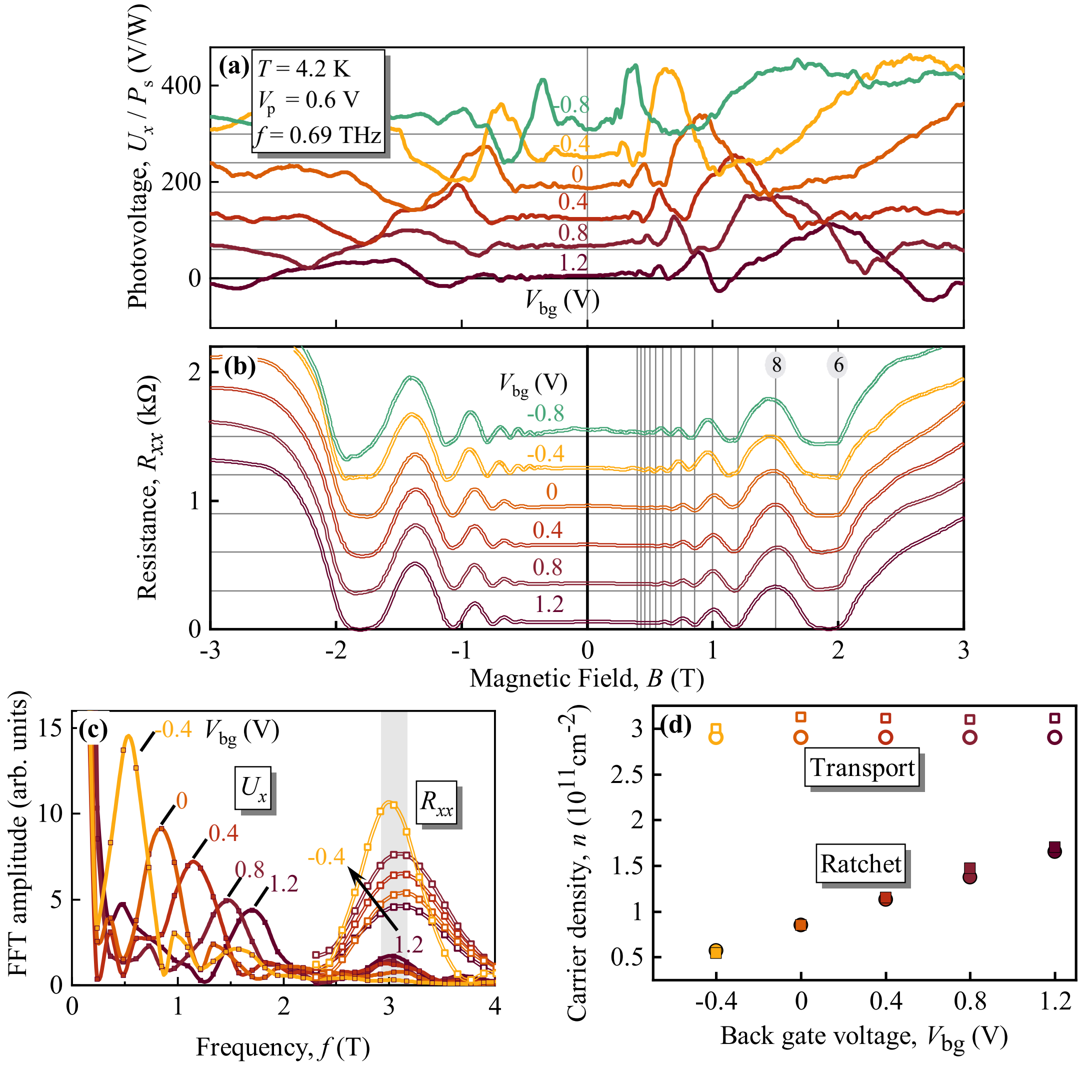

Figure 6.2 | U_x/P_s versus magnetic field for numerous back gate voltages for an azimuth angle $\alpha = 90°$ shifted by $60\,\mathrm{V/W}$ (a), and the corresponding resistance shifted by $0.3\,\mathrm{k\Omega}$ (b). Vertical lines indicate the even filling factors for one B-field polarity and encircled numbers denote values for the filling factor. Panel (c) shows the fast Fourier transform (FFT) of U_x (filled circles, solid lines) and R_{xx} (open circles, double line) where spline lines are a guide for the eye. Panel (d) shows the carrier density extracted from the photosignal oscillations (filled symbols) and R_{xx} (open symbols). The rectangles and circles show the density obtained from the FFT and filling factor, respectively. The data were obtained measuring with linear polarisation $\boldsymbol{E} \parallel \hat{\boldsymbol{x}}$. Adapted from Ref. [123].

resonance, measurements were performed with circularly polarised radiation. The results, illustrated in Fig. 6.4(a), distinctly indicate that the resonance is responsive to right- (CR$_+$) or left-handed (CR$_-$) light for one B-field polarity, and is therefore attributed to CR. For specific combinations of V_p and V_bg, two separated resonances were detected, as marked by the solid and dashed green arrows in Fig. 6.4(b), which depicts the evolution of the signal for various patterned gate voltages for one B-field

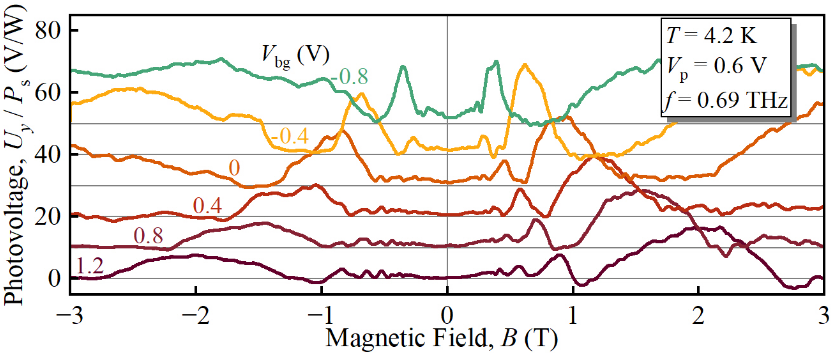

Figure 6.3 | U_y/P_s measured along the bases of the triangles as a function of magnetic field for numerous back gate voltages for $\alpha = 90°$. For visibility, the curves are shifted by 10 V/W. Adapted from Ref. [123].

polarity and σ^--polarised THz radiation. The two resonance field positions B_res dependent on the gate voltage are shown in the inset in Fig. 6.4(b). It can be seen that increasing the gate voltage from −0.75 V to −0.6 V reduces the values of the resonance fields. This is expected for graphene with its linear energy dispersion, as the CR position depends on the carrier density. The purple line is the calculated position of the densities obtained from transport measurements. The resonance is not only influenced by the patterned gate voltage but also by the back gate voltage, as shown in Fig. 6.4(c). Note that CR-enhanced magneto-ratchets were also observed in the photosignal U_x; see Ref. [123].

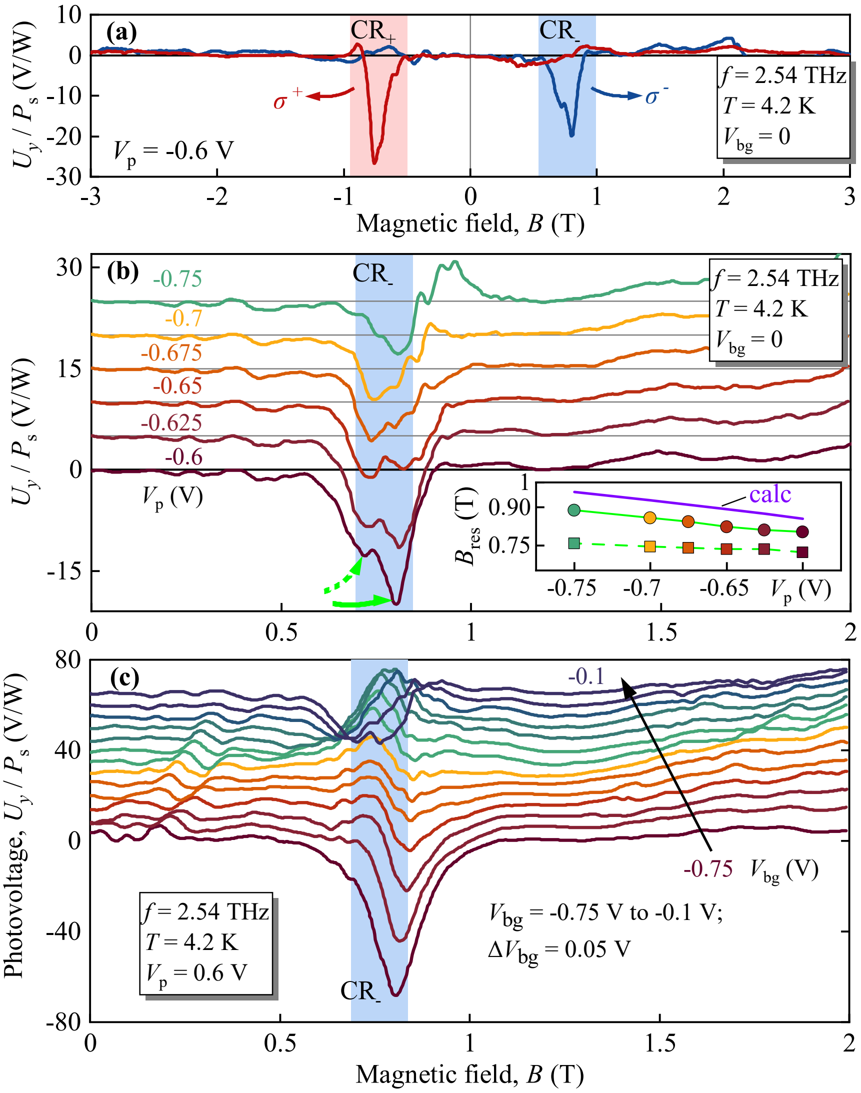

Figure 6.4 | Photosignal normalised to power measured in the y-direction dependent on magnetic field. Panel (a) shows the CR traces for opposite helicities. Panel (b) presents data for σ^{-}-radiation for zero back gate voltage and various patterned gate voltages. The two resonance peaks are indicated by the dashed and solid green arrow. The inset shows the position of the two resonant magnetic fields versus patterned gate voltage, with the purple line being the calculated positions from transport data. Panel (c) show the traces for fixed patterned gate and various back gate voltages. In (b) and (c) all curves are up-shifted by 5 V/W for better visibility. Adapted from Ref. [123].

6.2 Discussion

This section evaluates the experimental data of the magneto-ratchets. It begins with the oscillations in the photovoltage and their relation to the SdHO from transport measurements. First, the SdHO in R_{xx} are elaborated in order to acquire deeper insights to the formation of the photocurrents, which are dependent on the employed gates and the magnetic field. The grey traces in Figs. 6.1(a)–6.1(c) demonstrate that the longitudinal resistance is notably sensitive to the patterned gate voltage, whereas

Fig. 6.2(b) shows that R_{xx} is nearly immune to changes in the back gate voltage. This result can be attributed to the fact that the area of graphene above the antidots constitutes only 16 % of the total area of the graphene flake. Moreover, the density of the carriers situated in graphene between the antidots is governed by the patterned gate, which is positioned approximately ten times closer to graphene than the back gate. As a consequence, the period of the SdHO in R_{xx} is predominantly governed by V_p, and hence SdHO allow for accessing the carrier density outside the triangles. A function for the resistance and its oscillation in the presence of a magnetic field is known [96,133]:

$$R_{xx}(B) = R_{xx}(B=0) \times (1 + 2\delta_\mathrm{c}) \,, \tag{6.1}$$

with

$$\delta_\mathrm{c} = 2\cos\left(\frac{\pi E_\mathrm{F}}{\hbar\omega_\mathrm{c}}\right) \exp\left(-\frac{\pi}{\omega_\mathrm{c}\tau_\mathrm{q}}\right) \frac{\Psi}{\sinh\Psi} \,. \tag{6.2}$$

Here, E_F is the Fermi energy, $\omega_\mathrm{c} = eBv_0^2/E_\mathrm{F}$ the cyclotron frequency with the Fermi velocity v_0, τ_q is the quantum scattering time, and $\Psi = 2\pi^2 k_\mathrm{B}T/(\hbar\omega_\mathrm{c})$. The argument of the cosine in Eq. (6.2) can be rewritten by introducing the filling factor $\nu = 2\pi\hbar n_\mathrm{e}/(eB) \equiv 2E_\mathrm{F}/(\hbar\omega_\mathrm{c})$ yielding $\cos(\pi\nu/2)$. With the filling factor analysis, i.e. fitting all minima and maxima of the SdHO at even filling factors with the parameter n_e, the carrier density can be attained as $n_\mathrm{e} = \{2.8, 1.9, 1\} \times 10^{11}\,\mathrm{cm}^{-2}$ for $V_\mathrm{p} = \{0.6, 0.4, 0.2\}\,\mathrm{V}$, respectively [see Figs 6.1(a)–6.1(c)]. The results are in line with the density dependence found from Hall measurements, presented in Fig. 3.6(d) for the sample characteristics in Sec. 3.3.

Now, the discussion turns to the THz magneto-ratchet oscillations observed in the photovoltage. Such THz-induced oscillations have been reported previously in monolayer [96] and bilayer [14,17] graphene 1D metamaterials. It has been demonstrated that these photosignals can be described by [17,96]:

$$(j_x + ij_y)_\mathrm{1D} = \Xi_x \left(\frac{2\pi E_\mathrm{F}}{\hbar\omega_\mathrm{c}}\right)^2 \delta_\mathrm{c} \times (C_0 + C_1P_1 + C_2P_2 + C_\mathrm{circ}P_\mathrm{circ}) \,, \tag{6.3}$$

where j_x is the real and j_y the imaginary part, $P_{1,2,\mathrm{circ}}$ are the Stokes parameters, and $C_{0,1,2,\mathrm{circ}}$ are functions of frequency, transport relaxation time, and magnetic field; see Appendix of Ref. [96]. Equation (6.3) is composed of the product of the lateral asymmetry factor Ξ_x and the characteristics of the graphene sample, including the Fermi energy and relaxation times. This product form enables one to generalise the expression to the case of 2D modulations, as suggested in Ref. [123]: in the regime in which $\Xi_{x,y}$ are linear, the 2D modulation can be regarded as two superimposed structures with independent modulations in the x- and y-directions. As a result, the expression of the 1D case can then be applied to the components of the ratchet current along and perpendicular to the 1D modulation directions, yielding [123]:

$$(j_x + ij_y)_{2\mathrm{D}} = (\Xi_x + i\Xi_y)\left(\frac{2\pi E_\mathrm{F}}{\hbar\omega_\mathrm{c}}\right)^2 \delta_\mathrm{c} \times (C_0 + C_1 P_1 + C_2 P_2 + C_\mathrm{circ} P_\mathrm{circ})\,. \quad (6.4)$$

Here, $C_{0,1,2,\mathrm{circ}}$ are the same functions as in Eq. (6.3) for 1D modulation. In particular, this theory predicts that the amplitudes of the oscillations in the ratchet currents are substantially larger than the ratchet current at $B = 0$ due to the enhancement factor $[2\pi E_\mathrm{F}/(\hbar\omega_\mathrm{c})]^2 \gg 1$, as observed in the experiments. As this factor does not appear in the SdHO in R_{xx} [see Eq. (6.1)], the magneto-oscillations can emerge at much lower magnetic fields (higher filling factors) than the SdHO in the resistance; see Fig. 6.1. Physically, this additional enhancement factor in the magneto-ratchet appears because the transport parameters of graphene in the SdHO regime are modulated on the energy scale. The period of the modulation is the cyclotron energy $\hbar\omega_\mathrm{c}$, which is substantially smaller than the Fermi energy. Given that ratchet currents incorporate second-order derivatives with respect to energy [see, e.g. Eqs. (2.36) and (2.43)], the enhancement factor emerges.

Figures 6.1(a)–6.1(c) demonstrate that for relatively low modulations of $V(\boldsymbol{r})$, the oscillations of the ratchet current are in phase with the SdHO in R_{xx}. Thereby, low modulation is associated with comparable magnitudes of the gate voltage–induced electric fields of the two employed gates. As the back gate is about ten times farther from graphene than the patterned gate, applying $V_\mathrm{bg} = 5\,\mathrm{V}$ is supposed to affect the potential amplitude to a similar extend as applying $V_\mathrm{p} = 0.5\,\mathrm{V}$, but in different spatial regions. In contrast, higher modulations, i.e. V_bg and V_p have large magnitudes and are different in sign, involve more nuanced oscillations, which do not simple follow the SdHO; see Fig. 6.1(d).

The comparison between $R_{xx}(B)$ and the magneto-ratchet can be seen in Fig. 6.2. Whereas $R_{xx}(B)$ [Fig. 6.2(b)] does not change with the back gate voltage, the photosignal is highly sensitive to variations in V_bg [Fig. 6.2(a)]. This is analysed in the FFT spectrum in Fig. 6.2(c) revealing that two different peaks are present: a low-frequency and a high-frequency peak. For the ratchet signal, the low-frequency peak shifts to smaller values for decreasing gate voltages, whereas the less prominent high-frequency peak does not shift with the gate voltage. In contrast, there is only one peak in the FFT spectrum for $R_{xx}(B)$, which behaves very similar to the high-frequency peak of the FFT analysis of U_x. Therefore, the two different types of peaks are attributed to distinct densities, namely the carrier density in graphene in the interior [low-frequency peaks, mainly controlled by V_{bg}] and exterior [high-frequency peaks, mainly controlled by V_{p}] above the antidots. This conclusion is strongly supported by the ratchet density that is linearly dependent on the back gate voltage signal; see Fig. 6.2(d). The different spatial origin of the ratchets can be related to the characteristic of ratchets, i.e. to the joint action of the asymmetric electrostatic field and the THz near-field. As both fields should be strongly affected by variations in the density of states on both sides of the triangle edges, a complex magneto-ratchet photosignal is expected [123], which has indeed also been observed in the experiments. As the ratchet current is sensitive to local parameters, the oscillations are dependent on the strength of the modulation, which is achieved by varying V_{bg}. However, the resistance depends on the global charge density average, which is dominated by the large area between triangles, and is hence almost immune to the amplitude of the modulation. In addition, in the regime of low filling factors and the presence of the quantum Hall effect, fast changes in the density of states, localisation effects, or edge states at the triangles' boundaries may promote the responsivity of local fields to the gate voltages. Conclusions on concrete mechanisms under this deeply quantum-mechanical condition are out of scope of this thesis and requires further research.

In order to substantiate the behaviour of the longitudinal resistance and the magneto-ratchet at low magnetic fields, the data of Fig. 6.1(a) and Fig. 6.1(b) are shown for small B-fields. The traces are shown by circles in Fig. 6.5(a) and 6.5(b), and Fig. 6.5(c) and 6.5(d), respectively. Solid lines are fits according to Eqs. (6.1) and (6.4). Considering the SdHO in the resistance, only the quantum scattering time τ_{q} is a crucial fitting parameter because the other ones can be obtained independently from the period of the oscillations and from $R_{xx}(B=0)$. As a result, the parameter $\tau_{\mathrm{q}} = 0.1\,\mathrm{ps}$ is a good value for describing the behaviour of the SdHO in the resistance [Fig. 6.5(b) and 6.5(d)]. However, at higher magnetic fields the approximation of strongly overlapping Landau levels does not hold, and thus the model becomes inappropriate. The same parameters were used to fit the magneto-ratchets U_x, shown in Fig. 6.5(a) and 6.5(c). These magneto-oscillations depend on the enhancement factor $[2\pi E_{\mathrm{F}}/(\hbar\omega_{\mathrm{c}})]^2 \propto B^{-2}$, which gives rise to a less pronounced decay of the oscillations towards small B-fields compared to the SdHO. Fitting the magneto-ratchets with $U_x = CB^{-2}\delta_{\mathrm{c}}$, where C is a constant, reveals that the enhancement factor provides an excellent description of the experimentally observed decline in the magneto-oscillations towards low B-fields.

Next, the CR-induced ratchet signal observed for a radiation frequency of 2.54 THz is

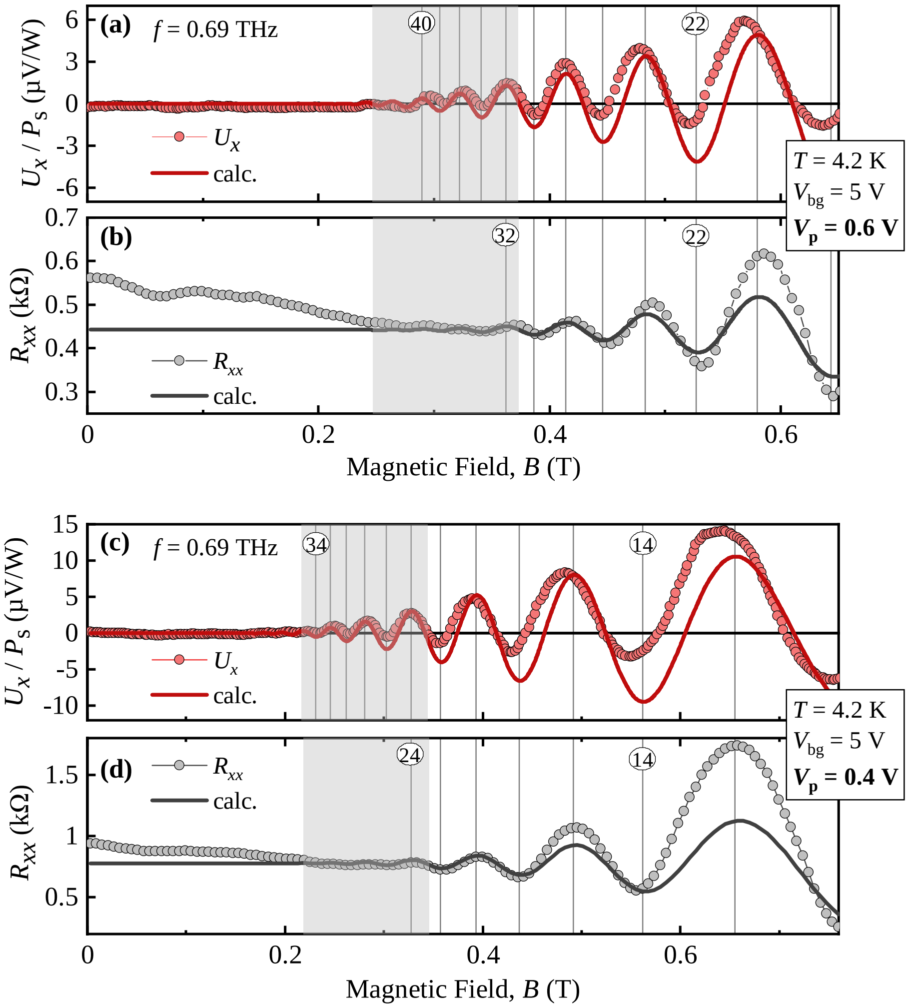

Figure 6.5 | Normalised photovoltage (red traces) measured along the x-direction versus magnetic field and the corresponding transport measurements (grey circles). The data of the upper panels were obtained for $V_\mathrm{p} = 0.6\,\mathrm{V}$, and the lower panels for $V_\mathrm{p} = 0.4\,\mathrm{V}$. Vertical lines indicate the magnetic fields for even filling factors, given by the encircled numbers. The grey areas indicate the range of the onset of the quantum oscillations in the photosignals, and solid lines are fits according to Eqs. (6.1) and (6.4). Adapted from Ref. [123].

discussed; see Fig. 6.4. A clear evidence that the observed traces are indeed related to CR is the helicity dependence: changing the helicity from σ^+ to σ^- inverts the polarity of the resonance B-field, as demonstrated in Fig. 6.4(a). Another evidence for CR is that the position of the resonance field is shifted towards larger magnetic field magnitudes with increasing $|V_\mathrm{p}|$, as seen in the inset in Fig. 6.4(b). This accords with the dependence of the carrier concentration in areas outside the triangles, which can be estimated from the resistance data according to $B_\mathrm{res} = \hbar\omega\sqrt{\pi n}/(ev_0)$; see calculated purple line ("calc") in Fig. 6.4(b). Although the dependence on the density of the experimentally measured resonance fields is in line with the calculated values, the magnitude is slightly different. This is due to the different areas in the sample in which the magneto-ratchets and the SdHO in the resistance are generated.

For B-fields close to CR condition, the ratchet current in graphene exhibits resonant behaviour that is similar to the one in systems with massive carriers, such as considered in a 1D bilayer graphene metamaterial in Ref. [17]. In an illustrative description, this means that the Drude absorption is resonantly enhanced. When one expands the C coefficients at $\omega \approx \omega_\mathrm{c}$, the ratchet currents in the 2D metamaterial are according to Ref. [123] expressed by

$$j_{x,y} = \frac{e^3 v_0^2}{8\pi\hbar^2 E_\mathrm{F}\omega^3}\left(\frac{2\pi E_\mathrm{F}}{\hbar\omega_\mathrm{c}}\right)^2 \delta_\mathrm{c}\frac{\Phi_{x,y}(\epsilon)}{1+\epsilon^2}\,, \tag{6.5}$$

where $\epsilon = (\omega - \omega_\mathrm{c})\tau$ with transport relaxation time τ and

$$\Phi_x = (\epsilon\Xi_x - 2\Xi_y)(1+P_1) - (2\Xi_x + \epsilon\Xi_y)P_2 + \left[(1+\epsilon)\Xi_x + \epsilon\Xi_y\right]P_\mathrm{circ}\,. \tag{6.6}$$

Φ_y has a similar dependence and is given by Eq. (6.6) when replacing $\Xi_x \to \Xi_y$ and $\Xi_y \to -\Xi_x$. The expressions given above illustrate that the x- and y-components of the polarisation-dependent and -independent ratchet currents close to the CR exhibit Fano shapes that are either symmetric or asymmetric functions of the detuning parameter ϵ, depending on the ratio Ξ_x/Ξ_y [123].

Nex, the complex shape of the CR curves are discussed; Fig. 6.4(a) and selected curves in Fig. 6.4(b). These manifold shapes can be regarded as two different, superimposed minima of the common Lorentzian shape. Such a characteristic has recently been reported in Ref. [17], in which bilayer graphene with a 1D modulation was investigated. The authors have demonstrated that the simultaneous excitation of magneto plasmons and cyclotron modes can result in two Lorentzian dips, similar as observed in the experiments in this work. However, in the 2D metamaterial the CR shape is much more complex due to the strong altering of the shape by the two gates; see Figs. 6.4(b) and 6.4(c). In order to investigate these alterations in greater detail, the data are re-plotted without vertical up-shift; see Fig. 6.6. Strikingly, for B-fields far from CR condition, the magneto-oscillations in the studied range of gate voltages are markedly dependent to the back gate voltage, but nearly independent of the patterned gate voltage. In contrast, for B-fields around the CR condition (marked by blue areas), additional and weak short-period oscillations manifest, which might be a possible origin for the fine structure of the CR and the two distinct minima present at certain combinations of V_bg and V_p. The characteristics of these short-period oscillations and their potential correlation with magneto plasmon modes

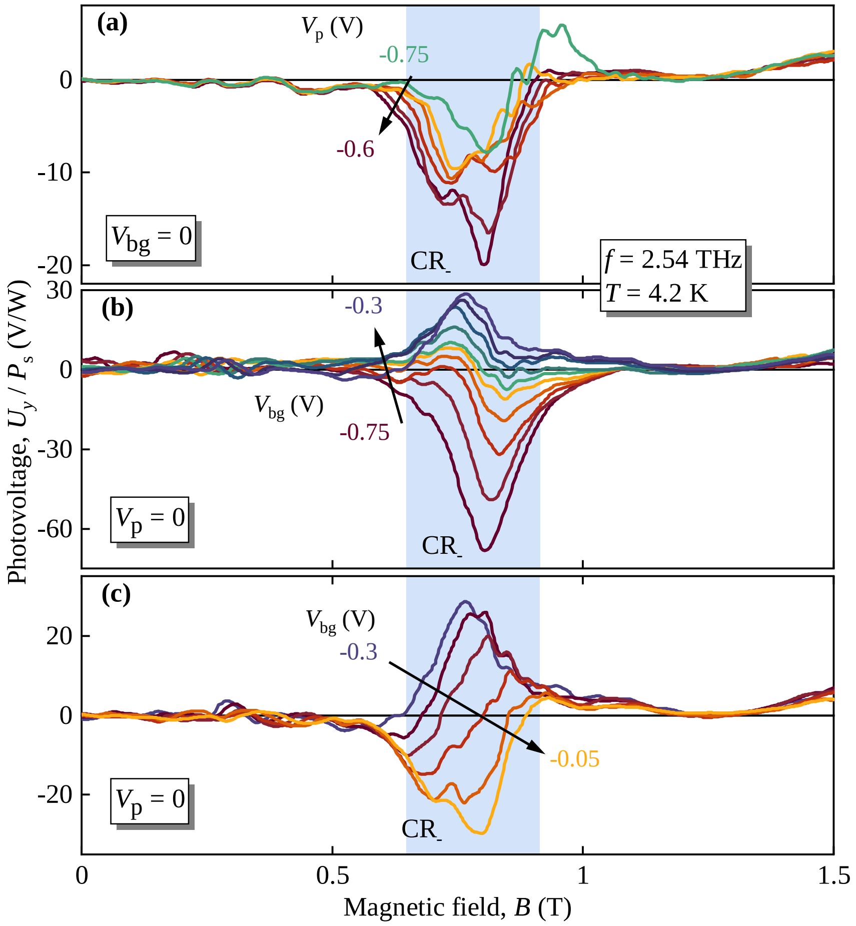

Figure 6.6 | Cyclotron resonance traces measured in U_y for zero back gate voltage and different patterned gate voltages [panels (a) and (b)], and for zero patterned gate voltage and different back gate voltages (c). Adapted from Ref. [123].

remain unclear and is a topic for future research. Interestingly, the envelope of the CR curve may be described by a single Lorentzian peak/dip or a combined shape of neighbouring peak and dip, which is also described by the theory in Eq. (6.5), predicting that the shape depends on the ratio Ξ_x/Ξ_y and can be composed of a symmetric (Lorentzian) and antisymmetric (Fano) shape: the ratio Ξ_x/Ξ_y depends on the gate voltages, consequently the shape of the CR curve [123]. The CR conceptually enhances the magneto-oscillations, and therefore it can have a gate-dependent sign. Qualitatively, this explains the non-trivial modification of the CR shape.

As a final remark, it is noted that in this sample electron spin resonance (ESR) have been observed in the magneto-ratchet photovoltage signal for GHz radiation [123]. The data, recorded by the group of Prof. Dr. Frédéric Teppe, reveal a Landé factor $g = 2$, as expected for graphene. In Ref. [123], the ESR ratchet has been attributed to resonant direct optical transitions between spin subbands, leading to stronger electron gas heating, and consequently to an additional Seebeck ratchet mechanism.

As this contribution is generated in addition to indirect optical transitions (which may have opposite signs), for certain frequencies the GHz-induced magneto-ratchet signal can be suppressed. This has been demonstrated to be possible independently of the patterned gate voltage [123].

7 Ratchets in the magnetic metamaterial

In the previous chapters have been studied graphene metamaterials in the presence of a gate-tunable carrier and potential modulation. However, the ferromagnetic metal in this chapter has by sample design a fixed 2D potential profile and electron density, as the ferromagnetic device has no gate. The important degree of freedom in this sample is the magnetisation of the 2D metal film. First, this chapter briefly shows the ratchet current behaviour upon polarisation with no magnetic field applied. Afterwards, the results with applied magnetic field are shown, which are intimately connected to the magnetisation of the sample.

7.1 Experimental results on the magnetic metamaterial

Prior to any applied magnetic field[1], the 2D ferromagnetic metamaterial is supposed to be in a magnetic multidomain state, which means that the magnetisation of all individual domains averages to a vanishing global magnetisation. By exciting the sample with THz radiation with a wavelength $\lambda = 118\,\mu\mathrm{m} \gg d$, which is much larger than the period of the metamaterial, the photosignal was observed to be polarisation-dependent. Figure 7.1(a) shows the photocurrents measured along the triangles' height (x-direction) and the triangles' bases (y-direction) as a response to the orientation of the radiation electric field vector $\boldsymbol{E}$. The data demonstrate minima and maxima as well as polarisation-independent contributions, which overall can be well described by the empirical fit equations

$$J_x = J_1 \cos 2\alpha + J_0\,, \tag{7.1}$$

$$J_y = -\tilde{J}_2 \sin 2\alpha + \tilde{J}_0\,. \tag{7.2}$$

---

[1] Note that in this chapter the magnetic field is denoted by H and given in units of $[\mu_0 H] = T$. This is, because in contrast to non-magnetised samples such as graphene the B-field in the sample is not equivalent to the external applied H-field: due to the presence of magnetisation it would read $B = \mu_0(M + H)$.

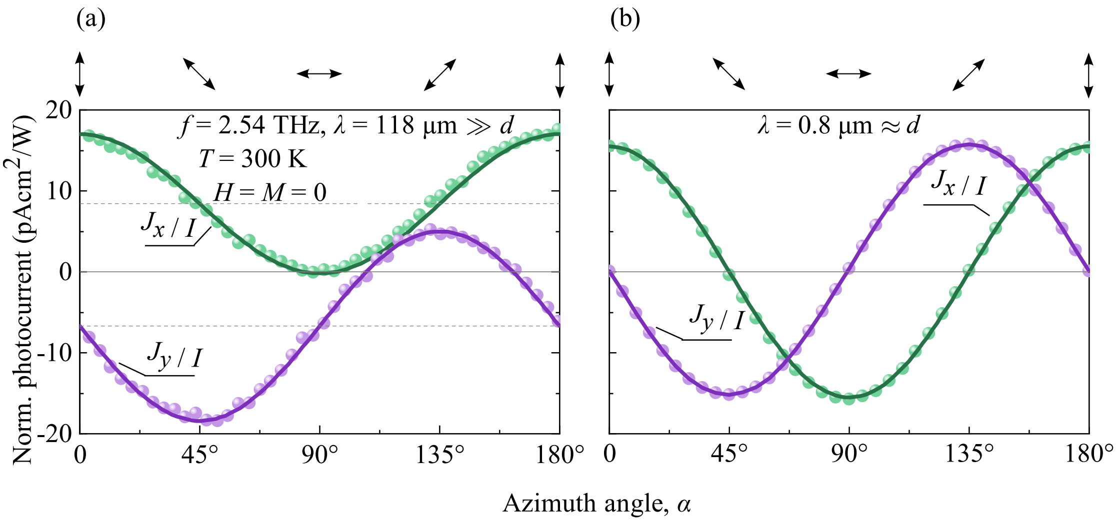

Figure 7.1 | Polarisation dependence of the photocurrents normalised to intensity, J_x/I (green) and J_y/I (purple), for zero magnetic field and zero magnetisation. Panel (a) shows the photosignals for a wavelength much larger than the triangles' period (118 µm $\gg d$), and panel (b) the photosignals for a wavelength in the order of the period (0.8 µm $\approx d$). The arrows on top indicate some polarisation states. Solid lines are fits according to Eqs. (7.1) and (7.2) yielding $J_1 = 8.6\,\text{pA}\,\text{cm}^2/\text{W}$, $J_0 = 8.5\,\text{pA}\,\text{cm}^2/\text{W}$, $\tilde{J}_1 = 11.7\,\text{pA}\,\text{cm}^2/\text{W}$, $\tilde{J}_0 = -6.7\,\text{pA}\,\text{cm}^2/\text{W}$ [panel (a)], and $J_1 = \tilde{J}_1 = 15\,\text{pA}\,\text{cm}^2/\text{W}$, $J_0 = \tilde{J} = 0$ [panel (b)]. Dashed lines indicate the offsets. Adapted from Ref. [125].

As shown in Fig. 7.1(b), the photocurrent was also recorded for a significantly smaller wavelength, $\lambda = 0.8\,\mu\text{m} \approx d$, which is comparable to the period of the artificial structure. The polarisation dependence of these data can also be described by Eqs. (7.1) and (7.2). The crucial difference for this wavelength regime is that the polarisation-independent part of the photosignal was neither detected in the x- nor in the y-direction; hence $J_0 = \tilde{J}_0 = 0$. The similarities and distinct differences between the photoresponses measured in the near-infrared and the far-infrared (THz) regime are addressed in in the discussion in Sec 7.2.

In the next step, the behaviour of the ratchet signal is investigated in case an external magnetic field $\mu_0 H$ is applied perpendicularly to the sample surface, i.e. along the easy axis of the magnetic anisotropy; see Chap. 3. Figure 7.2(a) shows the polarisation dependence measured in the x-direction for zero-magnetic field [compare Fig. 7.1(a)] and $\mu_0 H = \pm 2\,\text{T}$. The values were chosen so that the magnetisation M_z in the ferromagnetic metamaterial is saturated, $M_z = \pm M_\text{s}$, which means that H is sufficiently larger than the coercive field. It has been observed that under these conditions the photosignal is shifted in phase and also vertically depending on the polarity of M_z. This observation naturally suggests additional contributions to the empirical Eq. (7.1) that are odd and linear in M_z:

$$J_x = J_1 \cos 2\alpha + J_0 + M_z \left(J_2 \sin 2\alpha + J_{0,\mathrm{m}} \right) \,. \tag{7.3}$$

Using Eq. (7.3), the traces in Figure 7.2(a) can be decomposed into the parts that are even and odd in M_z:

$$J_x^{\mathrm{nm}} = \frac{1}{2} \left[J_x(+M_z) + J_x(-M_z) \right] \,, \tag{7.4}$$

$$J_x^{\mathrm{m}} = \frac{1}{2} \left[J_x(+M_z) - J_x(-M_z) \right] \,, \tag{7.5}$$

The result of this decomposition is shown in Fig. 7.2(b), substantiating that the even part is non-magnetic (superscript “nm”) and scales as $\cos 2\alpha$, and that the odd part is magnetic (superscript “m”) and scales as $\sin 2\alpha$.

Now, the behaviour of the photocurrent is investigated for values of the magnetisation that are smaller than the saturation magnetisation, i.e. the magnetic field dependence of the ratchet signal is studied. To differentiate all observed contributions, a new notation is introduced for the non-magnetic and magnetic parts:

$$J_{\mathrm{tr},x}^{\mathrm{nm}} + J_{\mathrm{S},x}^{\mathrm{nm}} = J_1 + J_0 \,, \tag{7.6}$$

$$J_{\mathrm{tr},x}^{\mathrm{m}} + J_{\mathrm{S},x}^{\mathrm{m}} = M_z J_2 + M_z J_{0,\mathrm{m}} \,. \tag{7.7}$$

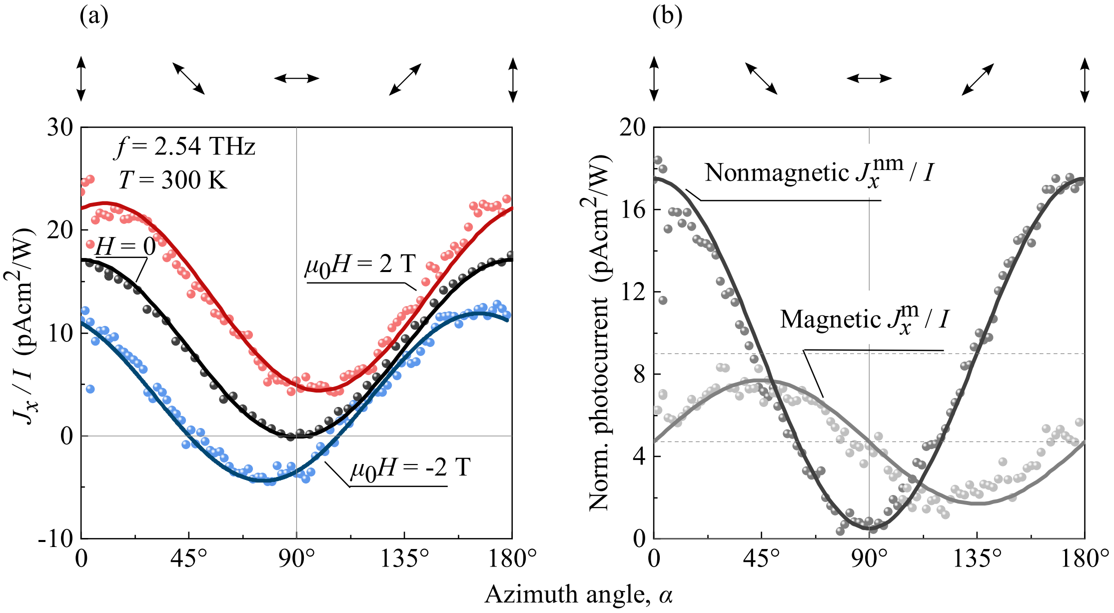

Figure 7.2 | Polarisation dependencies of the photocurrents for the x-direction normalised to intensity with arrows on top indicating some polarisation states. Panel (a) shows the photoresponse for three magnetic fields $\mu_0 H = 0, \pm 2\,\mathrm{T}$ with fit curves according to Eq. (7.3). Panel (b) shows the calculated magnetic and non-magnetic part according to Eq. (7.4): $J_1 = 8.5\,\mathrm{pA\,cm^2/W}$, $J_0 = 9\,\mathrm{pA\,cm^2/W}$, $J_2 = 3\,\mathrm{pA\,cm^2/W}$, and $J_{0,\mathrm{m}} = 5\,\mathrm{pA\,cm^2/W}$. Dashed lines indicate the offsets. Adapted from Ref. [125].

Here, in each line the first and second term on the left-hand side corresponds to the first and second term on the right-hand side, respectively. The subscripts “tr” (trigonal) and “S” (Seebeck) indicate the physical mechanism forming each contribution, namely polarisation-dependent scattering on triangles and polarisation-independent electron gas heating to which will be referred to in the discussion section.

The polarisation dependency measured in x-direction shown in Fig. 7.2(a) were repeated for numerous values of the magnetic field in the range $\mu_0 H = -2\,\mathrm{T}$ to $+2\,\mathrm{T}$ and $\mu_0 H = +2\,\mathrm{T}$ to $-2\,\mathrm{T}$ corresponding to the up- and down-sweep of the magnetic field, respectively. The obtained traces are depicted in Fig. 7.3. The magnetisation-independent contributions do not depend on the external magnetic field (see insets in Fig. 7.3), whereas the contributions odd in M feature a pronounced hysteresis for magnetic fields below the coercive field $\pm H_\mathrm{c}$ and are H-independent for large magnetic field magnitudes. Also, at large H-fields, inverting the H-field polarity results in a sign change of the contributions.

Figure 7.4 shows the hysteresis for a smaller H-field range. In particular, Figs. 7.4(a)–7.4(d) presents the measured photocurrent along the x-direction for the azimuth angles $\alpha = 0, 45°, 90°, 135°$. The grey curves relate to the right axes and show data of the normalised Faraday rotation angle that is proportional to magnetisation[2] [134]. The Faraday rotation measurement were conducted in the unpatterned Co/Pt film by the group of Prof. Dr. Matsubara at Tohoku University. It can be seen that for $\alpha = 0, 90°$, the width of the hysteresis matches the one of the Co/Pt film obtained from the Faraday angle measurement. Strikingly, for $\alpha = 45°, 90°$ the behaviour is more complex and a second jump emerges in the photosignal. As four all four azimuth angles either the sine or cosine contribution vanishes, taking the half-sums and half-differences, and using Eqs. (7.4) and (7.5), the two magnetic contributions can be extracted. The results are shown in Figs. 7.4(e) and 7.4(f). Indeed, the polarisation-dependent part J^m_tr exhibits a larger hysteresis width than the polarisation-independent part J^m_S.

---

[2] The Faraday effect incorporates that the polarisation plane of a linearly polarised light passing trough the magnetised sample is rotated by an angle, which is proportional to magnetisation. For the method and more details, in particular in the framework of this thesis, see Ref. [59].

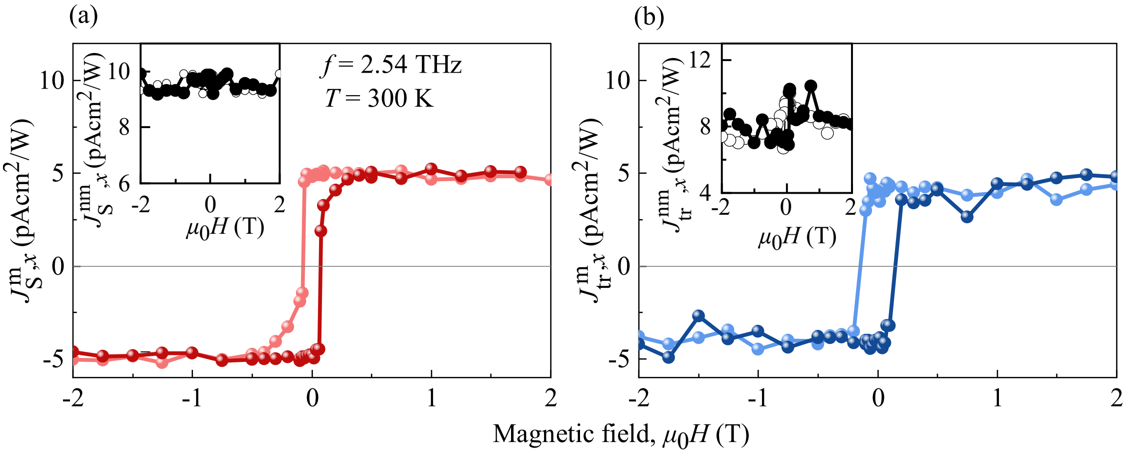

Figure 7.3 | Dependence of the contributions of Eq. (7.3) on magnetic field measured in the x-direction. Panel (a) shows the polarisation-independent, magnetisation-dependent part, and panel (b) the polarisation-dependent, magnetisation-dependent part. The insets show the corresponding magnetisation-independent traces. Dark and light traces corresponds to forward and backward sweep, respectively. Adapted from Ref. [125].

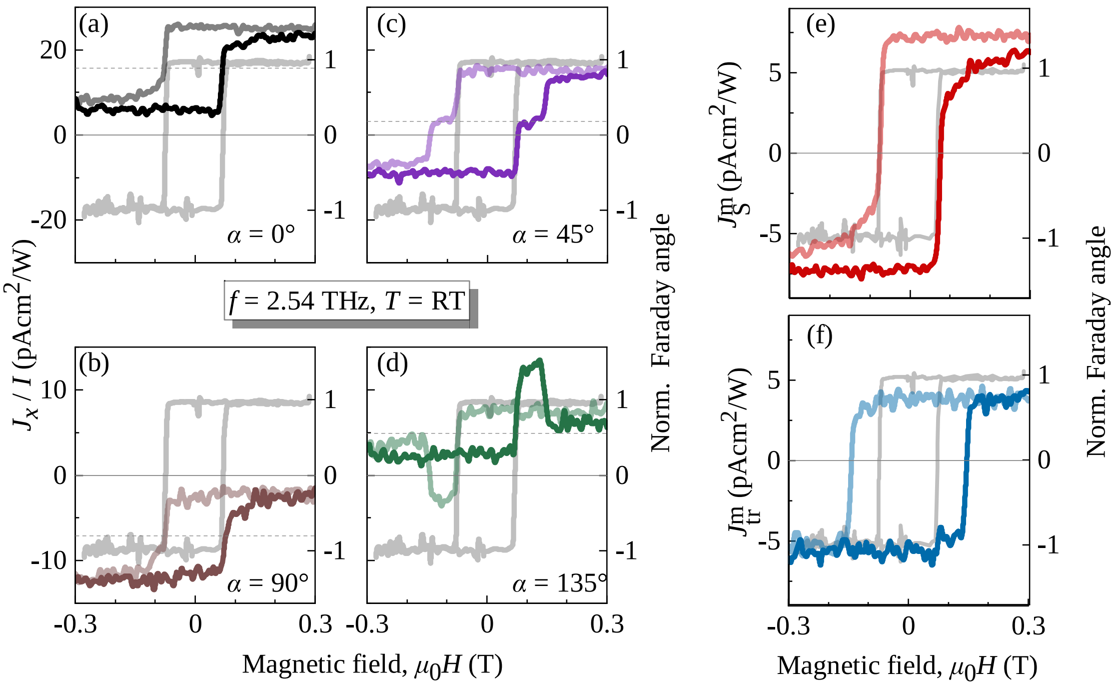

Figure 7.4 | Magnetic field dependencies for fixed azimuth angles, which have been chosen such that either the sine or cosine in Eq. (7.3) equals to zero [panels (a)–(d)]. Dark and light lines correspond to forward and backward sweeps, respectively. The grey curves correspond to the right axes and show the normalised Faraday rotation angle measured in the unpatterned Co/Pt stack. Grey curves and the red trace ($J^{\mathrm{m}}_{\mathrm{S}}$) have a coercive field of $\mu_0H \approx 76\,\mathrm{mT}$ and the blue trace ($J^{\mathrm{m}}_{\mathrm{tr}}$) of $\mu_0H \approx 144\,\mathrm{mT}$. Adapted from Ref. [125].

7.2 Discussion

This section analyses the data obtained from the ferromagnetic sample. Illuminating the sample at normal incidence with a radiation wavelength much larger than ($\lambda = 118\,\mu\text{m} \gg d$) or comparable to ($\lambda = 0.8\,\mu\text{m} \lesssim d$) the structure period d results in a ratchet current that is sensitive to the linear polarisation state of the radiation; see Fig 7.1 and 7.2. This reflects that the inversion center of the unstructured Co/Pt stack is broken if the sample is patterned by triangular holes, because in the unstructured Co/Pt film no ratchet signal has been detected for both wavelengths [59,125]. However, the crucial difference between both wavelengths is that in the THz regime a polarisation-insensitive contribution has been detected [Fig. 7.1(a)], which is absent for $\lambda = 0.8\,\mu\text{m} \lesssim d$. This behaviour is given by the empirical Eqs. (7.1), (7.2), and 7.3, demonstrating that the photocurrents vary with the Stokes parameters.

First, the polarisation-dependent (trigonal) photosignals are discussed. In Ref. [125] has been pointed out that the trigonal ratchets of both wavelength regimes share the same physical origin – scattering on individual triangles. However, the phenomenological equations should be different, as for $\lambda = 0.8\,\mu\text{m}$ individual triangles has to be considered and for $\lambda = 118\,\mu\text{m}$ the sample has to be regarded as a whole, i.e. as a metamaterial. According to Ref. [125], the point group symmetry of the regime of individual equilateral triangles is C_{3v}, describing three reflection planes and a three-fold vertical rotational axis. For this symmetry group the phenomenological equation reads for normal incident light [125]:

$$j_x = \chi P_1 E_0^2 + M_z \Phi P_2 E_0^2 \,, \tag{7.8}$$

$$j_y = -\chi P_2 E_0^2 + M_z \Phi P_1 E_0^2 \,. \tag{7.9}$$

Here, $P_1 = \cos 2\alpha$ and $P_2 = \sin 2\alpha$ denote the Stokes parameters. Apparently, in these equations no lateral asymmetry parameter emerges; instead, the squared amplitude of the radiation electric field E_0 appears explicitly. This reflects that individual triangles are distinct to the metamaterial regime and that the total signal is the sum of each triangle instead of being formed in the sample as a whole. Equations (7.8) and (7.9) yield that the amplitude of the trigonal ratchet ($M = 0$) is the same for the signals in x- and y-direction, since both include the same parameter χ. This has indeed been observed in the experiments, as shown in Fig. 7.1(b). Also, the magnetisation-dependent term should have the same amplitude for both measurement directions because the parameter Φ appears in j_x and j_y. This has been confirmed previously in Ref. [59].

In contrast, in the metamaterial regime ($\lambda = 118\,\mu\mathrm{m}$) the phenomenological equations are different. The observed experimental photosignals suggest C_s or C_1 symmetry. The former group includes the reflection plane (zx), the latter one only the identity operator. If the symmetry is reduced further to C_1, then all contributions possible for j_x are also allowed for j_y with independent coefficients, and vice versa. Moreover, for C_1 symmetry the additional lateral asymmetry parameter $\Xi_y = \langle E_0^2(\boldsymbol{r})\nabla_y V(\boldsymbol{r})\rangle$ occurs, as discussed for the graphene metamaterial. In order to maintain an overview of all individual contributions, in the following C_s symmetry is considered, which is sufficient to cover the microscopic mechanisms. According to Ref. [125], this symmetry allows for normal incident THz radiation for the following equations:

$$j_x = \Xi(\chi_1 P_1 + \chi_0) + M_z\Xi(\Phi_1 P_2 + \gamma P_{\mathrm{circ}})\,, \tag{7.10}$$

$$j_y = \Xi(-\tilde{\chi}_1 P_2 + \tilde{\gamma} P_{\mathrm{circ}}) + M_z\Xi(\tilde{\Phi}_1 P_1 + \Phi_0)\,, \tag{7.11}$$

with the lateral asymmetry parameter $\Xi = \Xi_x = \langle E_0^2(\boldsymbol{r})\nabla_x V(\boldsymbol{r})\rangle$, with $P_{1,2}$ as defined above, and $P_{\mathrm{circ}} = i(e_x e_y^* - e_x^* e_y)$. A comparison to Eqs. (7.8) and (7.9) of the C_{3v} point group of the individual antidots reveals differences: On one hand, χ, Φ become now independent for the x- and y-direction with the independent coefficients $\chi_1 \neq \tilde{\chi}_1$ and $\Phi_1 \neq \tilde{\Phi}_1$. This is in line with the experiments; see Fig. 7.1(a). Note that the data in x- and y-direction were measured at two separated arrays with identical fabrication but slightly different characteristics; see Figs. 3.7 and 3.8. On the other hand, two new polarisation-insensitive contributions arise, described by the parameters Φ_0 and χ_0, which are magnetisation-dependent and -independent, respectively. Also, helicity-dependent photocurrents become possible, but since they did not manifest themselves in the measurements, they will not be addressed further. If the sample has non-zero magnetisation, it has been observed that the polarisation dependence is phase shifted proportional to the magnetisation, as seen in Fig. 7.2. This finding accords very well with Eqs. (7.10) and (7.11).

The following microscopic theory has been developed in Ref. [125] and describes all polarisation-sensitive currents observed in the experiments, starting with the non-magnetic currents; see Fig. 7.1, and inset in Fig. 7.3(b). An overview of all proposed mechanisms is illustrated in Fig. 7.5. Using the Boltzmann kinetic equation and making the assumption of rare electron scattering on the edges of the triangles, the trigonal photocurrent parameters $\chi, \chi_1, \tilde{\chi}_1$ in Eqs. (7.8)–(7.11) can be expressed as [125,142]

$$\chi = -\frac{2Ne^3\tau_1}{m^* E_{\mathrm{F}}\,(1+\omega^2\tau_1^2)}\left[\frac{\mathrm{d}(\xi_{\mathrm{tr}} v_{\mathrm{F}} E_{\mathrm{F}} \tau_2)}{\mathrm{d}E_{\mathrm{F}}} - \frac{\mathrm{d}\tau_1}{\mathrm{d}E_{\mathrm{F}}}\frac{\tau_2}{\tau_1}\xi_{\mathrm{tr}} v_{\mathrm{F}}\frac{1-\omega^2\tau_1\tau_2}{1+\omega^2\tau_2^2}\right], \tag{7.12}$$

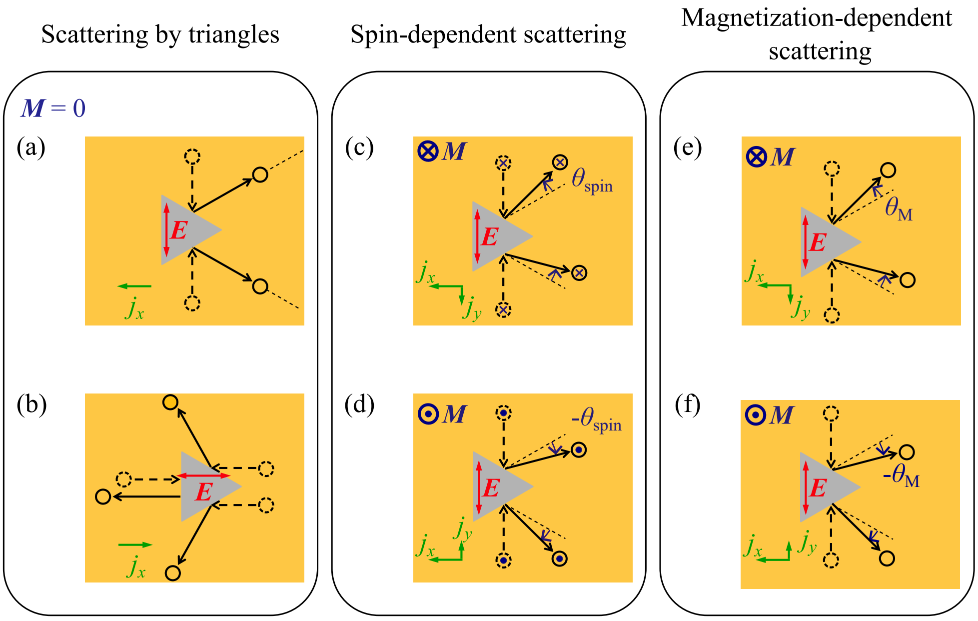

Figure 7.5 | Microscopic mechanisms for the polarisation-dependent photocurrents formed at an triangular antidot. The radiation electric field $\boldsymbol{E}$ (red double arrows) directs the carriers' motion. Initially incident electrons are indicated by dashed circles and dashed arrows and scattered off electrons by solid circles and solid arrows. Shown are only the predominant scattering directions. The generated currents (green arrows) depend on the following mechanisms: Panels (a) and (b) show the trigonal scattering without magnetisation for two perpendicular orientations of the electric field. In panels (c)–(f) only $\boldsymbol{E} \parallel \hat{\boldsymbol{y}}$ is depicted, with the spin-dependent scattering shown in panels (c) and (d) and the M-dependent scattering shown in panels (e) and (f). Adapted from Ref. [125].

where N is the 2D electron concentration, m^* the effective mass, E_F and v_F the Fermi energy and velocity, τ_1 the transport relaxation time, and τ_2 the radiation-induced momentum-alignment relaxation time. The quantities τ_1 and τ_2 are taken at the Fermi energy. The asymmetric scattering is described by the dimensionless quantity

$$\xi_\mathrm{tr} = \tau_1 \sum_{\boldsymbol{p}'} \left\langle W^\mathrm{a}_{\boldsymbol{p}\boldsymbol{p}'} \cos 2\varphi_{\boldsymbol{p}'} \cos 2\varphi_{\boldsymbol{p}} \right\rangle_{\varphi_{\boldsymbol{p}}} , \tag{7.13}$$

with averaging over $\varphi_{\boldsymbol{p}}$ with $\varphi_{\boldsymbol{p}}$ and $\varphi_{\boldsymbol{p}'}$ being the polar angles of the initial and final momenta, receptively. For example, for short-range scattering, ξ_tr is proportional to the density of states at E_F and the asymmetric scattering probability amplitude $W^\mathrm{a}_{\boldsymbol{p}\boldsymbol{p}'}$ is calculated by a product of the Bloch amplitude overlaps. This trigonal scattering that is present without magnetisation is illustrated in Figs. 7.5(a) and 7.5(b).

The polarisation-dependent photocurrent that is excited due to a non-zero magnetisation M_z is captured by the parameters $\Phi, \Phi_1, \tilde{\Phi}_1$; see Eqs. (7.8)–(7.11). For their origin, three mechanisms were proposed [125]: (i) the AHE, (ii) spin-dependent scattering, and (iii) magnetisation-dependent scattering.

The AHE has been conveyed in Sec. 2.2.2. Accordingly, magnetisation leads to a spin-dependent current. Translating this to the experimentally investigated photocurrents $\boldsymbol{j} \propto \boldsymbol{j}^{\mathrm{tr}} \times \boldsymbol{M}$ yields that the presence of magnetisation generates a component perpendicular to the trigonal current. Most often the extrinsic skew-scattering term dominates, as the conducting electron strongly interacts with the impurities, resulting in the photocurrent [125]

$$\boldsymbol{j} = \xi_{\mathrm{AHE}} P_{\mathrm{s}} \boldsymbol{j}^{\mathrm{tr}} \times \hat{\boldsymbol{z}} \,, \tag{7.14}$$

where $P_{\mathrm{s}} = -\Delta_{\mathrm{Z}}/(2E_{\mathrm{F}} \propto M_z)$ is the spin polarisation, and Δ_{Z} the Zeeman splitting. The dimensionless parameter describing the skew-scattering efficiency is given by [125]

$$\xi_{\mathrm{AHE}} = \tau_1 \left\langle \sum_{\boldsymbol{p}'} \sin\left(\varphi_{\boldsymbol{p}} - \varphi_{\boldsymbol{p}'}\right) W^{\mathrm{a,SO}}_{\boldsymbol{pp}'} \right\rangle_{\varphi_{\boldsymbol{p}}} \,. \tag{7.15}$$

A comparison of Eq. (7.14) with the phenomenological Eqs. (7.8) and (7.9) yields that $\Phi M_z = \xi_{\mathrm{AHE}} P_{\mathrm{s}} \chi$.

Skew-scattering does also give rise to spin-dependent scattering on the triangle boundary. In this case, spin-orbit interaction causes electrons with spin-up (spin-down) to be deflected by the angle $-\theta_{\mathrm{spin}}$ (θ_{spin}) relative to the trajectory for $M = 0$, as seen in Figs. 7.5(c) and 7.5(d). Accordingly, inverting the magnetisation inverts the sign of the perpendicular current. This behaviour is in accordance with the phenomenological Eqs. (7.8) and (7.9). In the microscopic picture, the photocurrents $j_{x,y} \propto M_z \Phi$ can be acquired analogue to above but with the replacements

$$N \to P_{\mathrm{s}} N \,, \quad \xi_{\mathrm{tr}} \to \xi_{\mathrm{SO}} \,, \tag{7.16}$$

and the spin-orbit asymmetry factor

$$\xi_{\mathrm{SO}} = \tau_1 \left\langle \sum_{\boldsymbol{p}'} \sin\varphi_{\boldsymbol{p}} \cos 2\varphi_{\boldsymbol{p}'} W^{\mathrm{a,SO}}_{\boldsymbol{pp}'} \right\rangle_{\varphi_{\boldsymbol{p}}} \,. \tag{7.17}$$

Here, $W^{\mathrm{a,SO}}_{\boldsymbol{pp}'}$ is the asymmetric scattering probability in which the Bloch amplitude overlap is modified by spin-orbit interaction.

The presence of magnetisation also influences the electron orbital motion. As a consequence, the carriers are deflected, regardless of having spin-up or spin-down, by an additional angle θ_M, whose sign reverses when the magnetisation is inverted, as illustrated in Figs. 7.5(e) and 7.5(f). The corresponding dimensionless parameter is

$$\xi_{\mathrm{M}} = \tau_1 \left\langle \sum_{\boldsymbol{p}'} \sin\varphi_{\boldsymbol{p}} \cos 2\varphi_{\boldsymbol{p}'} W^{\mathrm{a,M}}_{\boldsymbol{p}\boldsymbol{p}'} \right\rangle_{\varphi_{\boldsymbol{p}}} , \tag{7.18}$$

where in $W^{\mathrm{a,M}}_{\boldsymbol{p}\boldsymbol{p}'}$ magnetisation has to be included into the Bloch amplitudes. The factor $\xi_{\mathrm{M}} \propto M_z$ in the lowest order.

Next, the observed polarisation-insensitive ratchets are discussed, namely the Seebeck effect ratchet $J^{\mathrm{nm}}_{\mathrm{S}}$ and the magnetic Seebeck ratchet, i.e. the anomalous Nernst effect (ANE) ratchet $J^{\mathrm{m}}_{\mathrm{S}}$. The Seebeck contribution can be seen in particular in the offsets in Fig. 7.1(a), in the offset of the non-magnetic part J^{nm}_x in Fig. 7.2(b), and in the inset of Fig. 7.3(a). In contrast, the ANE ratchet can be seen especially in the offset of the magnetic part in Fig. 7.2(b), in Fig. 7.3(a), in Figs. 7.4(a) and 7.4(b) because the trigonal magnetic hysteresis vanishes for $\alpha = 0, 90°$, and in 7.4(e). Remarkably, the Seebeck and the ANE ratchet have not been observed for $\lambda = 0.8\,\mu\mathrm{m}$, as can be seen in Fig. 7.1(b) and in Ref. [59]. This is in accordance with the phenomenological Eqs. (7.8)–(7.11) and clearly demonstrates that the polarisation-insensitive currents are generated only due to the reduction of the symmetry, i.e. due to the new regime of a metamaterial achieved by increasing the wavelength such that $\lambda \gg d$.

The observation that for $\lambda = 118\,\mu\mathrm{m}$ the system's symmetry reduces from C_s to C_1 potentially results from different reasons: (i) the positions of the antidots may contrast with the designed lattice and can have slightly different shapes; and (ii) the beam spot is substantially larger than the patterned area, and therefore the structure can not be considered to be infinite, which is a prerequisite for the reflection plane of the C_s symmetry group. One argument from the experiments why the sample has C_1 symmetry is that the Seebeck ratchet was also detected in the y-direction, as can be clearly seen in Fig. 7.1(a). In terms of a microscopic illustration, the symmetry appears to be lowered from C_{3v} to C_s or C_1 because of the near-field of diffraction on the metallic edges of the triangles. This 2D near-field $\boldsymbol{E}(\boldsymbol{r})$ as well as the 2D electrostatic potential $V(\boldsymbol{r})$ have the same period as the antidot array. Together they have a joint action described by the lateral asymmetry parameter. The near-field-induced inhomogeneous temperature enhancement $\delta T(\boldsymbol{r}) \propto |\boldsymbol{E}(\boldsymbol{r})|^2$ and the potential gradient are schematically depicted in Fig. 7.6(a), demonstrating that the lateral asymmetry parameter does not average to zero because of the phase shift of $\delta T(\boldsymbol{r})$ with respect to the potential gradient. Furthermore, it is seen that the inhomogeneous heating is large at the edges of the antidots and in particular at points where three triangle apexes meet.

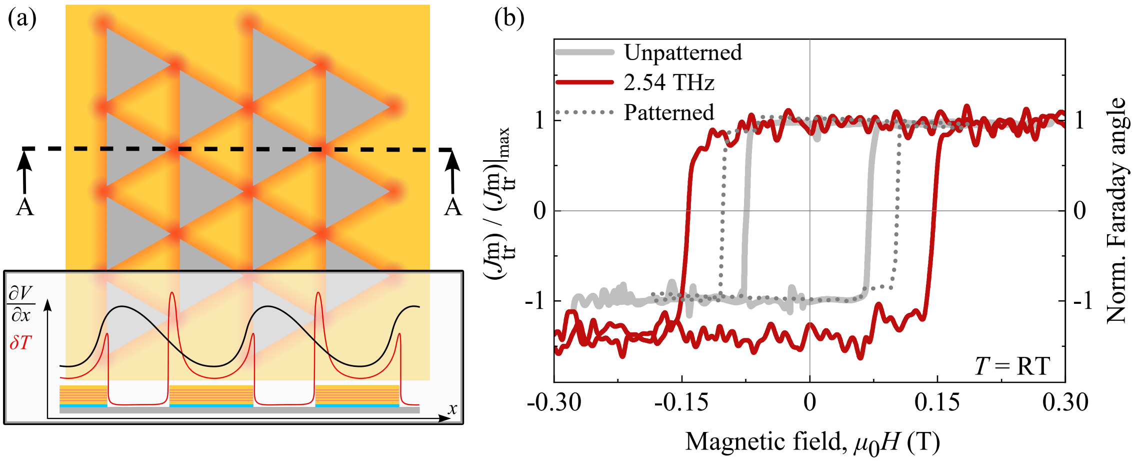

Figure 7.6 | Panel (a) shows the formation of the polarisation-independent Seebeck ratchet. The yellow square sketches the metallic multilayer film and the grey triangles the antidots. The red contour around these triangles illustrates the temperature enhancement due to the THz near field, $\delta T(\boldsymbol{r}) \propto E_0^2(\boldsymbol{r})$. The highlighted graph at the bottom shows $\delta T(\boldsymbol{r})$ and $\nabla_x V(\boldsymbol{r})$ along the cross section marked by the dashed line labelled AA. Panel(b) shows the normalised trigonal magnetic photocurrent (red) and the normalised Faraday rotation angles (grey). The latter were measured in the unpatterned (solid, $\mu_0 H_\mathrm{c} = 102\,\mathrm{mT}$) and in the triangular-patterned (dotted, $\mu_0 H_\mathrm{c} = 76\,\mathrm{mT}$) regions of the sample. Adapted from Ref. [125].

Following C_s symmetry, the non-magnetic Seebeck contribution J_S^nm is allowed in the x-direction and was detected in the experiments; see, e.g. Fig. 7.1(a). The intuitive explanation that this contribution is polarisation-insensitive is that the radiation-induced squared near-field amplitude $|\boldsymbol{E}_0|^2$ does not depend on the polarisation, and consequently the spatial temperature enhancement $\delta T(\boldsymbol{r}) \propto |\boldsymbol{E}_0|^2$ neither. In turn, the lateral asymmetry parameter does not depend on polarisation. The same arguments hold for the ANE contribution.

An equation for the Seebeck ratchet can be found in Ref. [125]:

$$j_x = -\frac{1}{2e}\frac{\partial \sigma_0}{\partial T}\left\langle \delta T(\boldsymbol{r}) \nabla_x V(\boldsymbol{r}) \right\rangle . \tag{7.19}$$

Expressing Eq. (7.19) in terms o the phenomenological Eq. (7.10), one acquires

$$j_x = \Xi \chi_0 = -\Xi \frac{\sigma_0 \tau_\mathrm{T} \partial \sigma_0 / \partial T}{e N k_\mathrm{B}(1 + \omega^2 \tau^2)} , \tag{7.20}$$

with the electron temperature relaxation time τ_T and the momentum relaxation time τ. The magnetic-induced ratchet effect $j_y = M_z \Phi_0 \Xi$ is similar to the Seebeck ratchet and is formed by inhomogeneous electron gas heating. For non-zero magnetisation, the dc conductivity tensor has an off-diagonal element σ_{yx} that is proportional to

M_z. The corresponding photocurrent is referred to as ANE ratchet and were shown in Ref. [125] to take the form

$$j_y(M_z) = -\frac{1}{e}\frac{\partial \sigma_{yx}}{\partial T}\left\langle \delta T(\boldsymbol{r}) \nabla_x V(\boldsymbol{r}) \right\rangle , \tag{7.21}$$

and associating with the phenomenological equation one can rewrite

$$j_y = M_z \Xi \Phi_0 = -\Xi \frac{2\sigma_0 \tau_{\mathrm{T}} \partial \sigma_{yx}/\partial T}{eNk_{\mathrm{B}}(1+\omega^2\tau^2)} . \tag{7.22}$$

The ANE ratchet current points perpendicularly to the underlying Seebeck ratchet current. This can be seen in particular in (i) Eqs. (7.10) and (7.11) for C_s symmetry for which $j_x = \Xi\chi_0$ and $j_y = M_z\Xi\Phi_0$, and (ii) in the microscopic Eqs. (7.20) and (7.22) showing that the Seebeck ratchet is proportional to $\partial\sigma_0/\partial T$, and the ANE ratchet scales with the off-diagonal component $\partial\sigma_{yx}/\partial T$ with $\sigma_{yx} \propto M_z$. It should be noted that the polarisation-insensitive contributions may also be described by the mechanism of dynamic carrier-density redistribution (DCDR), which is not based on electron gas heating. The DCDR for these contributions is related to the spatially varying electron concentration instead of temperature [2,19,58]. Both mechanisms have the same dependence of frequency, lateral asymmetry parameter, and polarisation. Distinguishing these mechanism experimentally is difficult and is out of scope of this thesis.

Before discussing the hysteresis, another mechanism for the formation of the polarisation-dependent photocurrents should be addressed. The mechanism of electron gas heating that leads to the ANE may be lateral anisotropic. This anisotropy can arise when considering the patterned area as a sequence of near-field antennas at points where three apexes of the antidots point to each other. The radiation absorption is maximal if the radiation electric field is aligned with the heights of the triangles, giving rise to the polarisation-dependent gradient $\nabla T(\alpha)$ that possesses trigonal space symmetry [125]. Thus, a photocurrent $\boldsymbol{j} \propto \boldsymbol{M} \times \nabla T(\alpha)$ may emerge that has the same polarisation- dependence as observed in the experiments.

Lastly, the hysteresis widths are analysed. Due to magnetisation, the ANE ratchet and the magnetic trigonal photosignal exhibit hysteresis; see Figs. 7.3(a) and 7.4(e), and Figs. 7.3(b) 7.4(f), respectively. However, as seen especially in Figs. 7.4(e) and 7.4(f), the widths of the hysteresis do not match. Strikingly, the coercive field of the ANE ratchet is even approximately two times smaller than the one of the magnetic trigonal ratchet. This difference in the hysteresis widths can be seen in the original data set measured for several azimuth angles; see Fig. 7.4(a)–7.4(d).

For $\alpha = 45°, 135°$, both J_S^m and J_tr^m were detected, and can be seen most clearly for $\alpha = 45°$ for which both contributions have opposite signs. Thus, both magnetic ratchets do not share the same value of magnetisation, indicating that they are generated in different parts of the metamaterial. This conclusion is also supported by the microscopic model, which demonstrate that the trigonal photocurrent is formed at the antidots' edges, whereas the ANE ratchet is formed in the bulk of the film, i.e. between the triangles and in particular in the sample as a whole. Thus, the magnetic characteristic should be different at the boundaries of the antidots. Indeed, measuring the Faraday rotation of the patterned area clearly demonstrate that the coercive field is larger than the one obtained from the unstructured sample; see Fig. 7.6(b). The method of Faraday rotation allows one to attain the magnetisation as an integrated quantity over the whole sample. In contrast, the photoresponse probes the magnetisation locally, i.e. the signal is proportional to the magnetisation in the vicinity of the edges, and hence the hysteresis of the photosignal is even larger, as seen by the red trace in Fig. 7.6(b). This difference in the coercive fields may have different reasons: (i) the electric near-field as well as the local heating can cause an inhomogeneous magnetisation vector at the antidot edges; (ii) the magnetic domain formation at the boundaries of the triangles might well be different from the formation in the bulk; or (ii) domain-wall pinning can play a role. Remarkably, if one applies radiation intensities that are five orders of magnitude higher than used in this work, only the amplitude of the signals increases but the hysteresis widths remain unaltered, as demonstrated in Ref. [125]. As a result, influences of the radiation electric field on the magnetisation characteristic, e.g. by near-fields and heating, can be ruled out.

Additional Superconducting quantum interference device (SQUID) and polar Kerr microscopy image measurements (see Fig. 7.7) conducted by Dr. Matthias Kronseder [125] substantiate possible mechanisms explaining the difference in the hysteresis widths. The measurements provide insights into the magnetisation and domain-wall switching. As can be seen in Fig. 7.7(b) a much larger negative H-field has to be applied in order to switch the domains in the patterned structure. This can be seen most pronounced at point B, at which the unstructured film has already inverted its magnetisation, whereas the patterned area keeps the previous spin-alignment. However, a sharp drop to negative magnetic moments is reached at point A, at which the unpatterned area of the sample switches its magnetisation, as seen in the SQUID loop measurement in Fig. 7.7(a). Although the Kerr microscope image measurements cannot resolve the domains and magnetisation inhomogeneities at the individual antidots, one can observe their role as pinning centers. Switching

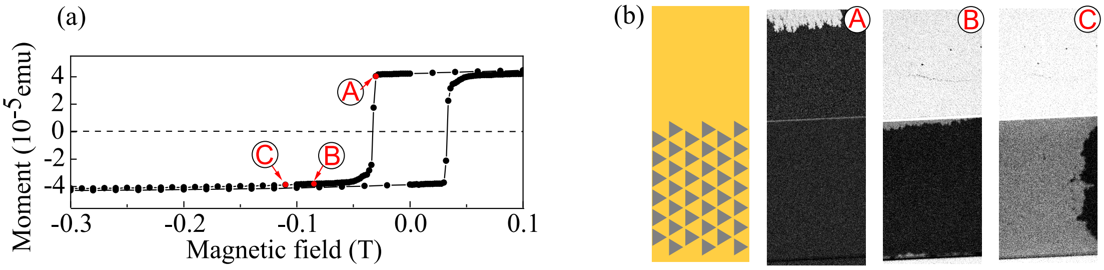

Figure 7.7 | Panel (a) shows a SQUID loop measured on the entire sample incorporating the unstructured Co/Pt film and the patterned area in the middle. Panel (b) shows the edge of the patterned area (yellow) and different Kerr microscopy images taken at the points A: −30 mT, B: −84 mT, and C:−110 mT. Black and white contrast denotes up and downward perpendicular magnetisation. Adapted from Ref. [125].

mechanisms in thin ferromagnetic films are notably sensitive to crystal defects, which results in nucleation and pinning sites for the domain walls. This holds for the unpatterned as well as for the patterned area (see, e.g. the fringed domain wall of the image taken at point A). As the dimension of one triangles is smaller than the usual width of the domain wall for Co/Pt multilayers, at small H-fields the interior of one triangle may reverse magnetisation by domain nucleation and propagation. In contrast, the reversal process of the boundary may be different because (i) the stray field is reduced because of the holes promoting magnetisation reversal in normally magnetised films; (ii) the domain walls shrink slightly owing to the domain-wall pinning at the apexes of the triangles; and (iii) defects and pinned moments may obstruct domain-wall propagation towards the triangles' boundaries.

8 Conclusion

This thesis has demonstrated that THz-induced optoelectronic ratchets can be generated effectively in 2D metamaterials. This has been shown in different realisations, namely the patterned-gated graphene samples [121–123] and the ferromagnetic Co/Pt stack [125]. A comparison of the results to phenomenological and microscopic theories developed by Dr. Leonid Golub in Refs. [121–123,125] has clearly demonstrated that the new experimental insights into 2D metamaterials are well described in a theoretical framework.

In the graphene-based metamaterials it has been demonstrated that THz radiation leads to a large photosignal due to the ratchet effect [121–123]. It has been shown that the dc photosignals are sensitive to the linear polarisation state of the incident radiation, and that they are generated by the joint action of near-field diffraction and the periodic electrostatic potential [121]. Specifically, it has been demonstrated that the magnitude and the direction of the observed photosignals are highly sensitive to the applied gate voltages, which is attributed to the combination of the back gate and the patterned gate voltages governing the potential profile, and consequently the ratchet current. The observed linear ratchet currents comprise a polarisation-independent Seebeck ratchet caused by electron gas heating, and the polarisation-dependent ratchet current as a result of the dynamic carrier-density redistribution mechanism [121]. Furthermore, it has been demonstrated that illuminating the graphene sample with circularly polarised terahertz radiation results in a ratchet current effect that reverses its sign upon switching the helicity of the radiation [122]. In addition, it has been observed that an applied out-of-plane magnetic field gives rise to magneto-ratchets that can be orders of magnitudes larger than the ratchets for zero magnetic field [123]. These magneto-ratchets feature $1/B$-periodic oscillations, which may or may not follow the Shubnikov–de Haas oscillations of transport measurements, depending on the combination of the patterned gate voltage and the back gate voltage. This finding is attributed to the fact that the ratchets can be formed in different spatial regions – between and inside the triangle-shaped areas in the graphene sheet above the patterned gate. Moreover, the complex Fano-shaped curve of the observed cyclotron resonance is shown to depend on the ratio of the components of the lateral asymmetry vector Ξ_{2D} [123].

In the other set of experiments, ratchets have been investigated in a ferromagnetic cobalt/platinum stack with strong perpendicular anisotropy that has triangle-shaped holes in the material forming a hexagonal antidot lattice. The study has demonstrated that THz excitation enables the observation of spin ratchets [125]. These magnetisation-sensitive dc currents can emerge as polarisation-independent current that has been shown to be induced by the Seebeck ratchet, which in the presence of magnetisation results in the anomalous Nernst effect ratchet. Furthermore, it has been demonstrated that the polarisation-dependent (trigonal) spin-ratchet is closely related to the anomalous Hall effect due to spin-dependent scattering on the edges of the triangular holes. The investigation has demonstrated that these two contributions exhibit a different hysteresis width. This is attributed to the different origin of the photosignal formation. Whereas the trigonal ratchet is sensitive to local inhomogeneities in the magnetisation at the triangle edges, the anomalous Nernst effect due to electron gas heating is sensitive to the average magnetisation over the entire metamaterial.

For future work, an interesting task would be to study the THz ratchet effects in metamaterials with periods that are much smaller than the mean-free path of the carriers. In such structures, which have a significantly modified spectrum exhibiting minibands, a new regime of ratchets may be observed.

References

[1] P. Olbrich, J. Karch, E. L. Ivchenko, J. Kamann, B. März, M. Fehrenbacher, D. Weiss, and S. D. Ganichev, *Classical Ratchet Effects in Heterostructures with a Lateral Periodic Potential*, Phys. Rev. B **83**, 165320 (2011).

[2] A. V. Nalitov, L. E. Golub, and E. L. Ivchenko, *Ratchet Effects in Two-dimensional Systems with a Lateral Periodic Potential*, Phys. Rev. B **86**, 115301 (2012).

[3] T. Otsuji, T. Watanabe, S. A. B. Tombet, A. Satou, W. M. Knap, V. V. Popov, M. Ryzhii, and V. Ryzhii, *Emission and Detection of Terahertz Radiation Using Two-dimensional Electrons in III–v Semiconductors and Graphene*, IEEE Trans. Terahertz Sci. Technol. **3**, 63–71 (2013).

[4] C. Drexler, S. A. Tarasenko, P. Olbrich, J. Karch, M. Hirmer, F. Müller, M. Gmitra, J. Fabian, R. Yakimova, S. Lara-Avila, S. Kubatkin, M. Wang, R. Vajtai, P. M. Ajayan, J. Kono, and S. D. Ganichev, *Magnetic Quantum Ratchet Effect in Graphene*, Nat. Nanotechnol. **8**, 104 (2013).

[5] Y. Kurita, G. Ducournau, D. Coquillat, A. Satou, K. Kobayashi, S. B. Tombet, Y. M. Meziani, V. V. Popov, W. Knap, T. Suemitsu, and T. Otsuji, *Ultrahigh Sensitive Sub-terahertz Detection by InP-based Asymmetric Dual-grating-gate High-electron-mobility Transistors and Their Broadband Characteristics*, Appl. Phys. Lett. **104**, 251114 (2014).

[6] G. V. Budkin and L. E. Golub, *Orbital Magnetic Ratchet Effect*, Phys. Rev. B **90**, 125316 (2014).

[7] P. Faltermeier, P. Olbrich, W. Probst, L. Schell, T. Watanabe, S. A. Boubanga-Tombet, T. Otsuji, and S. D. Ganichev, *Helicity Sensitive Terahertz Radiation Detection by Dual-grating-gate High Electron Mobility Transistors*, J. Appl. Phys. **118**, 084301 (2015).

[8] P. Olbrich, J. Kamann, M. König, J. Munzert, L. Tutsch, J. Eroms, D. Weiss, M.-H. Liu, L. E. Golub, E. L. Ivchenko, V. V. Popov, D. V. Fateev, K. V. Mashinsky, F. Fromm, T. Seyller, and S. D. Ganichev, *Terahertz Ratchet Effects in Graphene with a Lateral Superlattice*, Phys. Rev. B **93**, 075422 (2016).

[9] V. V. Popov, *Polarization-dependent Plasmonic Photocurrents in Two-dimensional Electron Systems*, Appl. Phys. Lett. **108**, 261104 (2016).

[10] D. V. Fateev, K. V. Mashinsky, J. D. Sun, and V. V. Popov, *Enhanced Plasmonic Rectification of Terahertz Radiation in Spatially Periodic Graphene Structures Towards the Charge Neutrality Point*, Solid-State Electron. **157**, 20–24 (2019).

[11] S. Hubmann, G. V. Budkin, M. Otteneder, D. But, D. Sacre, I. Yahniuk, K. Diendorfer, V. V. Belkov, D. A. Kozlov, N. N. Mikhailov, S. A. Dvoretsky, V. S. Varavin, V. G. Remesnik, S. A. Tarasenko, W. Knap, and S. D. Ganichev, *Symmetry breaking and circular photogalvanic effect in epitaxial CdHg films*, Physical Review Materials **4**, 043607 (2020).

[12] S. Boubanga-Tombet, W. Knap, D. Yadav, A. Satou, D. B. But, V. V. Popov, I. V. Gorbenko, V. Kachorovskii, and T. Otsuji, *Room-temperature Amplification of Terahertz Radiation by Grating-gate Graphene Structures*, Phys. Rev. X **10**, 031004 (2020).

[13] J. A. Delgado-Notario, V. Clericò, E. Diez, J. E. Velázquez-Pérez, T. Taniguchi, K. Watanabe, T. Otsuji, and Y. M. Meziani, *Asymmetric Dual-grating Gates Graphene FET for Detection of Terahertz Radiations*, APL Photonics **5**, 066102 (2020).

[14] E. Mönch, S. O. Potashin, K. Lindner, I. Yahniuk, L. E. Golub, V. Y. Kachorovskii, V. V. Bel'kov, R. Huber, K. Watanabe, T. Taniguchi, J. Eroms, D. Weiss, and S. D. Ganichev, *Ratchet effect in spatially modulated bilayer graphene: Signature of hydrodynamic transport*, Phys. Rev. B **105**, 045404 (2022).

[15] I. Yahniuk, G. V. Budkin, A. Kazakov, M. Otteneder, J. Ziegler, D. Weiss, N. N. Mikhailov, S. A. Dvoretskii, T. Wojciechowski, V. V. Bel'kov, W. Knap, and S. D. Ganichev, *Terahertz Ratchet Effect in Interdigitated HgTe Structures*, Physical Review Applied **18**, 054011 (2022).

[16] K. Tamura, C. Tang, D. Ogiura, K. Suwa, H. Fukidome, Y. Takida, H. Minamide, T. Suemitsu, T. Otsuji, and A. Satou, *Fast and sensitive terahertz detection with a current-driven epitaxial-graphene asymmetric dual-grating-gate field-effect transistor structure*, APL Photonics **7**, 126101 (2022).

[17] E. Mönch, S. O. Potashin, K. Lindner, I. Yahniuk, L. E. Golub, V. Y. Kachorovskii, V. V. Bel'kov, R. Huber, K. Watanabe, T. Taniguchi, J. Eroms, D. Weiss, and S. D. Ganichev, *Cyclotron and magnetoplasmon resonances in bilayer graphene ratchets*, Phys. Rev. B **107**, 115408 (2023).

[18] P. Olbrich, E. L. Ivchenko, R. Ravash, T. Feil, S. D. Danilov, J. Allerdings, D. Weiss, D. Schuh, W. Wegscheider, and S. D. Ganichev, *Ratchet Effects Induced by Terahertz Radiation in Heterostructures with a Lateral Periodic Potential*, Phys. Rev. Lett. **103**, 090603 (2009).

[19] E. L. Ivchenko and S. D. Ganichev, *Ratchet Effects in Quantum Wells with a Lateral Superlattice*, JETP Lett. **93**, 673–682 (2011), [Pisma v ZhETF **93**, 752 (2011)].

[20] L. Ermann and D. L. Shepelyansky, *Relativistic Graphene Ratchet on Semidisk Galton Board*, Eur. Phys. J. B **79**, 357–362 (2011).

[21] I Bisotto, E. S. Kannan, S Sassine, R Murali, T. J. Beck, L Jalabert, and J.-C. Portal, *Microwave based nanogenerator using the ratchet effect in Si/SiGe heterostructures*, Nanotechnology **22**, 245401 (2011).

[22] E. S. Kannan, I. Bisotto, J.-C. Portal, T. J. Beck, and L. Jalabert, *Energy Free Microwave Based Signal Communication Using Ratchet Effect*, Appl. Phys. Lett. **101**, 143504 (2012).

[23] E. Mönch, S. Hubmann, I. Yahniuk, S. Schweiss, V. V. Bel'kov, L. E. Golub, R. Huber, J. Eroms, K. Watanabe, T. Taniguchi, D. Weiss, and S. D. Ganichev, *Nonlinear intensity dependence of ratchet currents induced by terahertz laser radiation in bilayer graphene with asymmetric periodic grating gates*, J. Appl. Phys. **134**, 123102 (2023).

[24] D. Coquillat, S. Nadar, F. Teppe, N. Dyakonova, S. Boubanga-Tombet, W. Knap, T. Nishimura, T. Otsuji, Y. M. Meziani, G. M. Tsymbalov, and V. V. Popov, *Room temperature detection of sub-terahertz radiation in double-grating-gate transistors*, Optics Express **18**, 6024 (2010).

[25] W. Knap, S. Nadar, H. Videlier, S. Boubanga-Tombet, D. Coquillat, N. Dyakonova, F. Teppe, K. Karpierz, J. Łusakowski, M. Sakowicz, I. Kasalynas, D. Seliuta, G. Valusis, T. Otsuji, Y. Meziani, A. El Fatimy, S. Vandenbrouk, K. Madjour, D. Théron, and C. Gaquière, *Field Effect Transistors for Terahertz Detection and Emission*, Journal of Infrared, Millimeter, and Terahertz Waves **32**, 618–628 (2011).

[26] V. V. Popov, D. V. Fateev, T. Otsuji, Y. M. Meziani, D. Coquillat, and W. Knap, *Plasmonic Terahertz Detection by a Double-grating-gate Field-effect Transistor Structure with an Asymmetric Unit Cell*, Appl. Phys. Lett. **99**, 243504 (2011).

[27] T. Watanabe, Y. Kurita, A. Satou, T. Suemitsu, W. Knap, V. V. Popov, and T. Otsuji, "Terahertz Monochromatic Coherent Emission from an Asymmetric Chirped Dual-grating-gate InP-HEMT with a Photonic Vertical Cavity", in 2013 38th International Conference on Infrared, Millimeter, and Terahertz Waves (IRMMW-THz) (2013).

[28] V. V. Popov, *Terahertz Rectification by Periodic Two-dimensional Electron Plasma*, Appl. Phys. Lett. **102**, 253504 (2013).

[29] T. Watanabe, S. A. Boubanga-Tombet, Y. Tanimoto, D. Fateev, V. Popov, D. Coquillat, W. Knap, Y. M. Meziani, Y. Wang, H. Minamide, H. Ito, and T. Otsuji, *InP- and GaAs-Based Plasmonic High-Electron-Mobility Transistors for Room-Temperature Ultrahigh-Sensitive Terahertz Sensing and Imaging*, IEEE Sensors Journal **13**, 89–99 (2013).

[30] T. Otsuji, V. Popov, and V. Ryzhii, *Active Graphene Plasmonics for Terahertz Device Applications*, J. Phys. D: Appl. Phys. **47**, 094006 (2014).

[31] S. Boubanga-Tombet, Y. Tanimoto, A. Satou, T. Suemitsu, Y. Wang, H. Minamide, H. Ito, D. V. Fateev, V. V. Popov, and T. Otsuji, *Current-driven Detection of Terahertz Radiation Using a Dual-grating-gate Plasmonic Detector*, Appl. Phys. Lett. **104**, 262104 (2014).

[32] V. V. Popov, D. V. Fateev, E. L. Ivchenko, and S. D. Ganichev, *Noncentrosymmetric Plasmon Modes and Giant Terahertz Photocurrent in a Two-dimensional Plasmonic Crystal*, Phys. Rev. B **91**, 235436 (2015).

[33] I. Rozhansky, V. Kachorovskii, and M. Shur, *Helicity-driven Ratchet Effect Enhanced by Plasmons*, Phys. Rev. Lett. **114**, 246601 (2015).

[34] H. Spisser, A.-S. Grimault-Jacquin, N. Zerounian, A. Aassime, L. Cao, F. Boone, H. Maher, Y. Cordier, and F. Aniel, *Room-Temperature AlGaN/GaN Terahertz Plasmonic Detectors with a Zero-Bias Grating*, Journal of Infrared, Millimeter, and Terahertz Waves **37**, 243–257 (2016).

[35] Y. Koseki, V. Ryzhii, T. Otsuji, V. V. Popov, and A. Satou, *Giant Plasmon Instability in a Dual-grating-gate Graphene Field-effect Transistor*, Phys. Rev. B **93**, 245408 (2016).

[36] D. V. Fateev, K. V. Mashinsky, H. Qin, J. Sun, and V. V. Popov, *Giant Effect of Terahertz-radiation Rectification in Periodic Graphene Plasmonic Structures*, Semiconductors+ **51**, 1500–1504 (2017).

[37] G. Rupper, S. Rudin, and M. S. Shur, *Ratchet Effect in Partially Gated Multifinger Field-Effect Transistors*, Phys. Rev. Applied **9**, 064007 (2018).

[38] A. Yu, *Plasmon Ratchet Effect with Electrons and Holes Simultaneously Existing in the Graphene Channel: A Promising Effect for the Terahertz Detection*, J. Phys. D: Appl. Phys. **51**, 395103 (2018).

[39] P. Sai, S. O. Potashin, M. Szoła, D. Yavorskiy, G. Cywiński, P. Prystawko, J. Łusakowski, S. D. Ganichev, S. Rumyantsev, W. Knap, and V. Y. Kachorovskii, *Beatings of ratchet current magneto-oscillations in GaN-based grating gate structures: Manifestation of spin-orbit band splitting*, Phys. Rev. B **104**, 045301 (2021).

[40] T. Otsuji, S. A. Boubanga-Tombet, A. Satou, D. Yadav, H. Fukidome, T. Watanabe, T. Suemitsu, A. A. Dubinov, V. V. Popov, W. Knap, V. Kachorovskii, K. Narahara, M. Ryzhii, V. Mitin, M. S. Shur, and V. Ryzhii, *Graphene-based plasmonic metamaterial for terahertz laser transistors*, Nanophotonics **11**, 1677–1696 (2022).

[41] J. A. Delgado-Notario, W. Knap, V. Clericò, J. Salvador-Sánchez, J. Calvo-Gallego, T. Taniguchi, K. Watanabe, T. Otsuji, V. V. Popov, D. V. Fateev, E. Diez, J. E. Velázquez-Pérez, and Y. M. Meziani, *Enhanced terahertz detection of multigate graphene nanostructures*, Nanophotonics **11**, 519–529 (2022).

[42] X. Xu, N. M. Gabor, J. S. Alden, A. M. van der Zande, and P. L. McEuen, *Photo-Thermoelectric Effect at a Graphene Interface Junction*, Nano Letters **10**, 562–566 (2010).

[43] T. Mueller, F. Xia, and P. Avouris, *Graphene Photodetectors for High-speed Optical Communications*, Nat. Photonics **4**, 297–301 (2010).

[44] J. Yan, M.-H. Kim, J. A. Elle, A. B. Sushkov, G. S. Jenkins, H. M. Milchberg, M. S. Fuhrer, and H. D. Drew, *Dual-gated Bilayer Graphene Hot-electron Bolometer*, Nat. Nanotechnol. **7**, 472–478 (2012).

[45] T. J. Echtermeyer, P. S. Nene, M. Trushin, R. V. Gorbachev, A. L. Eiden, S. Milana, Z. Sun, J. Schliemann, E. Lidorikis, K. S. Novoselov, and A. C. Ferrari, *Photothermoelectric and Photoelectric Contributions to Light Detection in Metal–Graphene–Metal Photodetectors*, Nano Lett. **14**, 3733–3742 (2014).

[46] X. Cai, A. B. Sushkov, R. J. Suess, M. M. Jadidi, G. S. Jenkins, L. O. Nyakiti, R. L. Myers-Ward, S. Li, J. Yan, D. K. Gaskill, T. E. Murphy, H. D. Drew, and M. S. Fuhrer, *Sensitive Room-temperature Terahertz Detection Via the Photothermoelectric Effect in Graphene*, Nat. Nanotechnol. **9**, 814–819 (2014).

[47] S. D. Ganichev, D. Weiss, and J. Eroms, *Terahertz Electric Field Driven Electric Currents and Ratchet Effects in Graphene*, Ann. Phys. **529**, 1600406 (2017).

[48] D. V. Fateev, K. V. Mashinsky, and V. V. Popov, *Terahertz Plasmonic Rectification in a Spatially Periodic Graphene*, Appl. Phys. Lett. **110**, 061106 (2017).

[49] M. Y. Morozov, V. V. Popov, and D. V. Fateev, *Electrically controllable active plasmonic directional coupler of terahertz signal based on a periodical dual grating gate graphene structure*, Sci. Rep. **11** (2021).

[50] C. Drexler, N. Dyakonova, P. Olbrich, J. Karch, M. Schafberger, K. Karpierz, Y. Mityagin, M. B. Lifshits, F. Teppe, O. Klimenko, Y. M. Meziani, W. Knap, and S. D. Ganichev, *Helicity Sensitive Terahertz Radiation Detection by Field Effect Transistors*, J. Appl. Phys. **111**, 124504 (2012).

[51] K. Romanov and M. Dyakonov, *Theory of helicity-sensitive terahertz radiation detection by field effect transistors*, Applied Physics Letters **102** (2013).

[52] I. V. Gorbenko, V. Y. Kachorovskii, and M. S. Shur, *Plasmonic Helicity-Driven Detector of Terahertz Radiation*, physica status solidi (RRL) – Rapid Research Letters **13** (2018).

[53] E. Mönch, S. O. Potashin, K. Lindner, I. Yahniuk, L. E. Golub, V. Y. Kachorovskii, V. V. Bel'kov, R. Huber, K. Watanabe, T. Taniguchi, J. Eroms, D. Weiss, and S. D. Ganichev, *Cyclotron and magnetoplasmon resonances in bilayer graphene ratchets*, Physical Review B **107**, 115408 (2023).

[54] M. Scheid, M. Wimmer, D. Bercioux, and K. Richter, *Zeeman ratchets for ballistic spin currents*, physica status solidi c **3**, 4235–4238 (2006).

[55] M. V. Costache and S. O. Valenzuela, *Experimental Spin Ratchet*, Science **330**, 1645–1648 (2010).

[56] M. E. Flatté, *A one-way street for spin current*, Nature Physics **4**, 587–588 (2010), Stochastic processes in Physics and Chemistry (in honor of Peter Hänggi).

[57] P. Faltermeier, G. V. Budkin, J. Unverzagt, S. Hubmann, A. Pfaller, V. V. Bel'kov, L. E. Golub, E. L. Ivchenko, Z. Adamus, G. Karczewski, T. Wojtowicz, V. V. Popov, D. V. Fateev, D. A. Kozlov, D. Weiss, and S. D. Ganichev, *Magnetic Quantum Ratchet Effect in (Cd,Mn)Te- and CdTe-based Quantum Well Structures with a Lateral Asymmetric Superlattice*, Phys. Rev. B **95**, 155442 (2017).

[58] P. Faltermeier, G. V. Budkin, S. Hubmann, V. V. Bel'kov, L. E. Golub, E. L. Ivchenko, Z. Adamus, G. Karczewski, T. Wojtowicz, D. A. Kozlov, D. Weiss, and S. D. Ganichev, *Circular and Linear Magnetic Quantum Ratchet Effects in Dual-grating-gate CdTe-based Nanostructures*, Phys. E **101**, 178–187 (2018).

[59] M. Matsubara, T. Kobayashi, H. Watanabe, Y. Yanase, S. Iwata, and T. Kato, *Polarization-controlled tunable directional spin-driven photocurrents in a magnetic metamaterial with threefold rotational symmetry*, Nature Communications **13**, 6708 (2022).

[60] R. Huber, M.-H. Liu, S.-C. Chen, M. Drienovsky, A. Sandner, K. Watanabe, T. Taniguchi, K. Richter, D. Weiss, and J. Eroms, *Gate-Tunable Two-Dimensional Superlattices in Graphene*, Nano Letters **20**, 8046–8052 (2020).

[61] Z. G. Li and P. F. Carcia, *Microstructural dependence of magnetic properties of Pt/Co multilayer thin films*, J. Appl. Phys. **77** (1992).

[62] C. Thönißen, *Magnetische Eigenschaften von einzelnen Co/Pt- und Co-Nanostrukturen*, PhD thesis, University of Hamburg, 2018.

[63] P. A. M. Dirac, *The Quantum Theory of the Electron*, Proc. R. Soc. London, Ser. B **117**, 610–624 (1928).

[64] H. Weyl, *Elektron Und Gravitation. I*, Z. Phys. **56**, 330 (1929).

[65] A. H. Castro Neto, F. Guinea, N. M. R. Peres, K. S. Novoselov, and A. K. Geim, *The electronic properties of graphene*, Rev. Mod. Phys. **81**, 109–162 (2009).

[66] K. S. Novoselov, A. K. Geim, S. V. Morozov, D. Jiang, Y. Zhang, S. V. Dubonos, I. V. Grigorieva, and A. A. Firsov, *Electric Field Effect in Atomically Thin Carbon Films*, Science **306**, 666 (2004).

[67] K. S. Novoselov, A. K. Geim, S. V. Morozov, D. Jiang, M. I. Katsnelson, I. V. Grigorieva, S. V. Dubonos, and A. A. Firsov, *Two-dimensional Gas of Massless Dirac Fermions in Graphene*, Nature **438**, 197 (2005).

[68] Y. Zhang, Y.-W. Tan, H. L. Stormer, and P. Kim, *Experimental Observation of the Quantum Hall Effect and Berry's Phase in Graphene*, Nature **438**, 201–204 (2005).

[69] S. Das Sarma, S. Adam, E. H. Hwang, and E. Rossi, *Electronic transport in two-dimensional graphene*, Rev. Mod. Phys. **83**, 407–470 (2011).

[70] J. Cayssol, *Introduction to Dirac materials and topological insulators*, en, Comptes Rendus. Physique **14**, 760–778 (2013).

[71] R. Kundu, *Tight-binding parameters for graphene*, Modern Physics Letters B **25**, 163–173 (2011).

[72] R. S. Deacon, K.-C. Chuang, R. J. Nicholas, K. S. Novoselov, and A. K. Geim, *Cyclotron resonance study of the electron and hole velocity in graphene monolayers*, Phys. Rev. B **76**, 081406 (2007).

[73] P. R. Wallace, *The band theory of graphite*, Phys. Rev. **71**, 622–634 (1947).

[74] C. J. Drexler, *Photoelectric Phenomena in Graphene Induced by Terahertz Laser Radiation*, PhD thesis, University of Regensburg, 2014.

[75] R. R. Nair, P. Blake, A. N. Grigorenko, K. S. Novoselov, T. J. Booth, T. Stauber, N. M. R. Peres, and A. K. Geim, *Fine Structure Constant Defines Visual Transparency of Graphene*, Science **320**, 1308–1308 (2008).

[76] S. D. Ganichev and W. Prettl, *Intense Terahertz Excitation of Semiconductors* (Oxford Science Publications, 2006).

[77] L. D. Landau and E. M. Lifshitz, *Electrodynamics of continuous media*, Vol. 8 (Pergamon Press, 1960).

[78] J. Wagner, *The magnetic properties of ultrathin cobalt multilayers symmetrically and antisymmetrically sandwiched between layers of platinum and iridium*, PhD thesis, University of Hamburg, 2018.

[79] S. Freercks, *Comparison of the magnetic properties of ferromagnetic films and nanostructures*, PhD thesis, University of Hamburg, 2020.

[80] R. C. O'Handley, *Modern Magnetic Materials: Principles and Applications* (Wiley, 1992).

[81] S. Chikazumi, *Physics of Ferromagnetism* (Oxford Science Publication, 1997).

[82] E. C. Stoner and E. P. Wohlfarth, *A mechanism of magnetic hysteresis in heterogeneous alloys*, Philosophical Transactions of the Royal Society of London. Series A, Mathematical and Physical Sciences **240**, 599–642 (1948).

[83] S. Blundell, *Magnetism in Condensed Matter* (Oxford Science Publications, 2001).

[84] C.-J. Lin, G. Gorman, C. Lee, R. Farrow, E. Marinero, H. Do, H. Notarys, and C. Chien, *Magnetic and structural properties of Co/Pt multilayers*, Journal of Magnetism and Magnetic Materials **93**, 194–206 (1991).

[85] Y. Nie, X. Yang, P. Zhang, and H. Sang, *Magnetization and coercivity in Co/Pt multilayers with constant total Co layer thickness*, Transactions of Nonferrous Metals Society of China **20**, 819–824 (2010).

[86] E. H. Hall, *On a New Action of the Magnet on Electric Currents*, Am. J. Math. **2** (1879).

[87] K. von Klitzing, *The quantized Hall effect*, Rev. Mod. Phys. **58**, 519–531 (1986).

[88] S. R. Boona, H. Jin, and S. Watzman, *Transverse thermal energy conversion using spin and topological structures*, Journal of Applied Physics **130**, 171101 (2021).

[89] X. Kou, Y. Fan, and K. L. Wang, *Review of Quantum Hall Trio*, Journal of Physics and Chemistry of Solids **128**, 2–23 (2019), Spin-Orbit Coupled Materials.

[90] R. A. Griffiths, *Anomalous Anomalous Hall effect measurements of bilayer magnetic structures*, PhD thesis, University of Manchester, 2016.

[91] N. Nagaosa, J. Sinova, S. Onoda, A. H. MacDonald, and N. P. Ong, *Anomalous Hall effect*, Rev. Mod. Phys. **82**, 1539–1592 (2010).

[92] M.-C. Chang and Q. Niu, *Berry phase, hyperorbits, and the Hofstadter spectrum: Semiclassical dynamics in magnetic Bloch bands*, Phys. Rev. B **53**, 7010–7023 (1996).

[93] G. Sundaram and Q. Niu, *Wave-packet dynamics in slowly perturbed crystals: Gradient corrections and Berry-phase effects*, Phys. Rev. B **59**, 14915–14925 (1999).

[94] Q. Zhang, *Scattering Effect on Anomalous Hall Effect in Ferromagnetic Transition Metals*, PhD thesis, King Abdullah University of Science and Technology, 2017.

[95] E. Mönch, S. O. Potashin, K. Lindner, I. Yahniuk, L. E. Golub, V. Y. Kachorovskii, V. V. Bel'kov, R. Huber, K. Watanabe, T. Taniguchi, J. Eroms, D. Weiss, and S. D. Ganichev, *Ratchet effect in spatially modulated bilayer graphene: Signature of hydrodynamic transport*, Phys. Rev. B **105**, 045404 (2022).

[96] S. Hubmann, V. V. Bel'kov, L. E. Golub, V. Y. Kachorovskii, M. Drienovsky, J. Eroms, D. Weiss, and S. D. Ganichev, *Giant Ratchet Magneto-photocurrent in Graphene Lateral Superlattices*, Phys. Rev. Research **2**, 033186 (2020).

[97] Y. M. Blanter and M. Büttiker, *Rectification of Fluctuations in an Underdamped Ratchet*, Phys. Rev. Lett. **81**, 4040–4043 (1998).

[98] A. V. Nalitov, L. E. Golub, and E. L. Ivchenko, *Ratchet effects in two-dimensional systems with a lateral periodic potential*, Phys. Rev. B **86**, 115301 (2012).

[99] A. F. Kip, *Cyclotron resonance in solids*, Contemporary Physics **1**, 355–369 (1960).

[100] S. Hunklinger, *Festkörperphysik [German]* (De Gruyter, Berlin, Boston, 2018).

[101] K. Seeger, *Semicondcutor Physics* (Springer, Berlin, Heidelberg, 2004).

[102] T. Numai, *Fundamentals of Semiconductors* (Springer, Tokyo, 2004).

[103] C. Hamaguchi, *Basic Semiconductor Physics* (Springer, Berlin Heidelberg, 2010).

[104] L. D. Landau and E. M. Lifshitz, *Quantum Mechanics: Non-relativistic Theory* (Pergamon Press, 1965).

[105] N. M. R. Peres, F. Guinea, and A. H. Castro Neto, *Electronic properties of disordered two-dimensional carbon*, Phys. Rev. B **73**, 125411 (2006).

[106] M. L. Sadowski, G. Martinez, M. Potemski, C. Berger, and W. A. de Heer, *Landau Level Spectroscopy of Ultrathin Graphite Layers*, Phys. Rev. Lett. **97**, 266405 (2006).

[107] A. M. Witowski, M. Orlitapniewski, familyi=c., given=R., giveni=R., „ A. Wysmołek, J. M. Baranowskiski, familyi=n., given=W., giveni=W., „ C. Faugeras, G. Martinez, and M. Potemski, *Quasiclassical cyclotron resonance of Dirac fermions in highly doped graphene*, Phys. Rev. B **82**, 165305 (2010).

[108] Y. Zhang, *Electronic Transport in Graphene*, PhD thesis, Columbia University, 2017.

[109] T. Ihn, *Electronic Quantum Transport in Mesoscopic Semiconductor Structures* (SPRINGER NATURE, 2004).

[110] M. Otteneder, *Terahertz magnetospectroscopy of HgTe-based heterostructure materials*, PhD thesis, University of Regensburg, 2021.

[111] S. D. Ganichev and W. Prettl, *Intense terahertz excitation of semiconductors* (Oxford University Press, Oxford, 2005).

[112] L. Landau and E. Lifshitz, *Mechanics*, 3rd ed., Vol. 1 (Butterworth-Heinemann, 1976).

[113] P. Olbrich, *THz radition induced spin polarized currents in low dimensional semiconductor structures*, PhD thesis, University of Regensburg, 2010.

[114] O. Svelto, *Principles of Lasers*, 4th ed. (Springer, 1998).

[115] F. K. Kneubühl and M. W. Sigrist, *Laser*, German, 3rd ed. (Teubner Studienbücher, Stuttgart, 1991).

[116] S. D. Ganichev, *Tunnel Ionization of Deep Impurities in Semiconductors Induced by Terahertz Electric Fields*, Phys. B **273-274**, 737–742 (1999).

[117] T. Herrmann, I. A. Dmitriev, D. A. Kozlov, M. Schneider, B. Jentzsch, Z. D. Kvon, P. Olbrich, V. V. Bel'kov, A. Bayer, D. Schuh, D. Bougeard, T. Kuczmik, M. Oltscher, D. Weiss, and S. D. Ganichev, *Analog of Microwave-induced Resistance Oscillations Induced in GaAs Heterostructures by Terahertz Radiation*, Phys. Rev. B **94**, 081301 (2016).

[118] M. Bass, ed., *Handbook of Optics: Volume II - Design, Fabrication, and Testing; Sources and Detectors; Radiometry and Photometry*, en, 3rd Edition (McGraw-Hill Education, New York, 2010).

[119] E. Hecht, *Optics* (Fourth edition. Reading, Mass. : Addison-Wesley, [2002] ©2002, [2002]), Includes bibliographical references (pages 685-688) and index.

[120] F. Bréhat and B. Wyncke, *Measurement of the optical constants of crystal quartz at 10 K and 300 K in the far infrared spectral range: 10–600 cm–1*, International Journal of Infrared and Millimeter Waves **18**, 1663–1679 (1997).

[121] I. Yahniuk, M. Hild, L. E. Golub, J. Amann, J. Eroms, D. Weiss, W.-H. Kang, M.-H. Liu, K. Watanabe, T. Taniguchi, and S. D. Ganichev, *Terahertz ratchet in graphene two-dimensional metamaterial formed by a patterned gate with an antidot array*, Phys. Rev. B **109**, 235428 (2024).

[122] M. Hild, I. Yahniuk, L. E. Golub, J. Amann, J. Eroms, D. Weiss, K. Watanabe, T. Taniguchi, and S. D. Ganichev, *Circular terahertz ratchets in a two-dimensionally modulated Dirac system*, Phys. Rev. Research **6**, 023308 (2024).

[123] M. Hild, E. Mönch, L. E. Golub, I. A. Dmitriev, I. Yahniuk, K. Amann, J. Amann, J. Eroms, J. Wunderlich, D. Weiss, C. Consejo, C. Bray, K. Maussang, F. Teppe, J. Gumenjuk-Sichevska, K. Watanabe, T. Taniguchi, and S. D. Ganichev, *Terahertz and gigahertz magnetoratchets in graphene-based two-dimensional metamaterials*, Phys. Rev. B **110**, 125303 (2024).

[124] M. Drienovsky, J. Joachimsmeyer, A. Sandner, M.-H. Liu, T. Taniguchi, K. Watanabe, K. Richter, D. Weiss, and J. Eroms, *Commensurability Oscillations in One-dimensional Graphene Superlattices*, Phys. Rev. Lett. **121**, 026806 (2018).

[125] M. Hild, L. E. Golub, A. Fuhrmann, M. Otteneder, M. Kronseder, M. Matsubara, T. Kobayashi, D. Oshima, A. Honda, T. Kato, J. Wunderlich, C. Back, and S. D. Ganichev, *Terahertz spin ratchet effect in magnetic metamaterials*, Phys. Rev. B **107**, 155419 (2023).

[126] M. M. Glazov and S. D. Ganichev, *High Frequency Electric Field Induced Nonlinear Effects in Graphene*, Phys. Rep. **535**, 101 (2014).

[127] S. Candussio, M. V. Durnev, S. A. Tarasenko, J. Yin, J. Keil, Y. Yang, S.-K. Son, A. Mishchenko, H. Plank, V. V. Bel'kov, S. Slizovskiy, V. Fal'ko, and S. D. Ganichev, *Edge Photocurrent Driven by Terahertz Electric Field in Bilayer Graphene*, Phys. Rev. B **102**, 045406 (2020).

[128] S. Sassine, Y. Krupko, J.-C. Portal, Z. D. Kvon, R. Murali, K. P. Martin, G. Hill, and A. D. Wieck, *Experimental Investigation of the Ratchet Effect in a Two-dimensional Electron System with Broken Spatial Inversion Symmetry*, Phys. Rev. B **78**, 045431 (2008).

[129] E. S. Kannan, I. Bisotto, J.-C. Portal, R. Murali, and T. J. Beck, *Photovoltage induced by ratchet effect in Si/SiGe heterostructures under microwave irradiation*, Applied Physics Letters **98**, 193505 (2011).

[130] A. D. Chepelianskii, M. V. Entin, L. I. Magarill, and D. L. Shepelyansky, *Ratchet Transport of Interacting Particles*, Phys. Rev. E **78**, 041127 (2008).

[131] A. Logg, K.-A. Mardal, and G. Wells, eds., *Automated Solution of Differential Equations by the Finite Element Method: The FEniCS Book* (Springer Berlin Heidelberg, 2012).

[132] C. Geuzaine and J. Remacle, *Gmsh: A 3-D finite element mesh generator with built-in pre- and post-processing facilities*, International Journal for Numerical Methods in Engineering **79**, 1309–1331 (2009).

[133] G. V. Budkin, L. E. Golub, E. L. Ivchenko, and S. D. Ganichev, *Magnetic Ratchet Effects in a Two-dimensional Electron Gas*, JETP Lett. **104**, 649–656 (2016).

[134] R. Krishnan, M. Porte, M. Tessier, and N. K. Flevaris, “Structural and Magnetic Studies in Co-Pt Multilayers”, in *Science and Technology of Nanostructured Magnetic Materials*, edited by G. C. Hadjipanayis and G. A. Prinz (Springer US, Boston, MA, 1991), p. 191.

[135] A Lorke, S Wimmer, B Jager, J. Kotthaus, W Wegscheider, and M Bichler, *Far-infrared and transport properties of antidot arrays with broken symmetry*, Physica B: Condensed Matter **249-251**, 312–316 (1998).

[136] W. Weber, L. E. Golub, S. N. Danilov, J. Karch, C. Reitmaier, B. Wittmann, V. V. Bel’kov, E. L. Ivchenko, Z. D. Kvon, N. Q. Vinh, A. F. G. van der Meer, B. Murdin, and S. D. Ganichev, *Quantum Ratchet Effects Induced by Terahertz Radiation in Gan-based Two-dimensional Structures*, Phys. Rev. B **77**, 245304 (2008).

[137] H. Linke, *Ratches and Brownian Motors: Basics, Experiments and Applications*, Appl. Phys. A **75**, 167–167 (2002).

[138] S. V. Koniakhin, *Ratchet Effect in Graphene with Trigonal Clusters*, Eur. Phys. J. B **87**, 216 (2014).

[139] P. Olbrich, L. E. Golub, T. Herrmann, S. N. Danilov, H. Plank, V. V. Bel’kov, G. Mussler, C. Weyrich, C. M. Schneider, J. Kampmeier, D. Grützmacher, L. Plucinski, M. Eschbach, and S. D. Ganichev, *Room-temperature High-frequency Transport of Dirac Fermions in Epitaxially Grown* Sb_2te_3*- and* Bi_2te_3*-based Topological Insulators*, Phys. Rev. Lett. **113**, 096601 (2014).

[140] S. N. Danilov, L. E. Golub, T. Mayer, A. Beer, S. Binder, E. Mönch, J. Minár, M. Kronseder, C. H. Back, D. Bougeard, and S. D. Ganichev, *Superlinear Photogalvanic Effects in (Bi0.3Sb0.7)2 (Te0.1Se0.9)3 : Probing Three-Dimensional Topological Insulator Surface States at Room Temperature*, Phys. Rev. Applied **16**, 064030 (2021).

[141] V. I. Belinicher and B. I. Sturman, *The Photogalvanic Effect in Media Lacking a Center of Symmetry*, Phys. Usp. **23**, 199 (1980), [*Usp. Fiz. Nauk* **1980**, *130*, 415].

[142] M. Otteneder, S. Hubmann, X. Lu, D. A. Kozlov, L. E. Golub, K. Watanabe, T. Taniguchi, D. K. Efetov, and S. D. Ganichev, *Terahertz Photogalvanics in Twisted Bilayer Graphene Close to the Second Magic Angle*, Nano Lett. **20**, 7152–7158 (2020).

Acknowledgments

I would like to take this opportunity to express my gratitude to everyone who helped me on my way to writing this thesis. It has been a journey of challenge and growth in both subject-specific and individual, personal circumstances.

I am especially grateful to my supervisor, Sergey D. Ganichev, for giving me the opportunity to do my PhD in a great working atmosphere and for always supporting me throughout the thesis sand giving me scientific guidance. I am thankful for his sincere openness to questions and proposals for improvement.

Moreover, I would like to thank Leonid E. Golub, Vanya A. Dmitriev, and Matthias Kronseder for their theoretical support, enlightening discussions, and proofreading of the manuscript. In addition, my thanks go to Masakazu Matsubara, Marina Marocko, and Julia Amann for proving samples for my research, and for answering transport- and sample-related questions.

I would like to thank the whole working group, current and actual members, in particular Hannelore Lanz, Christian Schneider, Sergey Danilov, Mariya Moldavskaya, Erwin Mönch, Ivan Yahniuk, Anna Fuhrmann, Sophia Isabella Hofmeister, Sebastian Piehler, Katharina Amman, Stefan Hubmann, Max Otteneder and Susanne Candussio. I have had a great time and they have motivated me. I would especially like to extend my gratitude to Stefan and Max, who provided invaluable guidance during my Master's thesis, and to Erwin, with whom I have collaborated extensively in numerous international conferences and schools, and who diligently proofread my thesis. I would also like to thank my former bachelor and master students Anna, Isabella, Sebastian, and Katharina for a wonderful and funny time and for their great support in the lab.

I would like to finally thank my family and friends for their encouragement, understanding and belief in my abilities throughout this academic journey.